Part II

Analysis of the first IPHAS results

The analysis carried out in the following chapters takes into account all the 233 candidates, due to the lack of strong evidence supporting a denomination as "non planetary nebula".

4

General properties of the IPHAS PNe (and candidates)

4.1   Galactic distributions

The section of the sky observed in this study corresponds to the longitude range ~29 degrees to ~79 degrees.

Figure 4.1 shows galactic extinction as a function of galactic longitude (l) versus Galactic latitude (b). As expected, the extinction is higher near the plane (between ~±1 degree). The graph reveals a nearly homogeneous distribution of our nebulae. Some areas appear empty: this means that either there are no nebulae or we are in front of zones of relatively high extinction. But in those zones, the extinction is lower than others where nebulae have been discovered. So it is likely that there is simply a lack of objects at these locations.
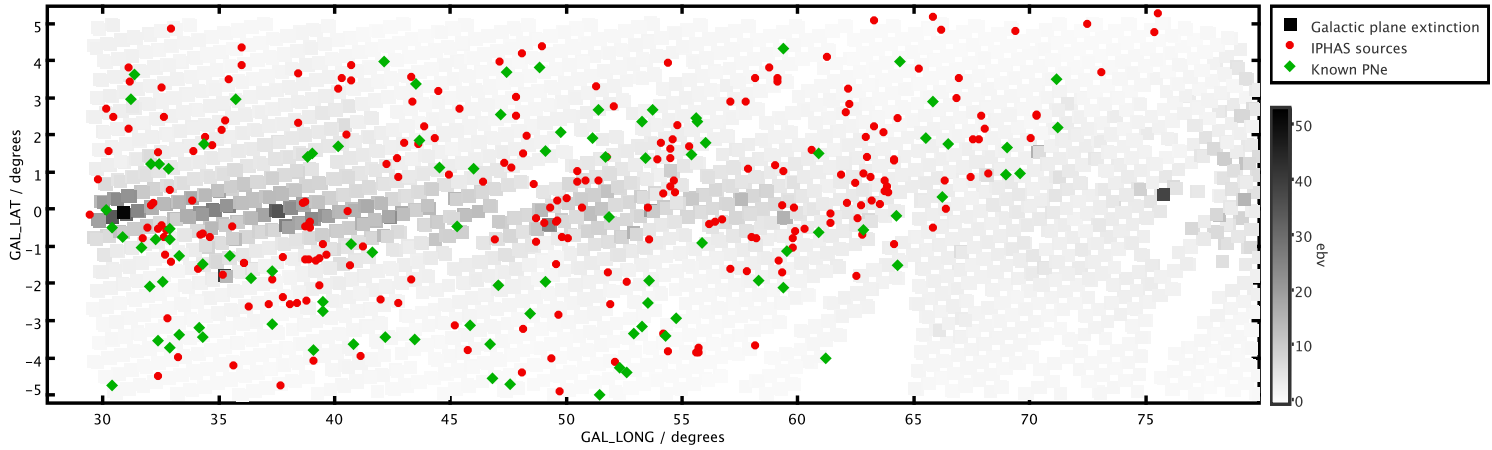
Figure 4.1: Galactic Distribution of the IPHAS nebulae and known PNe. The line-of-sight reddening is indicated on the right hand-side and is derived from Schlegel et al. (1998) dust maps.

If we compare in more detail the galactic location of our candidates and newly confirmed PNe with 98 known PNe located in the same area (Fig. 4.1 and Fig. 4.2), we can see that the overall longitudinal distribution is roughly similar except for the higher number of IPHAS objects. As we deal with a rather small portion of the sky (2h in RA), we do not expect to see spectacular changes in this direction. In contrast, in the latitudinal plane (b) we observed a gap between ~ -2 and ~ 1 degree between the two categories of objects. There are many more IPHAS nebulae (107) than known PNe (29) in this region. This difference nearly factor 4, shows that **IPHAS allowed the discovery of many more objects close to the Galactic Plane, and hence in heavier extinction zones.**

In an attempt to identify which kind of nebulae have been missed so far we consider two parameters: the size and the morphology dependence. First, all the nebulae are divided in 4 groups relative to their dimensions: the nebulae with a size lower than 20 arcsec, then between 20 arcsec and 60 arcsec, between 60 arcsec and 100 arcsec and finally with a size greater than 100 arcsec. The results are listed in Table 4.1.

Table 4.1: Number of IPHAS nebulae and known planetary nebulae in the galactic plane according their size.

Size	Whole area		-2 < b < 1	
	IPHAS	Known PNe	IPHAS	Known PNe
≤ 20"	92	64	41	13
20" < b < 60"	64	23	26	10
60" < b < 100"	29	3	14	3
≥ 100"	48	8	26	3

Along with the histogram in Figure 4.3, Table 4.1 shows that the distribution of small size nebulae i.e with a size lower than 20 arcsec is nearly comparable between the known PNe and the IPHAS nebulae across the galactic plane, although there are
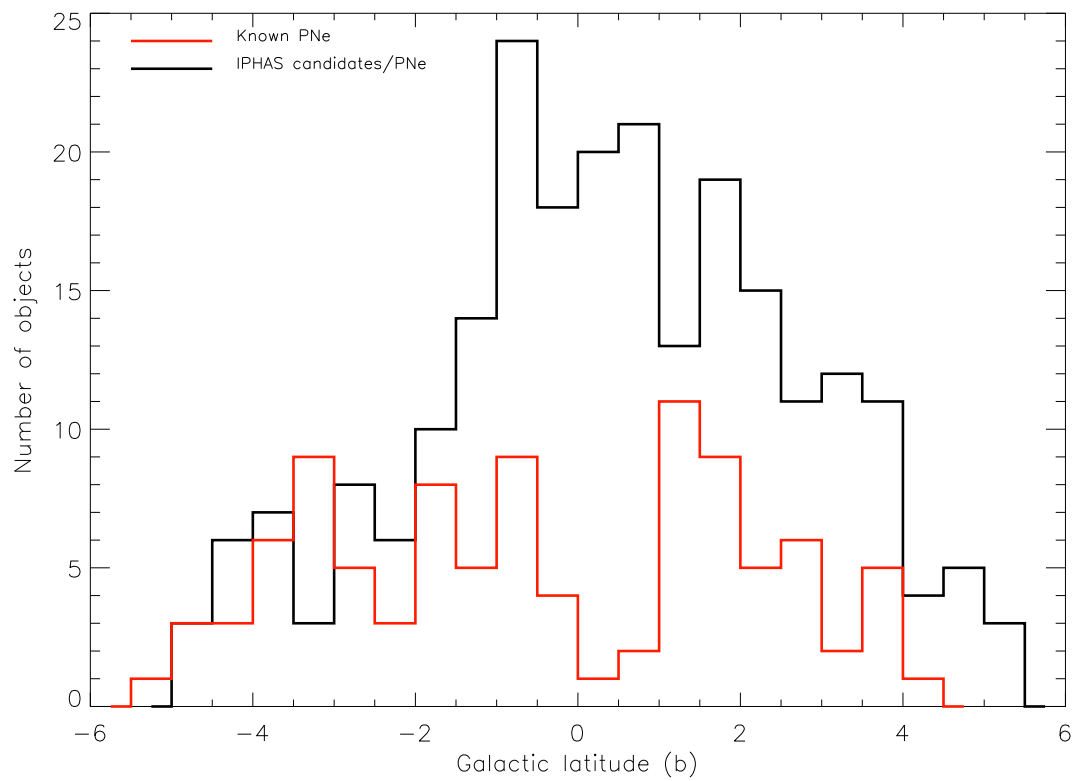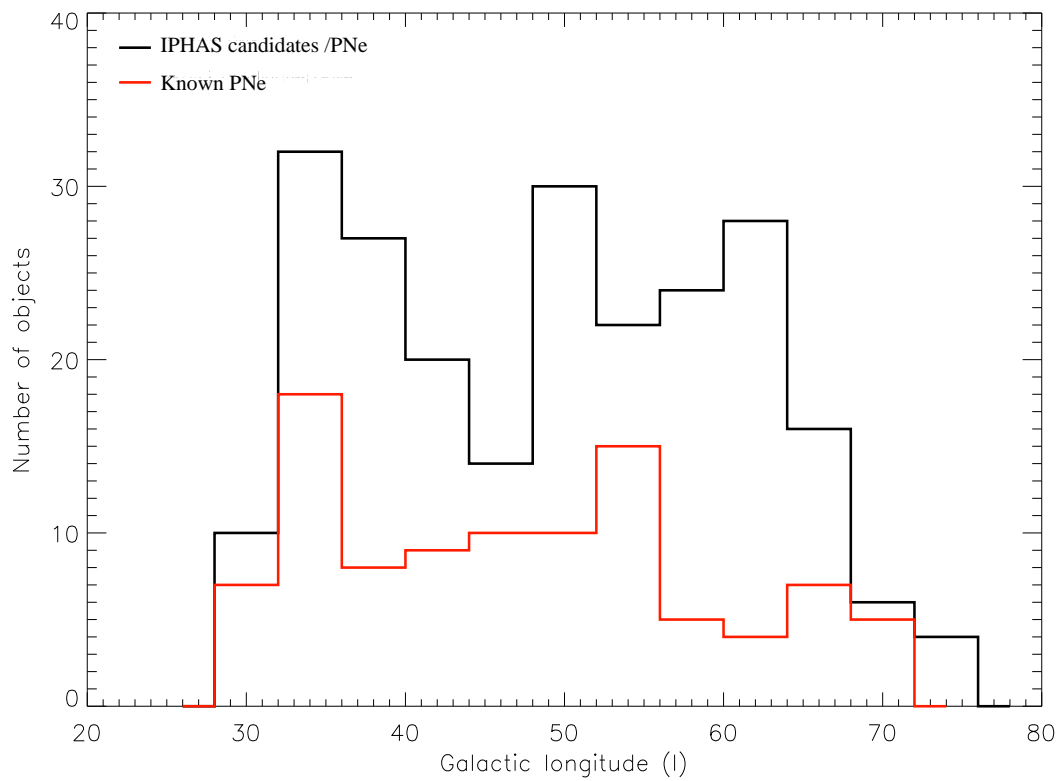
Figure 4.2: Galactic distribution of newly discovered objects and known PNe.
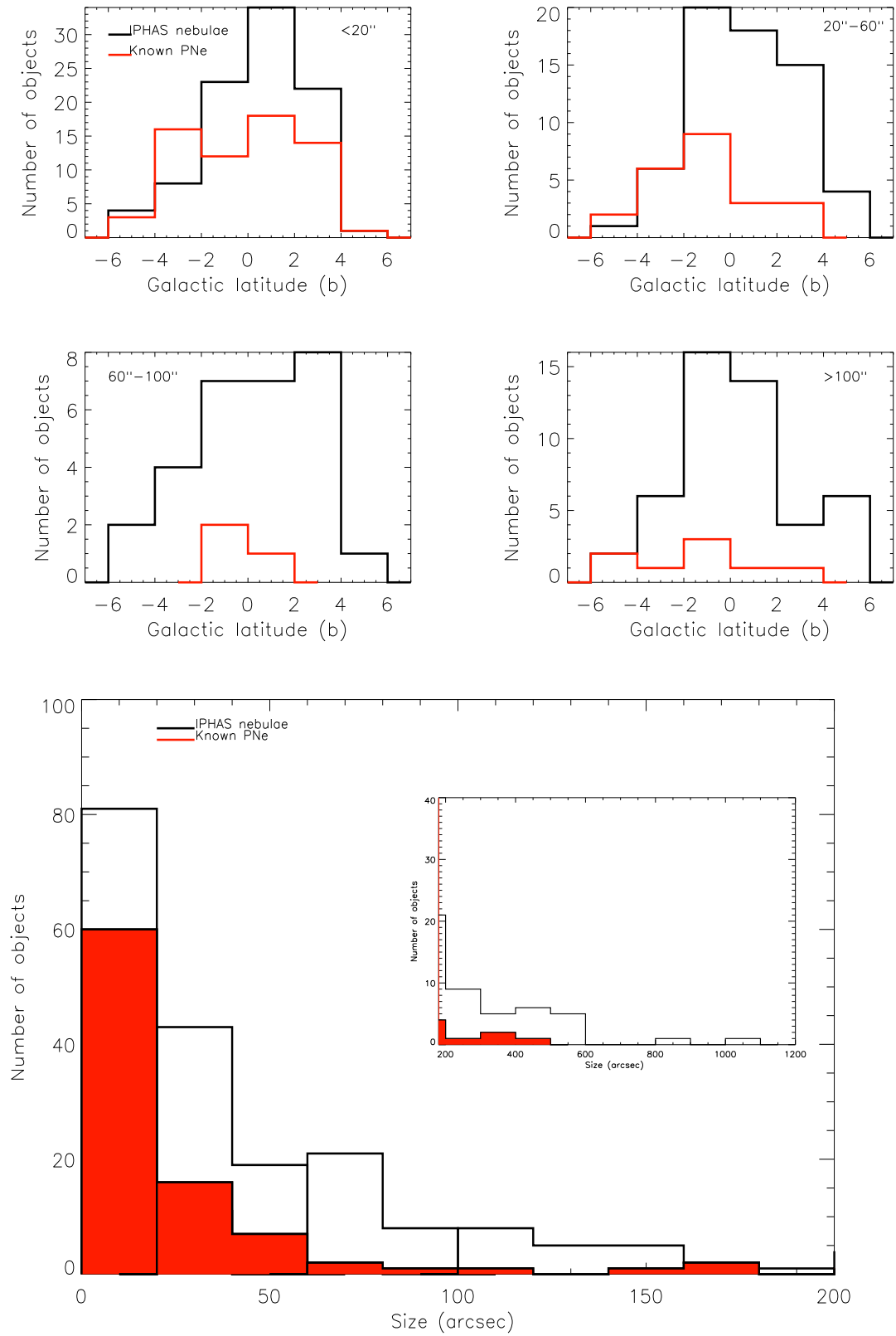
Figure 4.3: Distribution on the Plane of the IPHAS nebulae according their size.

about 1.5 times more nebulae detected by IPHAS. But in low latitude regions, detection is improved by a factor of 3. With IPHAS we can therefore discover more small sources in high extinction zones. While moving towards large nebulae we observed a drastic change: the IPHAS nebulae outnumber by far the known large PNe. As an example, concerning the largest ones (greater than 100 arcsec), there is no known PN (from our sample) between -1 deg < b < 1 deg, while there are 21 extended IPHAS nebulae. The improvement of our results at low latitude is confirmed here again.

So, the first "hidden population" revealed by IPHAS, is the one relative to the large nebulae with a size greater than ~20 arcsec. We expected that around 1/3 of them would be *bona fide* PNe based on their morphology.

The exact morphology of planetary nebulae is not easy to define with only the first data of the survey. So we did a tentative classification which is likely to change in the future, and listed the results of a comparative study in Table 4.2. The location on the plane of each category is shown in Fig. 4.4. Figure 4.5 shows that although we observed slightly more new bipolar nebulae, the general scheme remained the same in comparison to the known PNe *in terms of number of nebulae*. This is also the case for the round and elliptical nebulae. In agreement with the population of known PNe, there are more elliptical and round IPHAS objects than there are bipolar IPHAS objects. The emerging group is the irregular nebulae, which was previously poorly represented at low galactic latitudes and which is spread all over the plane in the longitudinal direction. Even if all the nebulae listed under this morphology are not true planetary nebulae, the number of those qualified as such will still be more than those we already know (none are previously identified between 0 and 1 degree for example). Unfortunately we are unable to quantify this number.

In terms of location above the plane, the "established" trend is followed (Table 4.3). Thus, IPHAS bipolar sources are located closer to the plane than elliptical and round nebulae. The irregular nebulae have a mean absolute galactic latitude which places them between the round and elliptical nebulae, and this figure is true for both

known and new nebulae. An other interesting point, is that these IPHAS populations have a systematically lower mean absolute galactic latitude than their known counterparts. The gathering of both datasets would therefore give a less biased figure of the distribution of the morphological populations in this direction of the Galactic Plane. In order to compare the scale height of our new nebulae with that of the known PNe in the studied sky area, we used an exponential distribution based on the mean absolute galactic latitude to fit the distribution in latitude for the different morphological classes (Fig. 4.6 and Table 4.3 for the FWHM). The distribution function is

$$n(b) = n_0 \exp^{\frac{-b}{<|b|>}} \qquad (4.1)$$

with n(b) the number of nebulae and n_0 the number of nebulae at b=0.

It appears that the exponential curves relative to the IPHAS nebulae and known PNe fit their histograms well. There is a level of correlation with the group of round PNe: the "scale height", **in terms of latitudes**, of this morphological population does not change drastically. This correlation between IPHAS and known PNe becomes less obvious for elliptical and bipolar nebulae respectively. And, it can be clearly seen that the level of discrepancy between both groups is highest for the irregular nebulae. The "latitudinal scale height" for these three populations need to be updated.

Table 4.2: Number of IPHAS nebulae and known planetary nebulae in the area observed according their morphology.

|	Round	Elliptical	Bipolar	Irregular
IPHAS	76 (33±11%)	26 (11±19%)	19 (8±22%)	112 (48±9%)
Known PNe	52 (53±14%)	24 (24±20%)	11 (11±30%)	11 (11±30%)
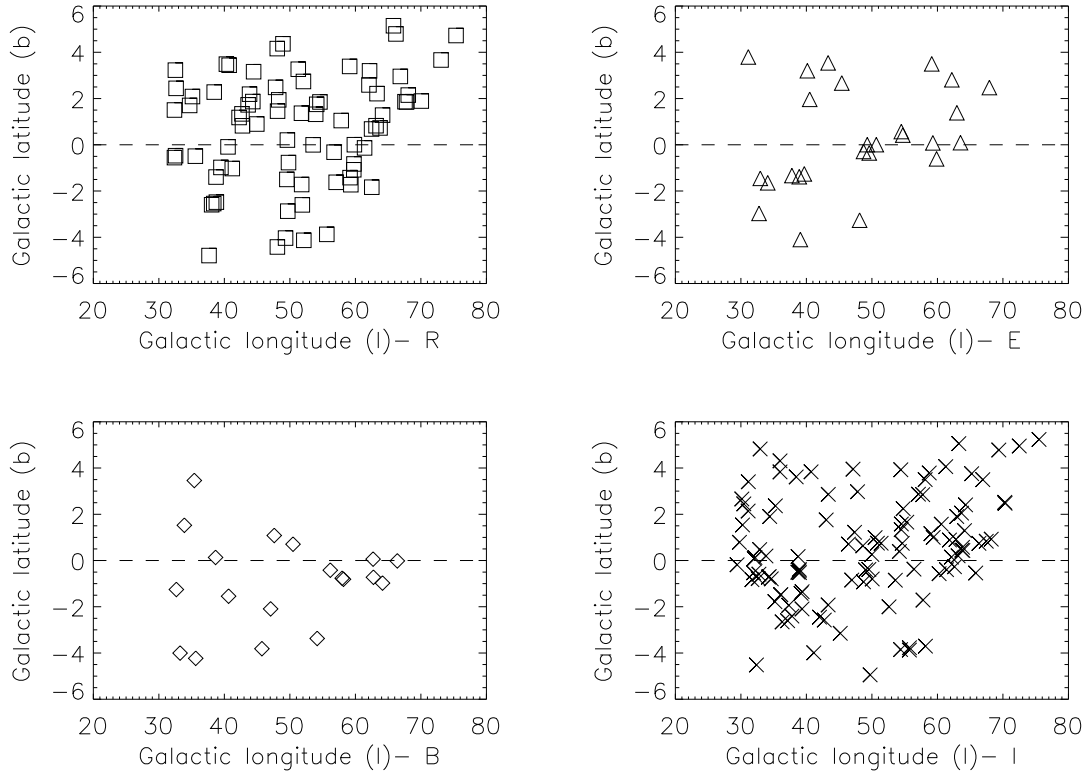
Figure 4.4: Morphological distribution of the IPHAS and known PNe. Top left: Round, Top right: Elliptical, Bottom left: Bipolar and Bottom right: Irregular.

Table 4.3: Mean latitude and dispersion (FWHM) of each morphological population for IPHAS nebulae and known PNe.

| Morphology	$< |b| >$ deg		FWHM deg	
	IPHAS	Known PNe	IPHAS	Known PNe
Round	2.0	2.4	6.4	9.5
Elliptical	1.7	2.0	6.2	8.4
Bipolar	1.6	1.8	7.7	6.2
Irregular	1.8	2.0	6.2	9.0
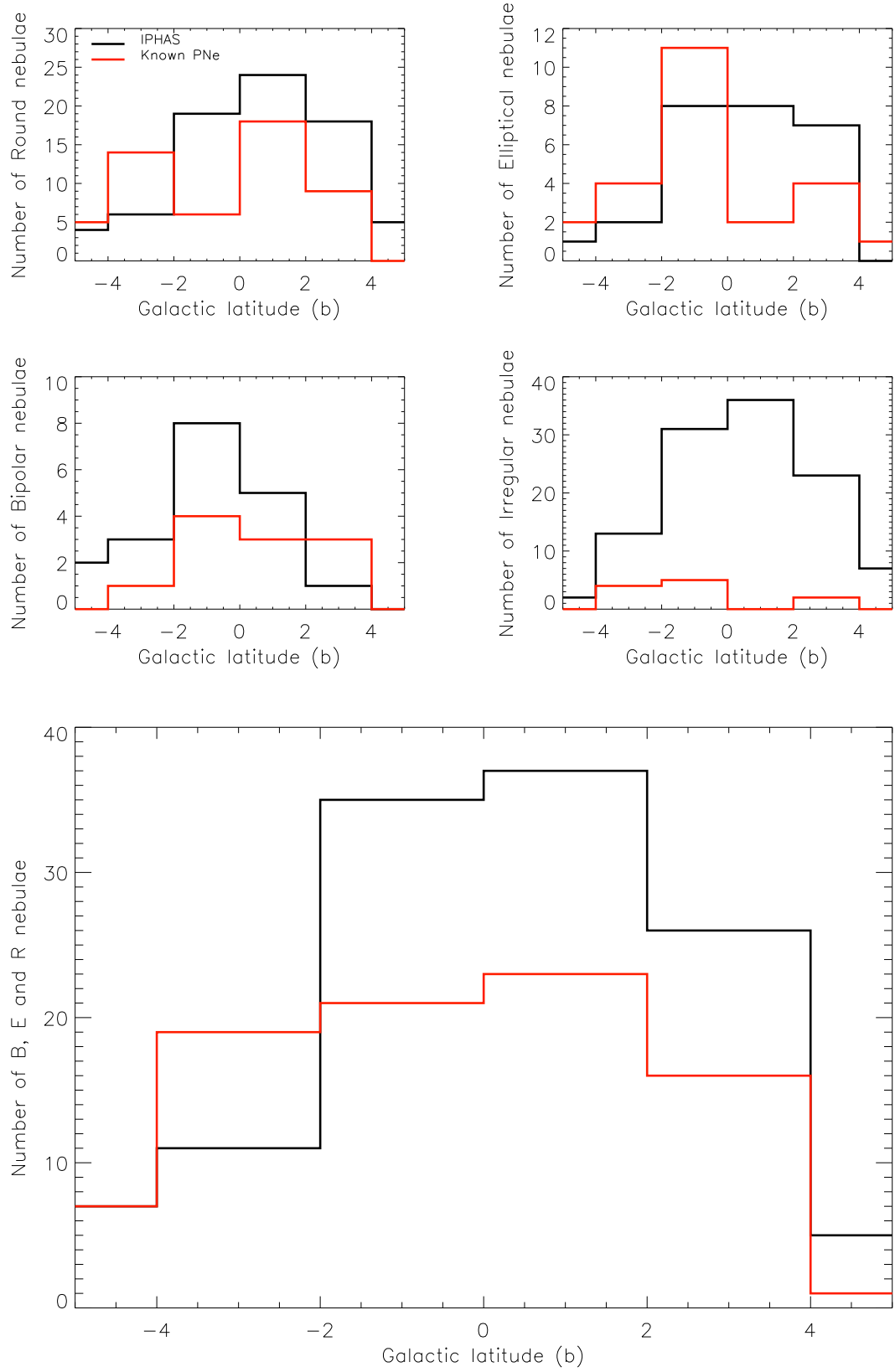
Figure 4.5: Number and morphology of the IPHAS and known PNe.
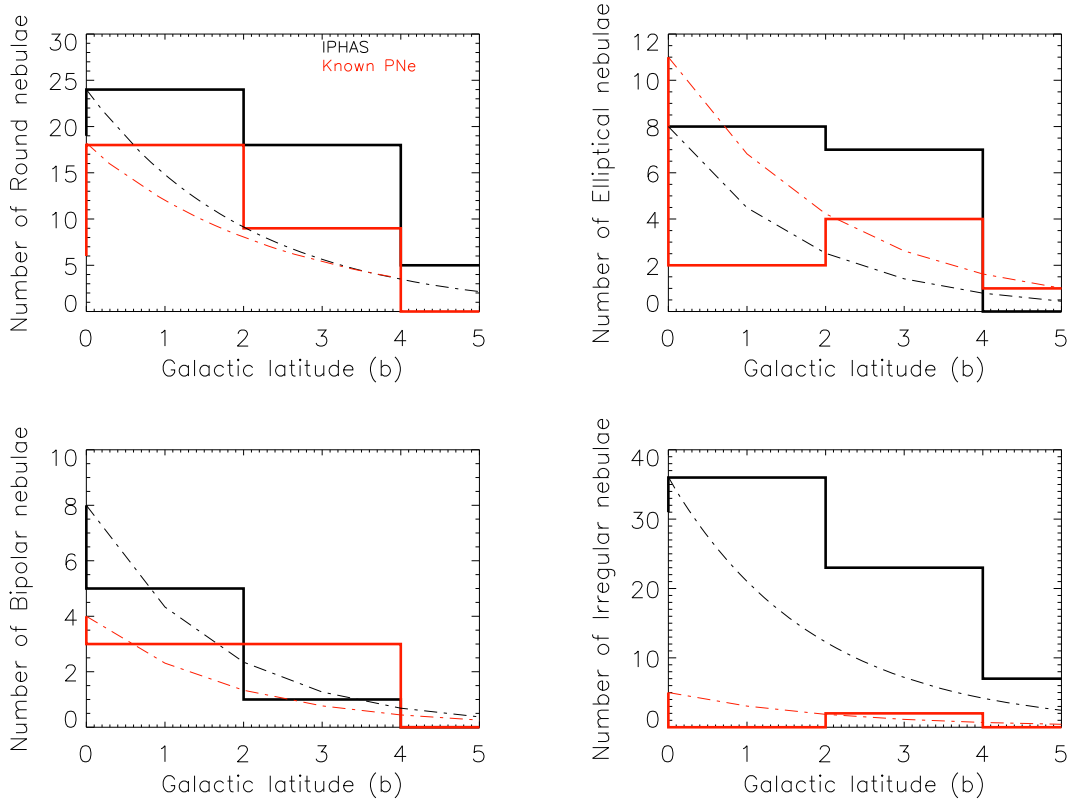
Figure 4.6: Morphological distribution of populations detected in IPHAS in terms of the latitudes. The fits represent the exponential distributions of the heights above the plane in latitude .

The INT photometric Hα Survey of the Galactic Plane has therefore contributed to:

- The increase in number of nebulae most of all **at low latitude (near b=0)**, their height being distance dependent. Therefore IPHAS can detect nebulae **throughout zones of high extinction (e.g. E(B-V) up to ~ 13 mag)**.

- The discovery of **two**, so far "hidden populations" which are **the large nebulae** with a size greater than ~ 20 arcsec and **the irregular nebulae**.

- The general increase in nebulae for each morphological class.

Several objects which were previously undetectable due to interstellar dust or their

intrinsic faintness (because of their large size or evolutionary status) are now observable and available for further studies.

4.2   Discussion

Our finding of hidden populations in the region of the plane observed here, lead us to investigate their nature and origin.

Little is known about **irregular PNe**. Corradi and Schwarz (1995) pointed out that the irregular PNe have properties between the bipolar and elliptical groups (for instance their location between those two groups on the plane) and that they may not be a proper class of objects but a mixture of both mentioned groups where the morphology has not been well established. Nevertheless, for those objects where the central stars have been studied, Stanghellini et al. (1993) found that they concentrated on the central part of the HR diagram (i.e. with log T_{eff}~5K and log L/L$\odot$~3.5), contrary to the elliptical and bipolar PNe, which show a wider spread. We could argue that the absence of symmetry in these nebulae is due to their evolutionary state in the sense that they have reached an advanced point where they lose their shape and start to mix with the ISM. But if we consider their size, which is an indicator of the age of the nebulae, we see that there is no absolute correlation (Fig 4.7). The irregular nebulae are not specially larger than the other morphological classes. There is therefore no indication that they are older and are then the end products of other classes. But the determination of their distance is essential to verify this claim. Phillips (2004) used line ratio mapping to differentiate the morphological classes and found that all the nebulae defined as irregular in his sample (14 over 300), have a high HeII(4686)/Hβ ratio (see his figure 9). This means that they are high excitation PNe and hence have a high effective temperature. Phillips (2004) derived a mean HeII Zanstra temperature of 99 000 K, in between the bipolar with a mean T_Z(HeII)=~118-138 000 K and the round and elliptical PNe with a mean

T_Z(HeII)=~81-92 000 K. The [NII]/Hβ ratio of the irregular PNe is comparable to that of the elliptical PNe.

We are therefore in the presence of a new genuine class of PNe which does not seem to originate from a known morphological class, with its own location on the plane, its own central star temperature range and of course its own morphology characterised by the absence of strict symmetry. So the question is now what are the predecessors of these objects ? If we compare the PNe scale height derived by Corradi and Schwarz (1995) and Manchado et al. (2000) (see Table 1.2) with the scale height found by Jura and Kleinmann (1992a) and Jura and Kleinmann (1992b) for AGB stars with pulsation periods up to 400 days, and the height scales derived from Pottasch (1984) for AGB stars with periods greater than 400 days, we find a quite good correlation:

- Round PNe correspond in scale height to (O-rich) Mira with short period (100-300 days) and to semi-regulars (SRs) with 200-300 days period.

- Elliptical PNe are relative to intermediate period SRs and (O-rich) Miras (300-400 days). There is also a correlation with short period SRs (100-150 days).

- Bipolar PNe scale heights correlate with long period Mira and OH-IR stars (P greater than 450 days).

Following Pottasch (1984) and assuming that the miras with periods of ~200 days have a progenitor mass of about 1M$\odot$ and those with periods of ~450 days have a progenitor mass of about 2M$\odot$ (this trend was also found by Vassiliadis and Wood (1993)), we estimate the origin of the irregular IPHAS nebulae. According to our classification (Table 4.3), the irregular nebulae are localised between the elliptical and bipolar nebulae. They would therefore have as progenitors, (O-rich) AGB stars with intermediate to long periods, with a high mass between 1M$\odot$ and 1.5-2 M$\odot$ (without reaching the bipolar progenitor mass level). The relatively high mass of the irregulars' progenitors is also supported by their high effective temperature.
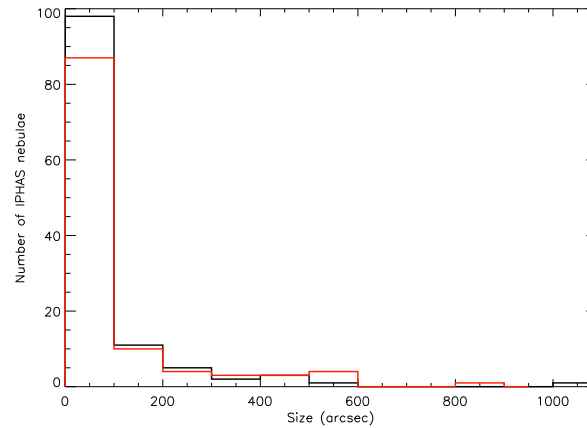
Figure 4.7: Representation of the IPHAS nebulae according their morphology and their relative size. The black histogram shows the groups of elliptical, bipolar and round nebulae; the red histogram shows the irregular IPHAS nebulae.

Planetary nebulae with a **large angular size** are in general quite close. This is observed when using the Shklovskii method to obtain the distances, and assuming that the PNe have a constant ionised mass. A more complete definition and an application of this method with some IPHAS targets is shown in section 6.3. Kaler et al. (1990) studied a set of large PNe and we derived from their sample (75 objects) an average angular size of 57 arcsec, a mean radius of 0.30 pc and a mean distance of 2.5 kpc. Those extended PNe are also believed to be older, as there is a positive correlation between their central stars cooling and the expansion of their nebulae (see their figure 12). The core mass is also an important parameter as the higher the mass, the larger the nebular size.

Therefore the 141 nebulae found within IPHAS having an angular size greater than 20 arcsec, would be more evolved and/or could be derived from massive progenitors. But our sample is biased by the presence of probable HII regions as well as young supernovae remnants.

After screening the Galactic Plane between b=±5° and 29° <l< 79°, we ended up with a large number of new nebulae in this direction. Moreover, from a purely

morphological point of view we assumed that at least 2/3 of the objects detected could be classified from true to probable PNe. When we introduced the planetary nebulae, one of the obvious, unresolved issues was the mismatch between the total number of detected PNe in the Galaxy and the estimated theoretical one. One of the goals of the IPHAS nebulae search was to attempt to reduce the gap. So it is interesting to know how many PNe were theoretically expected in the region that we studied, and therefore what was the efficiency of the survey.

The total number of PNe in the Galaxy can be defined as follows:

$$N(D, z) = 2 \times N_0 \times \int_0^{+\infty} e^{\frac{-D}{Dl}} \, dD \times \int_0^{+\infty} e^{\frac{-z}{zl}} \, dz \qquad (4.2)$$

with N(D,z) the number of nebula as a function of the galactic length and height; N_0 the number density of local PNe; $e^{\frac{-D}{Dl}}$ represents the distribution of the PNe as a function of the galactocentric distance D and the scale length Dl; finally $e^{\frac{-z}{zl}}$, shows the distribution of the PNe as a function of the height above the plane z and the scale height zl. We assume the scale length to be 3 kpc in the old disk (Kitchin 2004) and the scale height for PNe is 250 pc. In the area we investigated, we found that 1200±200 planetary nebulae are expected to be present, assuming that 28 000±5000 PNe in total populate the Galaxy (Frew and Parker 2006). We noticed that this number increases to ~2500 if we consider 60 000 PNe as claimed by Shklovsky. In figure 4.8, we show the expected distribution of planetary nebulae in latitude compared to the observations made so far in our sky area. We can see that the lack of detection occurs mainly at low latitude range which implies a higher extinction rate (although IPHAS increases the detection rate in this low latitude range). Therefore, we may not be able to retrieve the missing PNe with such optical surveys.
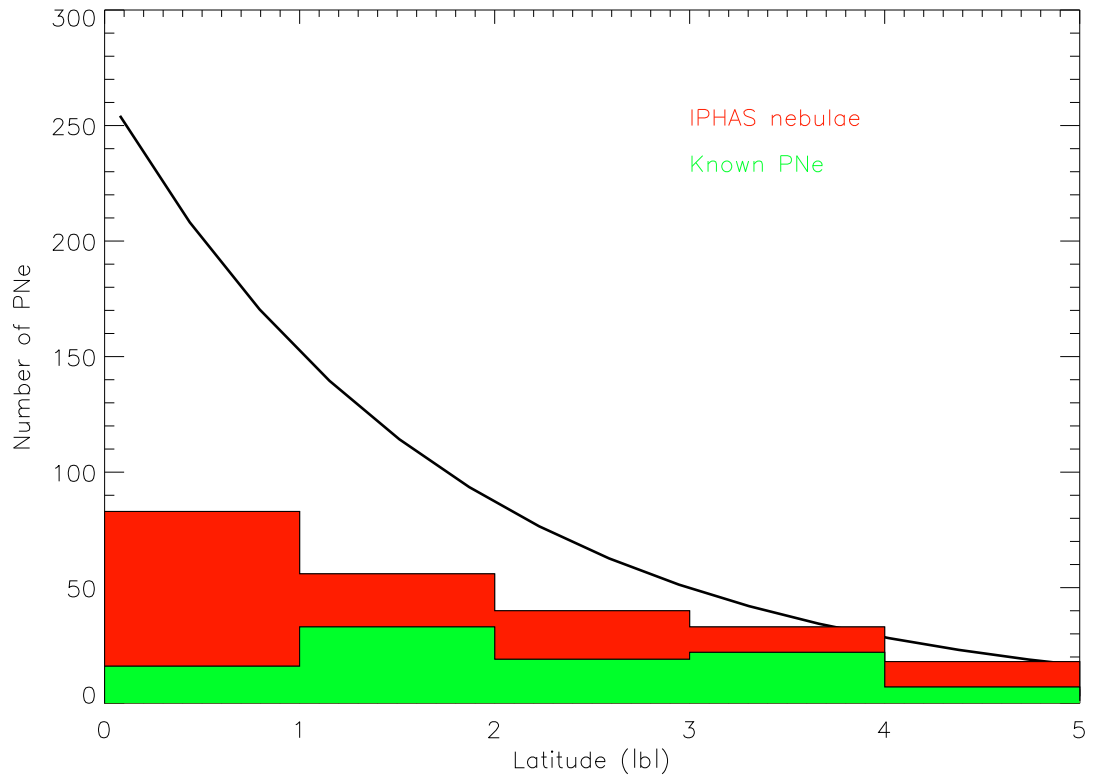
Figure 4.8: Expected versus observed nebulae in the Galactic plane between 18h and 20h. The black curve shows the expected distribution of PNe as a function of the latitude.

5

Infrared properties of the IPHAS sources

5.1 Introduction

Figure 3.12, used to determine the nature of some IPHAS sources, unveils a particular characteristic: all of them show a systematic 60μm excess in comparison to the known PNe located in the same sky area.

The emission detected with IRAS is mainly due to dust. Leene and Pottasch (1987) claimed that the 12μm and 25μm radiation of PNe was due to line emission while the 60μm and 100μm emission was only due to dust. We therefore concluded that the 60μm excess is due to an excess of dust. Using the Pottasch diagram (Fig.3.12), some IPHAS objects (with high 60μm excess) tend to fall in the HII region zone (where we do expect a large amount of dust for those massive nebulae) or are undetermined. But we can question the accuracy of the diagnostic diagram when it comes to separating HII regions and PNe, most of all with the new type of nebulae discovered by IPHAS. Indeed, as shown with the radio observations (Part 1, section 3.3) and in chapter 4, IPHAS nebulae represent a faint population. This type of object is perhaps missed by Pottasch et al. (1988) leading to a wrong delimitation in the diagram and then a

wrong classification. In order to test the diagram, we need to know whether the IRAS colours of the IPHAS nebulae (and particularly those without a clear classification) are consistent or not with a planetary nebula nature. This will involve modelling the IPHAS nebulae.

5.2   CLOUDY models

In order to proceed, we used version C07.02.02 of the photoionisation code CLOUDY, last described by Ferland et al. (1998). The model atmosphere used for the stellar flux is the 2nd generation grid model from Rauch (2003) and the geometry is spherical (Fig. 5.1). We have to emphasise that this was a non-exhaustive study, and we do not pretend to give "state of the art" models. Hence, the abundances chosen here are typical abundances for planetary nebulae but they can be different from one PN to another. We assumed that it would not interfere in the accuracy of our models since we did not have the spectra of our sources to give the correct values. The use of silicate grains was preferred as few objects were expected to be C-rich (although we also show some examples with graphite grains for a set of IPHAS targets). This is due to the fact that few AGB stars become C-rich in the inner Galaxy (6-8 kpc) (Le Bertre et al. 2001). Finally, we have to note the strong influence of the 12μm flux in our modelling. This flux is thought to be due mainly to atomic line emission which can be dominant over the dust emission and lead to an increase of the F12/F25 ratio. Here again, the lack of spectra prevented us correcting this 12μm influence.

Before modelling our objects, we first show the range of 12/25 μm and 25/60 μm on which planetary nebulae evolve, principally as a function of their radius and density. The parameters for each model are listed in Tables 5.1 and 5.2.

For each model, we adopted a different density, effective temperature and type of grain. The range of masses from our models evolved is 0.8 $M_\odot$ to 10^{-5} $M_\odot$. The IR colours given by the CLOUDY modelling for the three different densities, are presented in a F12/F25 vs F25/F60 diagram to allow their comparison with the Pottasch diagram.
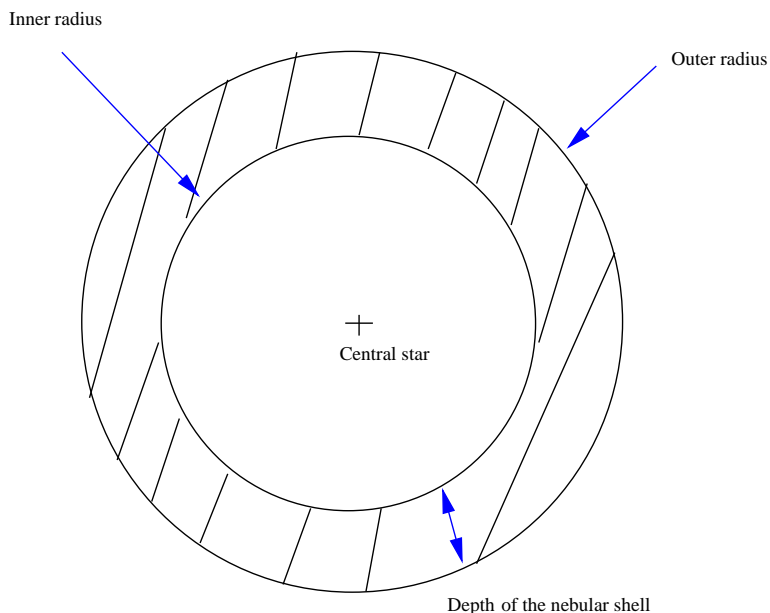
Figure 5.1: Closed geometry assumed in the CLOUDY models with the central star as source of ionisation and the dashed area the nebular shell.

The results are shown in Figures 5.2, 5.3 and 5.4 (with the Pottasch delimitations).

Several observations can be made from these graphics:

- First, we notice that the higher density model nebulae have lower F12/F25 flux ratios (and then towards warmer dust). At high density the 25μm fluxes seems dominant over the 12μm. This behaviour only affects the largest nebulae, with a radius between 0.1 pc and 0.01 pc (model A, B and C). In fact, the nebulae represented by model D (R=0.005 pc) do not show any major variations while evolving from high to low densities.

- We also remark on the difference between two models when the differing parameter is the nature of the dust grains: graphite dust has a systematic higher

Table 5.1: Main parameters for the CLOUDY models. The four last for parameters are free.

Symmetry	Spherical
Distance	2 kpc
Abundances	Typical PNe
Luminosity	$10^{36.5}$ erg/s
Electronic temperature	$10^{3.9}$ K
Grain	Silicate (ISM) and graphite (ISM)
Hydrogen density	$10^{3.96}$, $10^{2.96}$, and $10^{1.96}$ cm^{-3}
Electronic density	$10^{3.97}$, $10^{2.97}$, and $10^{1.97}$ cm^{-3}
Stellar Temperature	50 000 K and 100 000 K

Table 5.2: Radius for each CLOUDY models.

Model	Model A	Model B	Model C	Model D
Inner radius	0.1 pc	0.05 pc	0.01 pc	0.005 pc

F12/F25 flux and lower F25/F60 flux than silicate dust. This discrepancy decreases with increasing density. The size of the different types of grain or the efficiency of their emissivity in the IR wavelength may account for the features observed.

- In the models with a density of 100 and 1000 cm^{-3}, we observed a displacement in the diagram from the zone where the dust is warmer (bottom right of the diagrams) to a zone where the dust is colder (top left of the diagrams), with an increase of the radius from 0.005 to 0.01, 0.05 and 0.1 parcsecs. This is consistent with the fact that the greater the radius, the less efficient is the dust heating.

We also show in Figure 5.5 the spectra for model A using Silicate grains at 100 and
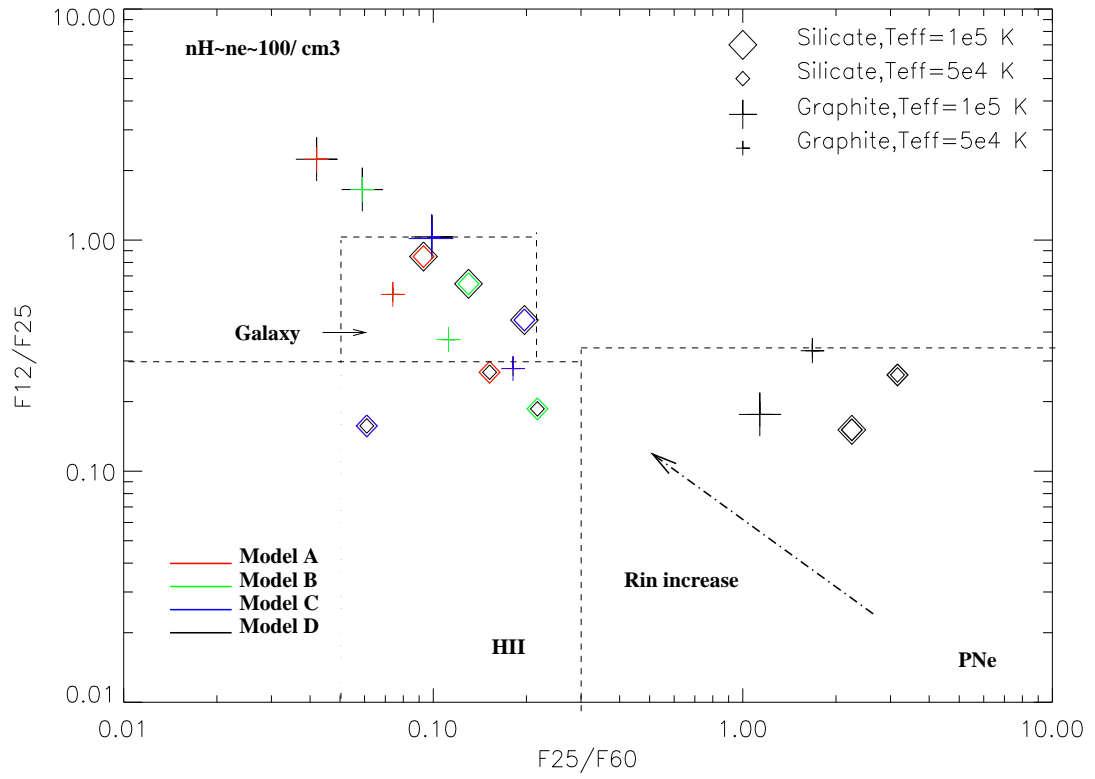
Figure 5.2: CLOUDY models for a density of 100 cm^{-3} with the Pottasch limits.

1000 cm^{-3}; and in Appendix D we show all the spectra relative to each combination modelled with CLOUDY.
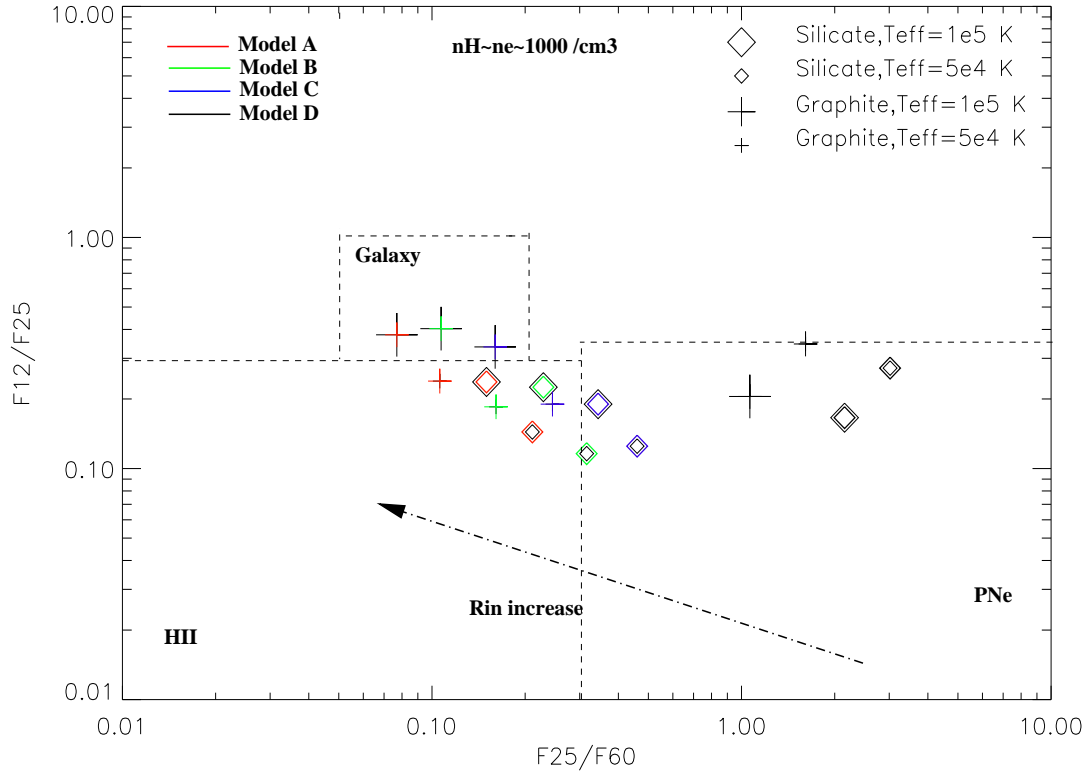
Figure 5.3: CLOUDY models for a density of 1000 cm^{-3} with the Pottasch limits.
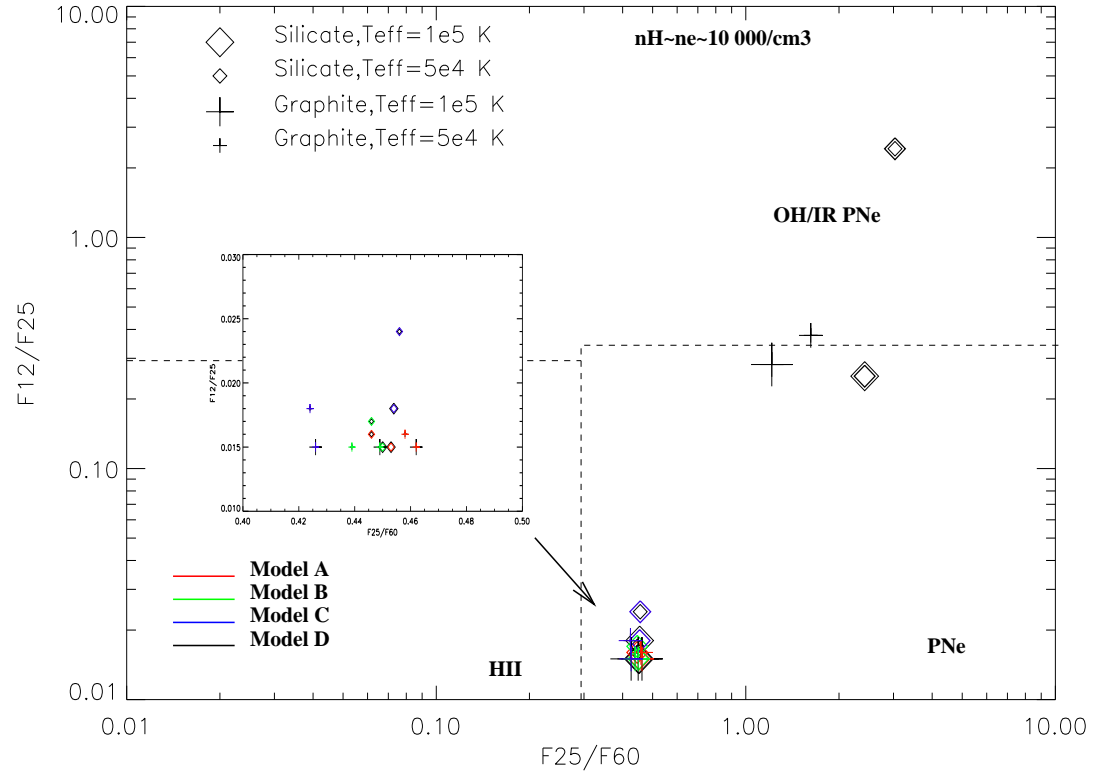
Figure 5.4: CLOUDY models for a density of 10 000 cm^{-3} with the Pottasch limits.
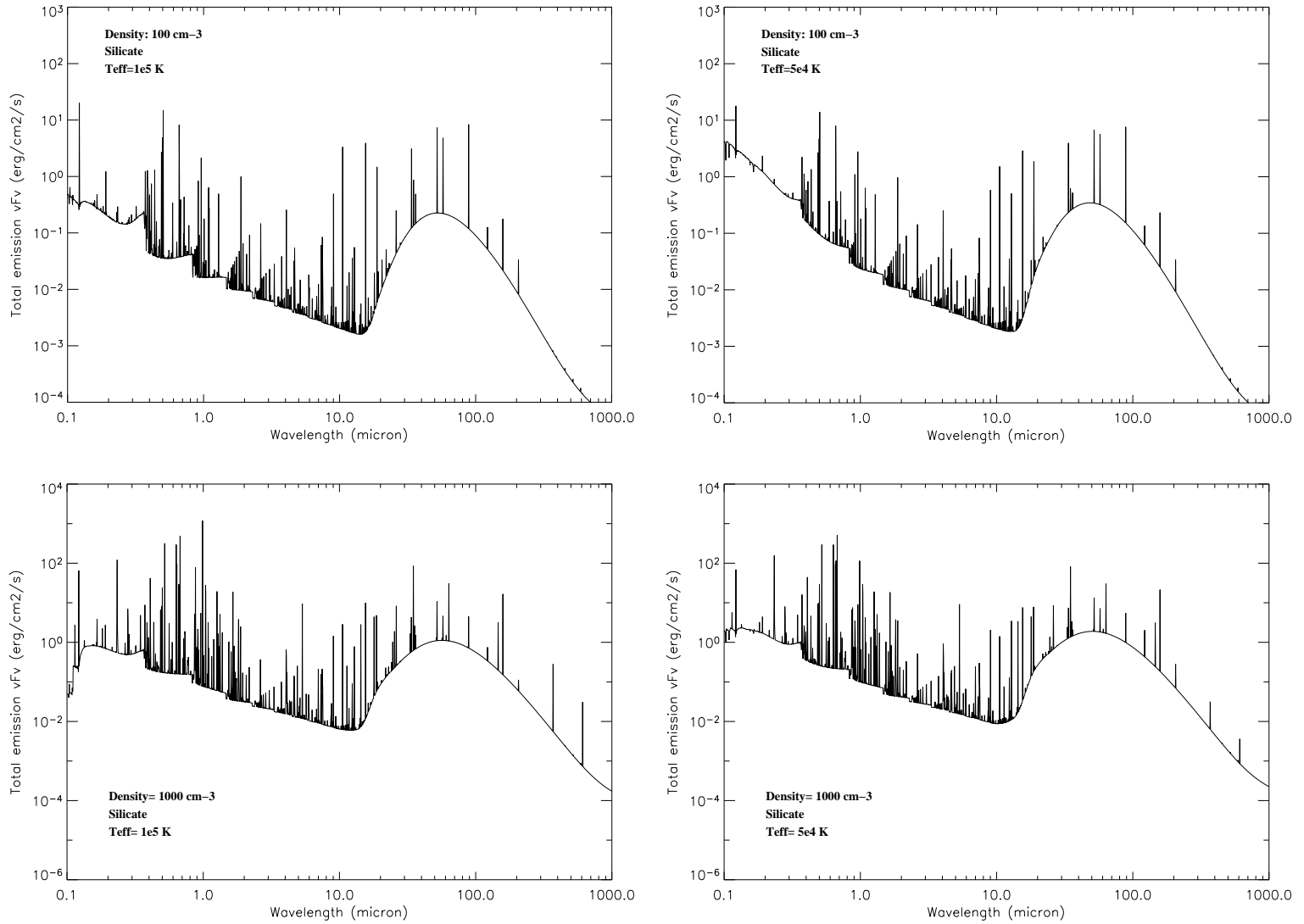
Figure 5.5: CLOUDY model A . Top for a density of 100 cm^{-3}: From left to right, Silicate & T$_{eff}$=1e5 K and Silicate & T$_{eff}$=5e4 K. Bottom: for a density of 1000 cm^{-3}: From left to right, Silicate & T$_{eff}$=1e5 K and Silicate & T$_{eff}$=5e4 K.

But we did not forget our prime goal which was the comparison between the Pottasch diagram and the IPHAS results. It appears that the only two figures which correspond with the location of IPHAS sources are the ones for densities of 100 and 1000 cm^{-3} (Fig. 5.2 and 5.3). For those densities, the best matching models are models A, B and C, i.e. with radii of 0.1, 0.05 and 0.01 pc. Therefore, we can conclude that the IPHAS nebulae fit better with large size nebulae. An other interesting point is the evolution of the radius. It appears, for a defined density, that there is a correlation between the F25/F60 flux and the size of the nebula. Indeed, a high 60μm flux (excess) is coincident with a large radius. Moreover, all 3 models (A, B and C) show a ratio lower than unity. If we examine the CLOUDY models for a density of 10000 cm^{-3} (Fig. 5.4), we can argue that large size PNe are inconsistent with high densities.

In summary, **the CLOUDY modelling has shown that the IPHAS population is characterised by medium-low density nebulae, with large sizes (from ~ 0.01 pc in radius) and a tendency for 60μm excess (or dust excess)**. This "new population of PNe" unveiled by the models, is absent from the Pottasch diagram (in the PN zone). But we do know that identified PNe have the characteristics mentioned earlier (e.g. NGC 6778, NGC 7293 "Helix nebula"), so is the diagram complete ?

In order to answer that question, we used all the PNe with IRAS measurements in the Acker catalogue (Acker et al. 1992) and plotted them as defined in IR diagram by Pottasch et al. (1988). This involved 322 PNe (Fig.5.6). We clearly see that the location of the planetary nebulae extends well above the defined limits for PNe as defined by Pottasch et al. (1988) and those nebulae mainly show a shift towards the left part of the diagram: where our missing objects are. We noticed that model D, which concerns small size nebulae (from 0.005 to ~0.01), always gives a good fit, whatever the density, for the PNe located in the PN zone by Pottasch et al. (1988). The author's diagram is therefore mainly orientated towards "small" size nebulae.
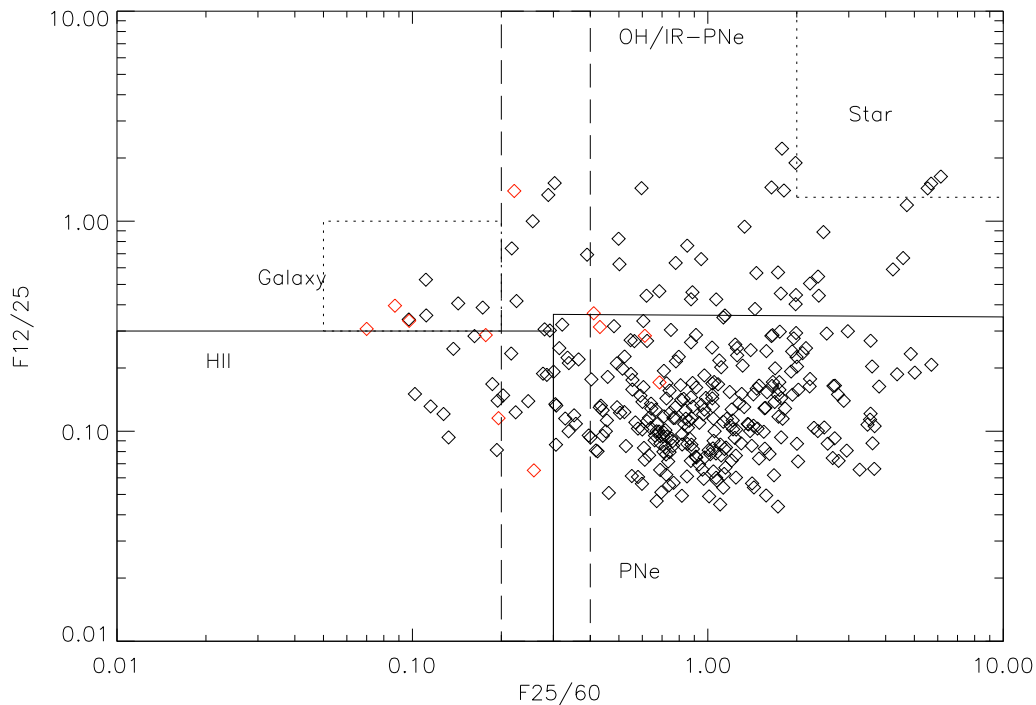
Figure 5.6: Superposition of 322 galactic PNe from (Acker et al. 1992) in the IR diagram from Pottasch et al. (1988). The IPHAS nebulae are shown in red (diamonds).

5.3 Fitting models for the IPHAS nebulae

As we have seen that, using the Pottasch diagram, we are certainly missing genuine PNe, we will use the CLOUDY results (for densities of 100 and 1000 cm^{-3}) to fit the IPHAS nebulae which were beyond all boundaries in the Pottasch diagram. These are IPHASX J192458.2+193434 (1), IPHASX J192624.7+195045 (2), IPHASX J193912.0+251105 (3) and IPHASX J195919.6+283827 (4) shown in Figure 5.7. We show in Table 5.3 the best fit obtained for the first 3 nebulae, as IPHASX J195919.6+283827 does not fit with any location on our graph. This nebula shows a lower 60μm excess but more importantly, a lack of warm dust (low 25μm flux). The best fitting model gives a minimum radius of 0.07 parsecs and an effective temperature of 100 000 K, but it also implies a much reduced nebular shell (estimated at 0.005 parsecs). In this

particular case the 12μm flux plays a large role.

Table 5.3: Best CLOUDY fits for 3 formely misclassified PNe.

N° nebula	Model at 100 cm^{-3}	Model at 1000 cm^{-3}
1,2,3	Dust : Graphite	Dust : Graphite
	T$_{eff}$: 5e4 K	T$_{eff}$: 1e5 K
	R$_{in}$: 0.1 to 0.05	R$_{in}$: 0.1 to 0.05
	Shell thickness: 0.3 to 0.4 pc	Shell thickness: 0.3 to 0.4 pc
	Mean dust temperature: 45 K	Mean dust temperature: 42 K

We compared the radii with those of the known planetary nebulae located in the same IR area. One hundred and twenty-one objects were found with a F25/F60 lower than 0.3 but only 101 have known distances. We derived a mean radius of 0.15 pc and a maximal radius of 0.48 pc. These numbers correlate well with the models.

It is interesting to notice the very good fit obtained for IPHASX J195015.9+272859 (initially classified as HII region by Pottasch et al. (1988)), which could correspond to a low density planetary nebula (100 cm^{-3}) with a central star temperature of 5e4 K, a minimum radius of 0.01 pc (Model C) and a carbon chemistry.

As we mentioned previously, the implication of the IR emission lines is likely to interfere with our results relative to the IR emission solely due to the dust. It is believed that the contribution from line emissions is smaller for wavelengths greater than ~30μm, and the contribution of the dust is dominant (Leene and Pottasch (1987), Harrington et al. (1988)). Using a standard example which involves an effective temperature of 100 000K, Silicate grains and a density of 100 cm^{-3}, we derived the emission line contribution for each model (A, B, C and D) for all four IRAS bands (Fig.5.8). Therefore, all the emission lines contained in one band have been extracted and their fluxes added up. The in-band flux obtained was then converted into flux density by
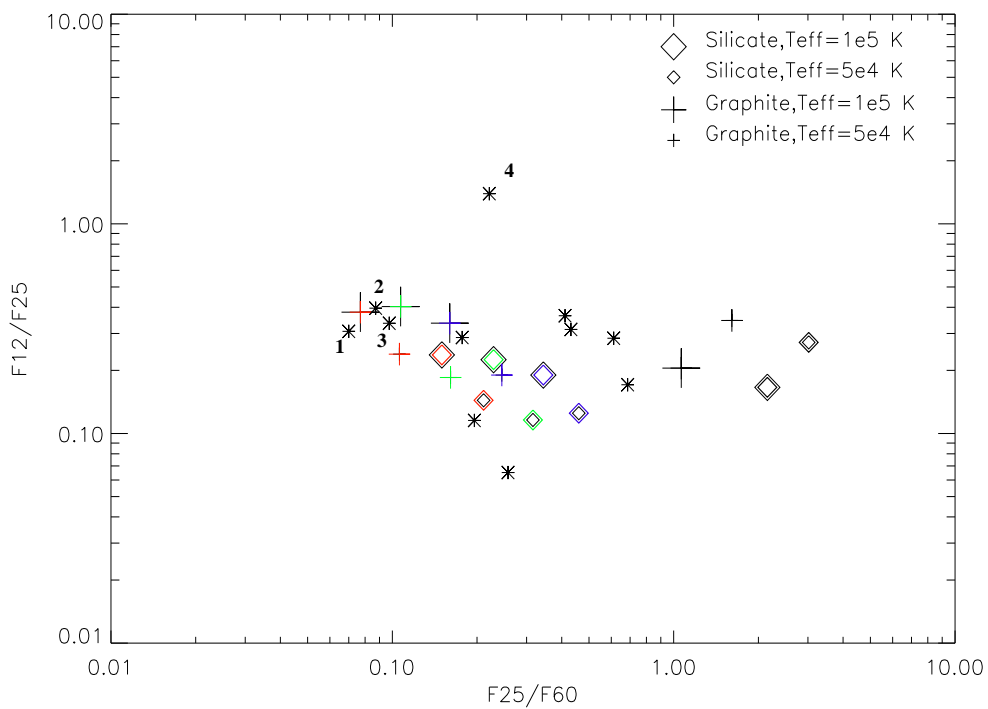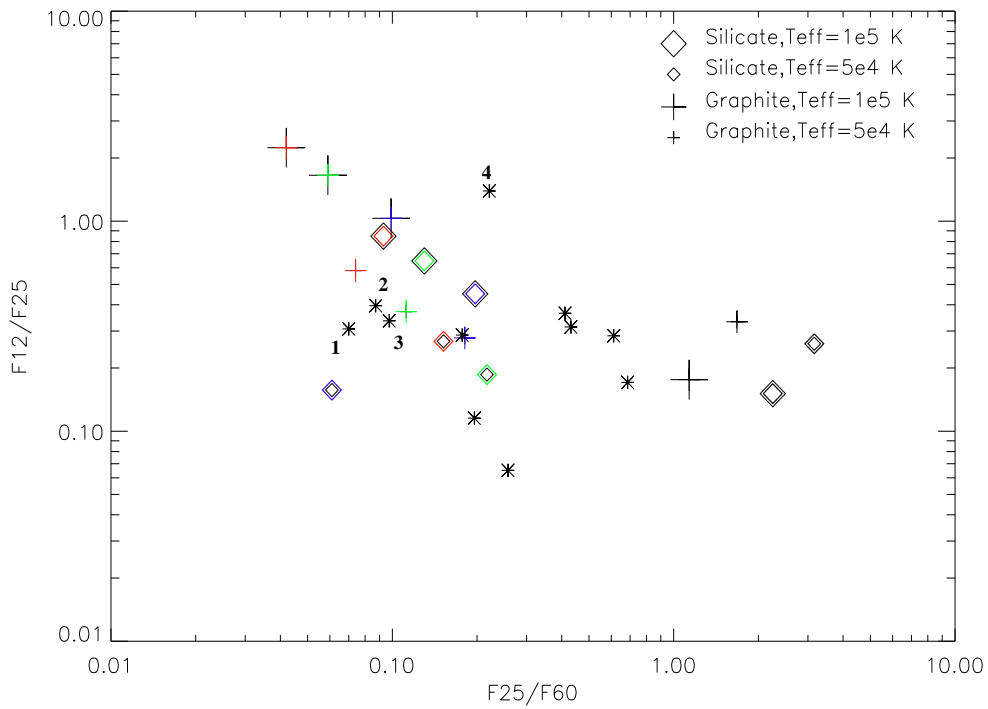
Figure 5.7: IPHAS nebulae in the CLOUDY resulting graphics for a density of 100 cm^{-3} (top) and 1000 cm^{-3} (bottom). IPHASX J192458.2+193434 (1), IPHASX J192624.7+195045 (2), IPHASX J193912.0+251105 (3) and IPHASX J195919.6+283827 (4)

dividing it by the filter width in Hz. The widths are 13.5×10^{12} Hz for the 12μm band, 5.15×10^{12} Hz for the 25μm band, 2.57×10^{12} Hz for the 60μm band and 0.994×10^{12} Hz for the 100μm band. By subtracting the emission line density flux from the flux given by CLOUDY for the whole band we obtain the dust density flux. Table 5.4 shows the ratio

$$\frac{F_{eml}}{F_{dust}}$$

with, F_{eml} the flux density of emission lines and F_{dust} the flux density of dust. The ratio shows the contribution of the emission line (over the dust) for each band.
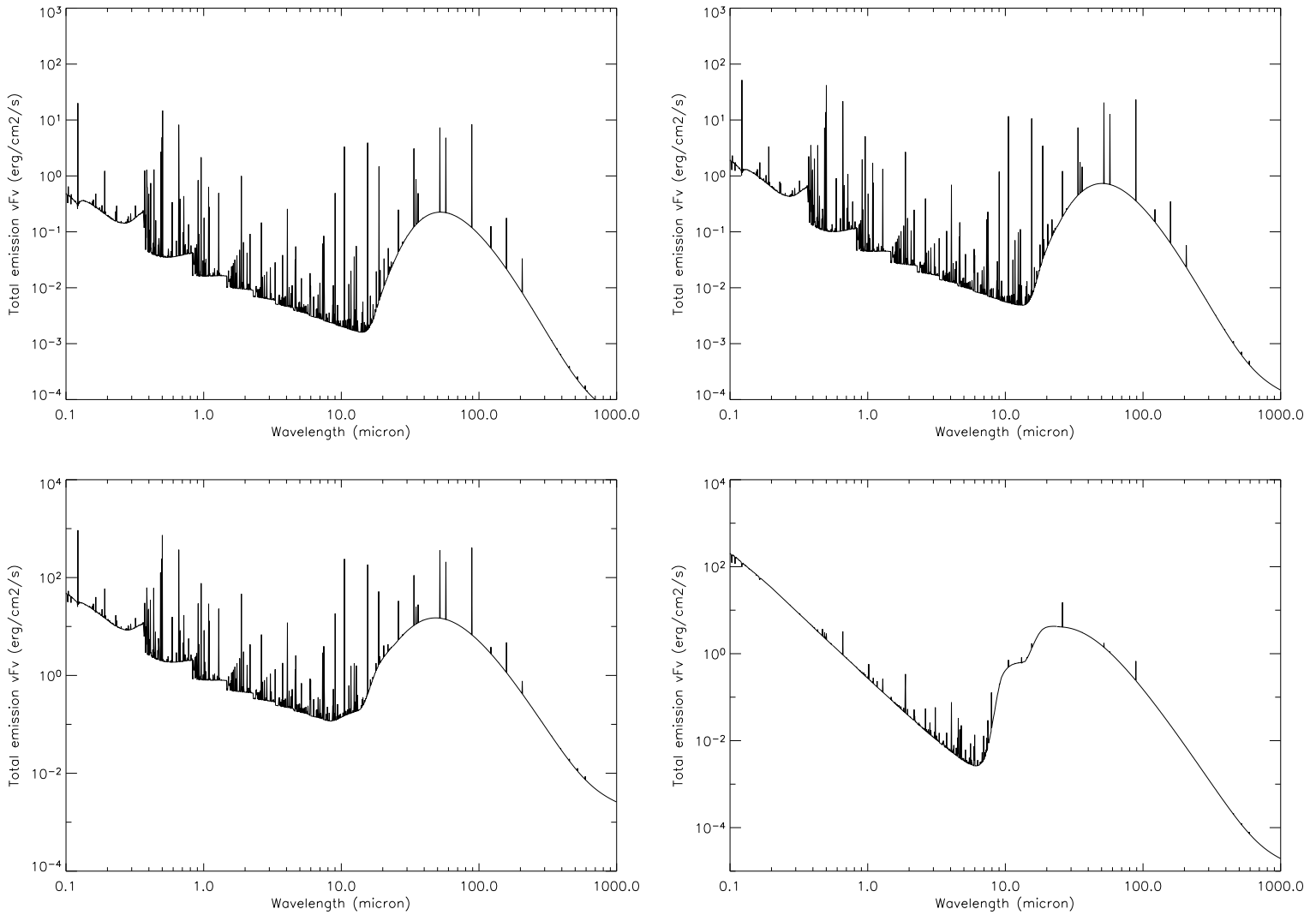
Figure 5.8: Spectra of the CLOUDY models used for the determination of the emission lines contribution. From left to right and top to bottom: model A, B, C and D.

Table 5.4: Emission line contribution for the CLOUDY models. We present the ratio of the emission line flux over the flux from the dust.

Model	12μm	25μm	60μm	100μm
A	59.6	0.10	0.28	0.88
B	123.6	0.10	0.24	0.81
C	24.7	0.06	0.20	0.77
D	6e-3	0.02	1e-3	0.02

First we notice that the 12μm band is generally dominated by emission lines. This coincides with the findings of Leene and Pottasch (1987) and Harrington et al. (1988). The exception is case D, which has the smallest radius where the dust is predominant: we therefore have hot dust. In all four models, the IR emission at 25μm, 60μm and 100μm is due to dust rather than emission lines. In the case of the 25μm band our conclusion differs from the authors previously mentioned.

5.4   Conclusion

Using the photoionisation code CLOUDY we tried to understand the systematic shift of the IPHAS nebulae towards the left part of the Pottasch diagram. This location is not considered in his IR diagram as being a zone where PNe would lie.

The different models show a **new zone** where the nebulae are consistent with medium-low density planetary nebulae (below 1000 cm^{-3}), displaying a relatively large size (with a minimum of ~ 0.01 pc in radius) and which IR emission is mainly due to the dust, except in the 12μm band (which is dominated by emission lines). The models also show the correlation between a large radius and the occurrence of a 60μm excess: dust excess is then concordant with large size PNe. Those nebulae would be less affected by the dust heating and then display cold dust. The objects showing a high 25μm flux and showing simultaneously a 60μm excess, can be explained by the fact

that warm dust (T $\gg$ 100 K) still exists near the low luminosity central star and is not totally destroyed in the ionisation area. This case has been studied in detail by van Hoof et al. (1999) for the planetary nebulae NGC 6445.

The IPHAS nebulae generally match that "forgotten population" of PNe and the 4 unclassified/misclassified objects according to Pottasch et al. (1988) and Zijlstra et al. (2001) may be genuine PNe. If we look at the CLOUDY diagrams in terms of evolution, we demonstrate that as the PNe mature, they expand in size. The change in physical conditions allows the conversion from warm to cold dust, and the lower the density the higher the dust excess. Therefore the association of large nebular radius, low density and excess of cold dust can be related to evolved PNe. IPHAS is then more likely to detect this kind of object.

By the end of this study, it appears that the Pottasch IRAS diagnostic diagram is incomplete and does not cover all PNe. This conclusion stands, when redrawing the diagram with a greater and more diverse sample of PNe. This result is important if we want to continue to use this IRAS diagram, as IPHAS is more likely to fill its left side with new objects, due to their large size (as seen previously the large size nebulae are a new population unveiled by the survey). In Figure 5.9, we show the new boundaries we established for the planetary nebulae population. We kept the limits for the HII regions and the stars as overlap is always possible. There is no clear separation between PNe and HII regions in our new graphics.
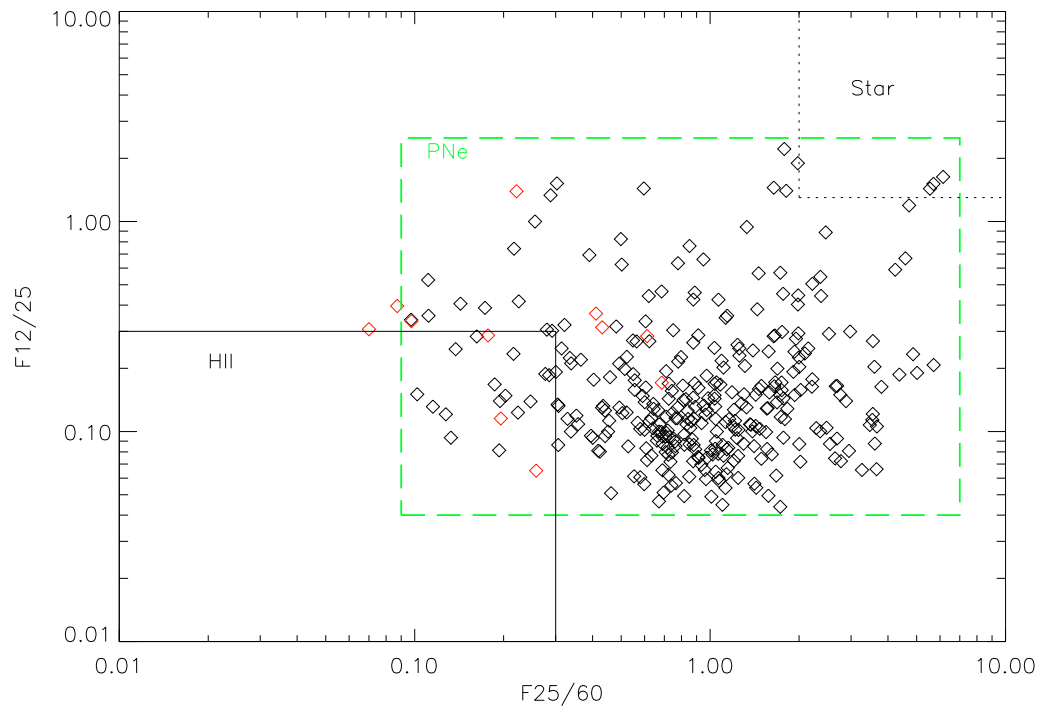
Figure 5.9: New version of the Pottasch et al. (1988) diagram, including 322 known PNe from the Acker catalogue with IR data. The red diamonds show the IPHAS nebulae.

6

Estimation of the Distances

6.1 Introduction

Distance is one of the most fundamental and difficult parameters to measure. Several methods exist to determine it, among which we can cite the trigonometric and spectroscopic parallax methods, the location in a defined "cluster" or the nebula expansion method (Liller and Liller 1968). One of the most used is the statistical "Shklovskii" method (Shklovskii 1956). The distance is obtained from the equation (Pottasch 1984):

$$d = \frac{22.8 \times M^{2/5} \times t^{-0.18}}{\epsilon^{1/5} \times F(H\beta)^{1/5} \times \theta^{3/5}} \tag{6.1}$$

with d the distance in kpc, M the mass in solar masses ($M_\odot$), t=$10^{-4}T_e$ in K, ϵ the filling factor, F(Hβ) the Hβ line flux in 10^{-11} erg cm^{-2} s^{-1}, and θ the angular radius in arcsec. This method assumes a constant ionised nebular mass for all PNe (Cahn et al. 1992) but also a constant electron density and a filling factor. The model is based on the following consideration: a PN is like a sphere filled, in the quantity ϵ, with ionised matter at a constant electron density. From this figure the flux Hβ and the distance are derived (see (Pottasch 1984) equation V-5). Still following this model the ionised mass, considered as constant, is inferred (see (Pottasch 1984) equation V-7). The combination of both equations permits us to derive the distance (which follows the initial model constraints). A modified "Shklovskii" method was proposed by Maciel and Pottasch

(1980) for high density PNe (greater than 4.10^2 cm^{-3}). A caveat in the "Shklovskii method" is the constant mass hypothesis. Indeed, due to the wide range of progenitor masses (from 0.8 to 8 M⊙), in the PNe population, it is unlikely that all PNe have the same ionised mass and this will lead to wrong estimations of the distance (Pottasch and Zijlstra 1992). But those who support this method argue that the distance is not very sensitive to the mass as it is only a 2/5 power of the mass dependence, giving an error ~30 % over the distance (Buckley and Schneider 1995). Another problem is the case of the young PNe with their high surface brightness and generally lower ionised mass. These PNe will have their distances overestimated as they are not fully ionised (i.e. they are still ionisation bounded), which means in the Shklovskii formalism that their mass is not yet constant.

Avoiding the "mass problem", van de Steene and Zijlstra (1995) defined a new statistical distance method based on the relationship between the radio surface brightness and the radius (obtained from the radio angular diameter):

$$\log R(\text{pc}) = -0.35(\pm 0.05) \log T_{\text{b}} - 0.52(\pm 0.10) \qquad (6.2)$$

$$D = \frac{R}{\theta} \qquad (6.3)$$

with R the radius in pc, θ the angular radius in arcsecond and T_b the radio brightness temperature in K. Formula 6.3 was obtained using bulge PNe. The surface brightness-radius relationship (SB-R), is a technique which has emerged in the last decade, and has been widely used in the radio regime (van de Steene and Zijlstra (1995), Zhang (1995), Schneider and Buckley (1996) and Phillips (2002)). Recently, Frew and Parker (2006) adapted this method in the optical range, using the dereddened Hα surface brightness of the PNe found during the AAO/UKIST survey.

The Shklovskii and the SB-R methods are statistical, i.e. they assume a constant parameter (respectively the ionised mass and the linear behaviour of the surface brightness regarding the radius). These assumptions can be problematic and lead to large discrepancies from one method to another. Other techniques to derive the distances

are based on individual determination (e.g trigonometric parallax). One of these is the extinction-distance method based on the comparison of nebular extinction and the E(B-V) (colour excess) of main sequence stars for which the distances are known (Kaler and Lutz 1985). We have to keep in mind that the use of individual distance methods does not guarantee better accuracy on the distances.

In this chapter we apply several methods to a set of IPHAS planetary nebulae in order first, to estimate their distance, but also to detect where the discrepancies may arise and try to understand why. Therefore we first use the SB-R method from Frew and Parker (2006), then compare the results with the "Shklovskii method" and finally with the new extinction-distance method developed within the IPHAS survey. The best objects for this study are those for which we have the spectroscopic Hα and Hβ fluxes. In this case, the 17 PNe analysed in section 3.1 will constitute our sample.

6.2   Surface brightness-radius relationship

With their new method, Frew and Parker (2006) found that the PNe were following a trend consistent with a R$^\alpha$ law with α ranging from -3 to -3.5. The variation is related to the morphology of the PNe. As mentioned previously, before applying the method to the whole set of PNe candidates, we will work on our small set of PNe.

The first step is the determination of the surface brightness of the nebulae. This process is not a simple one as we must take into account several parameters:

- If there are no spectra for the objects, the flux can be determined from the IPHAS images. But those measure Hα+[NII] and some objects exhibit a [NII] enhancement. Hence the contribution of the [NII]6583 line should not be discarded. However we have no way of correcting for it.

- Extinction should be corrected for. This flux dereddening is done using the Fitzpatrick parameterization (Fitzpatrick 1999). The algorithm inputs are the Hα

6563 line, the un-derreddened flux and the colour excess E(B-V).

- The morphology of a planetary nebula can be very complex and the full extent hard to define on a 120s Hα+[NII] image. The correct derivation of the SB should take into account the variations in flux with radius seen, for example in ring nebulae, bipolar nebulae ...etc.

- The density (and flux) increase due to ISM interaction can be misleading when measuring the surface brightness. This is even more critical if the SB has been measured via a spectroscopic determination of F(Hα) with the slit on the inter-acting rim.

- The flux determination via spectroscopy is only accurate if we consider a PN uniformly ionised. But the position and size of the slit is crucial, as we generally tend to measure the brightest part of the PN and we apply the flux to the whole nebula. According to the PN morphology, this can give a wrong SB.

When using the IPHAS images, we assume that the [NII] contribution won't affect the final surface brightness of the nebula.

To define the flux from an image, first we have to correct the image for atmospheric extinction. Then, we need to convert the counts in ADUs into fluxes. This is done by applying a conversion factor to the image. This conversion factor (cf), varies from one night to another as it is dependent on the observing condition. The definition of cf, is based on the studyof standard stars for which the magnitudes are known and therefore for which we can retrieve the flux using Pogson's law:

$$F_\nu = F_\mathrm{o} \times 10^{\frac{mag}{-2.5}} \tag{6.4}$$

with F_o the zero point flux in Hα as defined by Gonzalez-Solares et al. (2007) and Fν the flux in erg sec^{-1} cm^{-2} Hz^{-1} . For each observing night (i.e.when our nebulae have been observed), we retrieve the standard stars associated with the nebulae and we

associate the fluxes to the number of counts. Therefore in order to obtain the conversion factor for each night, we apply the following:

$$c_\mathrm{f} = \frac{F_\nu * EW}{count} \tag{6.5}$$

with "EW" the equivalent width of the filter (95 Å), "count" the data count in ADUs for each standard star to get a flux per data count. The correction for the filter transmission is done by dividing cf by the corresponding ~88 %. The conversion factor is then applied to each object using their continuum-subtracted images.

Four different ways to derive the SB were used:

- We performed a simple visual determination of the limit of the nebulae and we derive integrated fluxes. The latter is divided by the whole surface.

- We defined an expanding circular adaptive aperture, with radii increasing from the inner part of the nebulae to the outer layers. This takes into account the different geometries showed by the PNe. For each aperture, a flux and the corresponding SB were retrieved, and we took an average of all the apertures to obtain the mean SB.

- We defined the 1% contour for each nebulae. The flux was derived over the concerned area .

- We used the Hα flux from the spectroscopy, corrected from extinction. The flux was measured through a slit of ~1 arcsec width. This method is only applicable to the most compact and well defined PNe (i.e. without halo, lobes..etc). We assume therefore that there was no variation in the flux or that they were negligible. This concerns 5 PNe in our sample.

Once the SB was obtained, we used the SB-radius relationship from Frew and Parker (2006). It should be noted that they used an H-alpha surface brightness from

the spectroscopic measurement of the Hα flux alone i.e. not combined with [NII]. Around 120 calibrators were used in a wide range of surface brightness (private communication with D. Frew). The faintest calibrating PN in terms of SB is the huge, faint, one-sided nebula, TK 1 around the hot WD star Ton 320. An unpublished WHAM H-alpha integrated flux is log F(Ha) = -10.79 erg cm^{-2} s^{-1}. They adopt a distance of 570 pc from the weighted mean of trigonometric and gravity distances. Using a 42.32×10^5 arcsec^2 area they obtain log SB(Hα) = -6.68 erg cm^{-2} s^{-1} sr^{-1}. The brightest calibrators like NGC 7027 and BD+30 3639, have log SB(Hα) $\sim$ +0.1 erg cm^{-2} s^{-1} sr^{-1}. Three relations were derived from the fits and are defined according to the characteristics of the PNe.

- An overall relation, grouping all the objects: Log SB(Hα) = -3.61 log R - 5.37 (with R in parsec) and Log SB(Hα) in erg cm^{-2} s^{-1} sr^{-1}.
- A relation followed by the bipolar PNe: Log SB(Hα) = -3.37 log R - 4.87.
- A relation for the low-mass, optically thin and high excitation PNe: Log SB(Hα) = -3.16 log R - 5.78.

Frew and Parker (2006) obtained an error of ±40% on the derived distances for the general relation and ±25% on the derived distances for the 3rd category .

The resulting surface brightnesses, radii and distances are listed in Table 6.1, 6.2 and 6.3 respectively. Those results for our 17 PNe, include all four methods using the general SB-R relationship by Frew and Parker (2006) i.e. Log SB(Hα) = -3.61 log R - 5.37. We also show in Table 6.4 the radius and distance obtained using the SB-R law for the bipolar nebulae.

Table 6.1: Logarithm of the surface brightness in erg cm^{-2} s^{-1} sr^{-1} obtained via the four methods.

PN (IPHASX J)	Whole SB	Mean SB	F(Ha)Spectro	1% Contour
183911.8+010624	-1.46	-1.32	-2.03	-1.48
184336.6+034640	-1.18	-0.77	-2.69	-1.20
185224.2-004446	-1.93	-1.30	-2.49	-1.56
185525.7-004823	-1.75	-1.59	-3.34	-1.76
185925.8+001734	-1.32	-1.14	-2.63	-1.15
191124.8+002743	-2.66	-2.42		-2.13
191345.6+174752	-1.91	-1.82		-1.90
191445.1+133219	-2.89	-2.77		-2.69
192847.1+093439	-3.01	-3.06		-2.25
192902.5+244646	-2.59	-1.94		-2.59
193827.9+265752	-2.54	-2.28		-2.53
193912.0+251105	-2.42	-2.19		-1.74
194359.5+170901	-3.45	-2.83		-2.67
194751.9+311818	-1.07	-0.64		-1.00
194940.9+261521	-1.43	-1.17		-1.27
195248.8+255359	-0.65	0.12		-0.16
195657.6+265714	-2.10	-2.01		-1.79

Table 6.2: Logarithm of the radius in pc obtained via the four methods. The general fitting law, Log SB(Hα) = -3.61 log R - 5.37, is used.

PN (IPHASX J)	Whole SB	Mean SB	F(Ha)Spectro	1% Contour
183911.8+010624	-1.08	-1.12	-0.92	-1.07
184336.6+034640	-1.16	-1.27	-0.74	-1.15
185224.2-004446	-0.95	-1.12	-0.79	-1.05
185525.7-004823	-1.00	-1.04	-0.56	-0.99
185925.8+001734	-1.12	-1.16	-0.75	-1.16
191124.8+002743	-0.74	-0.81		-0.89
191345.6+174752	-0.95	-0.98		-0.96
191445.1+133219	-0.68	-0.71		-0.74
192847.1+093439	-0.65	-0.63		-0.86
192902.5+244646	-0.76	-0.94		-0.76
193827.9+265752	-0.78	-0.85		-0.78
193912.0+251105	-0.81	-0.88		-1.00
194359.5+170901	-0.53	-0.70		-0.74
194751.9+311818	-1.19	-1.30		-1.20
194940.9+261521	-1.08	-1.16		-1.13
195248.8+255359	-1.30	-1.52		-1.44
195657.6+265714	-0.90	-0.93		-0.99

Table 6.3: Distances in kpc obtained via the four methods.

PN (IPHASX J)	Whole SB	Mean SB	F(Ha)Spectro	1% Contour
183911.8+010624	5.7 ± 2.3	5.2 ± 2.2	8.1 ± 3.2	5.8 ± 2.3
184336.6+034640	1.6 ± 0.6	1.2 ± 0.5	4.1 ± 1.6	1.6 ± 0.6
185224.2-004446	11.5± 4.6	7.7 ± 3.1	16.5± 6.6	9.1 ± 3.6
185525.7-004823	3.4 ± 1.4	3.1 ± 1.2	9.4 ± 3.7	3.4 ± 1.4
185925.8+001734	2.6 ± 1.0	2.3 ± 0.9	6.0 ± 2.4	2.3 ± 0.9
191124.8+002743	2.2 ± 0.9	1.8 ± 0.7		1.5 ± 0.6
191345.6+174752	7.6 ± 3.0	7.2 ± 2.9		7.5 ± 3.0
191445.1+133219	6.5 ± 2.6	6.0 ± 2.4		5.7 ± 2.3
192847.1+093439	1.4 ± 0.6	1.5 ± 0.6		0.9 ± 0.3
192902.5+244646	7.0 ± 2.8	4.6 ± 1.8		7.0 ± 2.8
193827.9+265752	9.7 ± 3.9	8.2 ± 3.3		9.6 ± 3.8
193912.0+251105	1.6 ± 0.7	1.4 ± 0.6		1.1 ± 0.4
194359.5+170901	1.0 ± 0.4	0.7 ± 0.3		0.6 ± 0.2
194751.9+311818	3.3 ± 1.3	2.5 ± 1.0		3.2 ± 1.3
194940.9+261521	3.4 ± 1.3	2.8 ± 1.1		3.0 ± 1.2
195248.8+255359	2.0 ± 0.8	1.3 ± 0.5		1.5 ± 0.6
195657.6+265714	2.1 ± 0.8	2.0 ± 0.8		1.7 ± 0.7

Table 6.4: Log radius (pc) and distances in kpc obtained using the SB law for the bipolar nebulae.

PN (IPHASX J)	Whole SB		Mean SB		F(Ha)Spectro		1% Contour	
	LogR	Distance	LogR	Distance	LogR	Distance	LogR	Distance
184336.6+034640	-1.09	1.8 ± 0.7	-1.21	1.4 ± 0.6	-0.84	9.9 ± 3.9	-1.08	1.9 ± 0.7
185525.7-004823	-0.92	4.1 ± 1.6	-0.97	3.7 ± 1.4	-0.64	5.1 ± 2.1	-0.92	4.1 ± 1.6
191124.8+002743	-0.65	2.7 ± 1.1	-0.72	2.3 ± 0.9			-0.81	1.9 ± 0.7
191445.1+133219	-0.58	8.2 ± 3.3	-0.62	7.5 ± 3.0			-0.64	7.2 ± 2.8
192847.1+093439	-0.55	1.8 ± 0.7	-0.53	1.8 ± 0.7			-0.77	1.1 ± 0.4
194359.5+170901	-0.42	1.3 ± 0.5	-0.60	0.8 ± 0.3			-0.65	0.7 ± 0.3
194940.9+261521	-1.01	3.9 ± 1.6	-1.09	3.3 ± 1.3			-1.06	3.5 ± 1.4
195248.8+255359	-1.24	2.3 ± 0.9	-1.48	1.4 ± 0.5			-1.39	1.7 ± 0.7
195657.6+265714	-0.81	2.6 ± 1.0	-0.84	2.4 ± 1.0			-0.91	2.1 ± 0.8

The first observation we can make concerns the reliability of the distances. All four methods indicate valuable distances as they stand within the limits of ~10 kpc (we are unlikely to detect any objects above this boundary). Then, we notice a good correlation concerning the distance of each PN, generally within the error margin, using the four techniques. But we have to emphasise that although the original data on the PNe have undergone different treatments, they were all eventually applied using the same single-fitting relation.

6.3   The Shklovskii method

As mentioned earlier, this method has been widely used and assumes a constant ionised mass (M_i). We will consider M_i=0.3 $M_\odot$, a value used in the literature, although masses from 0.2 to 0.5$M_\odot$ are acceptable. The filling factor is set to 0.6. Applying equation 6.1 we found the distances quoted in Table 6.5.

We noticed that there are several inconsistent values for the distances. Indeed we did not expect PNe at larger distances than ~10 kpc. Kinman et al. (1988) noticed the same type of discrepancies for PNe with Hβ fluxes of the same order as ours (greater than $\sim 1e^{-13}$ erg cm^{-2} s^{-1})). We consider that the PNe with the largest distances are at least at ~8.5 kpc which is the distance of the Galactic centre.

We concluded that the "Shklovskii method" as presented by Pottasch (1984), was not applicable to PNe such as those discovered in the framework of the IPHAS survey. Then, this method would be limited to the "bright " PNe.

6.4   The IPHAS extinction method

In the framework of IPHAS a new method is being tested and implemented, to derive the distances by the determination of the extinction (Sales et al, in preparation). The reddening or interstellar extinction can be a good tool to determine the distances of

Table 6.5: Distances in kpc obtained with the Shklovskii method.

IPHAS PNe (IPHASX J)	FHβ (erg cm^{-2} s^{-1})	Distance (kpc)
183911.8+010624	1.35e-12	12.0 ± 3.6
184336.6+034640	2.93e-12	5.3 ± 1.6
185224.2-004446	1.88e-13	22.8 ± 6.8
185525.7-004823	1.24e-13	12.8 ± 3.8
185925.8+001734	2.70e-12	6.9 ± 2.1
191124.8+002743	1.35e-15	16.9 ± 5.1
191345.6+174752	1.96e-14	28.1 ± 8.4
191445.1+133219	9.01e-17	51.8 ± 15.5
192847.1+093439	6.64e-17	21.2 ± 6.3
192902.5+244646	1.33e-15	35.4 ± 10.6
193827.9+265752	9.47e-16	46.9 ± 14.1
193912.0+251105	9.69e-15	10.7 ± 3.2
194359.5+170901	7.23e-16	8.9 ± 2.7
194751.9+311818	1.61e-13	15.5 ± 4.6
194940.9+261521	1.49e-14	21.8 ± 6.5
195248.8+255359	4.28e-13	11.1 ± 3.3
195657.6+265714	1.45e-15	20.7 ± 6.2

objects in the Galactic Plane. If we know the apparent and absolute magnitudes of field stars surrounding our nebulae we can determine an extinction-distance law in the direction of the PNe.

All the stars (A0 to K4) detected in IPHAS were placed in a r-Hα vs r-i colour-colour diagram. They described a curve which moves for different values of the reddening E(B-V). The bump of those curves describe a line called the early-A reddening line (Fig. 6.1) as they are relative to the early A-stars. Each position on this line is therefore linked to an extinction. The early A-stars are the ones used for the extinction-distance

method, although in practise all stars from A0 to K4 are used. Drew et al. (2008) shows how the high Hα absorption of the early A-stars made them identifiable in the IPHAS r-Hα vs r-i colour-colour diagram. Their extinctions are derived from their r-i colour and their distances are obtained from the photometric parallax method.

For each star, the distance, extinction and colours are obtained and the data are binned to give an extinction-distance relation. The luminosity class can be retrieved from the chosen extinction curve, the extinction to the stars and their apparent magnitude m_V. The apparent magnitude is obtained from the IPHAS photometric measurements. As the luminosity class and spectral type of the object are now known, the absolute magnitude M_V of the stars and then an estimate of their distance are found, as well as their extinction and colours. These new estimations are part of a repeated process which lasts until convergence of the results. The distances at different extinction values can be derived. We use the standard equation:

$$m_V - M_V = 5 \log d + R \times E(B - V) - 5 \qquad (6.6)$$

with R the reddening coefficient assumed constant (R=3.1) as the A-stars are localised in a small area around the concerned nebula.

By retrieving the nebular extinction, generally by spectroscopic means (Balmer decrement) we can obtain the PNe distance and compare it to the extinction-distance of the A-stars surrounding it in the same line of sight. This method depends on the accuracy of the photometric measurements, the presence of contaminants like O and B stars and in our case, on the structure of the nebula (if there is a variation of the extinction due to the geometry). Hence, the distance estimation could be erroneous if the extinction is intrinsic to the PN and does not affect the surrounding stars.

6.4.1 Application to the IPHAS PNe

The extinction curves have been produced by the IPHAS group dealing with the A-type stars (which also developed the algorithm to produce them). We used the preliminary
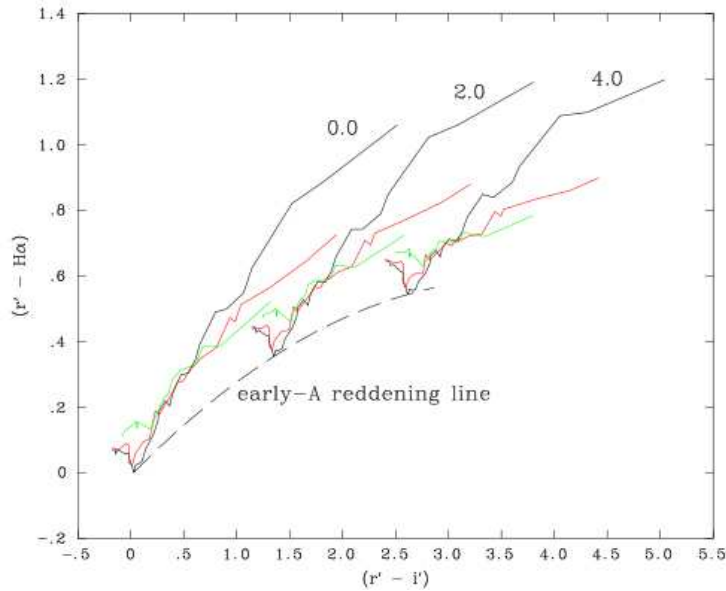
Figure 6.1: The effect of interstellar extinction, calculated according to an R = 3.1 Galactic law, on synthetic stellar tracks in the (r-Hα, r-i) plane. The main sequences are drawn in black, the giant sequences in red, and supergiants in green. The three sets shown apply to E(B-V) = 0.0, 2.0 and 4.0, as labelled. The dashed line shown is the reddening locus for A0V stars. This defines a notional minimum line for all non-degenerate stars. It is named the "early-A reddening line". The figure and the text have been taken from Drew et al. (2005) with authorisation of the author.

diagrams to give an estimation of the PNe distances (see Fig. 6.2). As said previously, the curves show the distribution of the extinction as a function of the distance. The A-stars used for each diagram have been binned up (100 pc bins). For each line of sight, at least two fields' stars were used (as we have to take into account the offset during the observations).

The results for the 17 spectroscopically investigated IPHAS PNe, are shown in Table 6.6. The errors on the distances are derived from the error on the visual extinction. But as our targets are in an area of heavy extinction the accuracy of the extinction curves can be low (we rely on upper and lower limits) and therefore the error on the distance

is large. By contrast, the figures in Appendix C.2 show the extinction curves for PNe observed in a less obscured region (RA between 20h and 00h) where a distance is always well determined. In our case, out of 17 targets, 9 show a good fit and therefore we can have confidence in their accuracy.

Table 6.6: Extinction and distances of a set of IPHAS nebulae. The (*) shows nebulae with extinction much higher than the field stars visual extinction. *ul* indicates that the distance is the upper limit and *ll* indicates that the distance is the lower limit. The accuracy on c(Hβ) depends on the observing conditions and the data reduction process.

| Name	c(Hβ)	A(V)	d (kpc)	Morphology	Height $|z|$ (pc)
IPHASX J183911.8+010624	2.71	5.67	0.7^{-ul}_{+1}	R	41
IPHASX J184336.6+034640	2.17	4.45	$2.2^{-0.5}_{+1}$	B	132
IPHASX J185224.2-004446	2.56	5.32	$5.2^{-2}_{+0.5}$ *	R	50
IPHASX J185525.7-004823	1.93	3.92	$1.7^{-0.9}_{+2.5}$	B	37
IPHASX J185925.8+001734	3.73	8.08	$3.7^{-1.6*}_{+ll}$	E	106
IPHASX J191124.8+002743	1.32	2.62	4.7^{-3}_{+ll}	B	349
IPHASX J191345.6+174752	2.30	4.74	$2.7^{-1.6}_{+2.5}$	R	155
IPHASX J191445.1+133219	1.60	3.21	$0.8^{-ul}_{+0.9}$	B	15
IPHASX J192847.1+093439	0.97	1.90	$1.3^{-1.0}_{+1.7}$	B	86
IPHASX J192902.5+244646	0.88	1.72	$2.2^{-0.5}_{+1.5}$	R	131
IPHASX J193827.9+265752	0.89	1.74	2.2^{-1}_{+2}	R	102
IPHASX J193912.0+251105	2.21	4.54	$5.7^{-1.5*}_{+ll}$	I	157
IPHASX J194359.5+170901	0.38	0.72	$0.3^{-ul}_{+0.6}$	B	18
IPHASX J194751.9+311818	2.79	5.85	$5.7^{-2}_{+0.5}$ *	R	296
IPHASX J194940.9+261521	2.70	5.64	$6.7^{-4}_{+0.5}$ *	B	7
IPHASX J195248.8+255359	3.93	8.58	$3.7^{-1.3*}_{+ll}$	B	47
IPHASX J195657.6+265714	3.05	6.45	$5.9^{-0.8*}_{+2.4}$	B	101
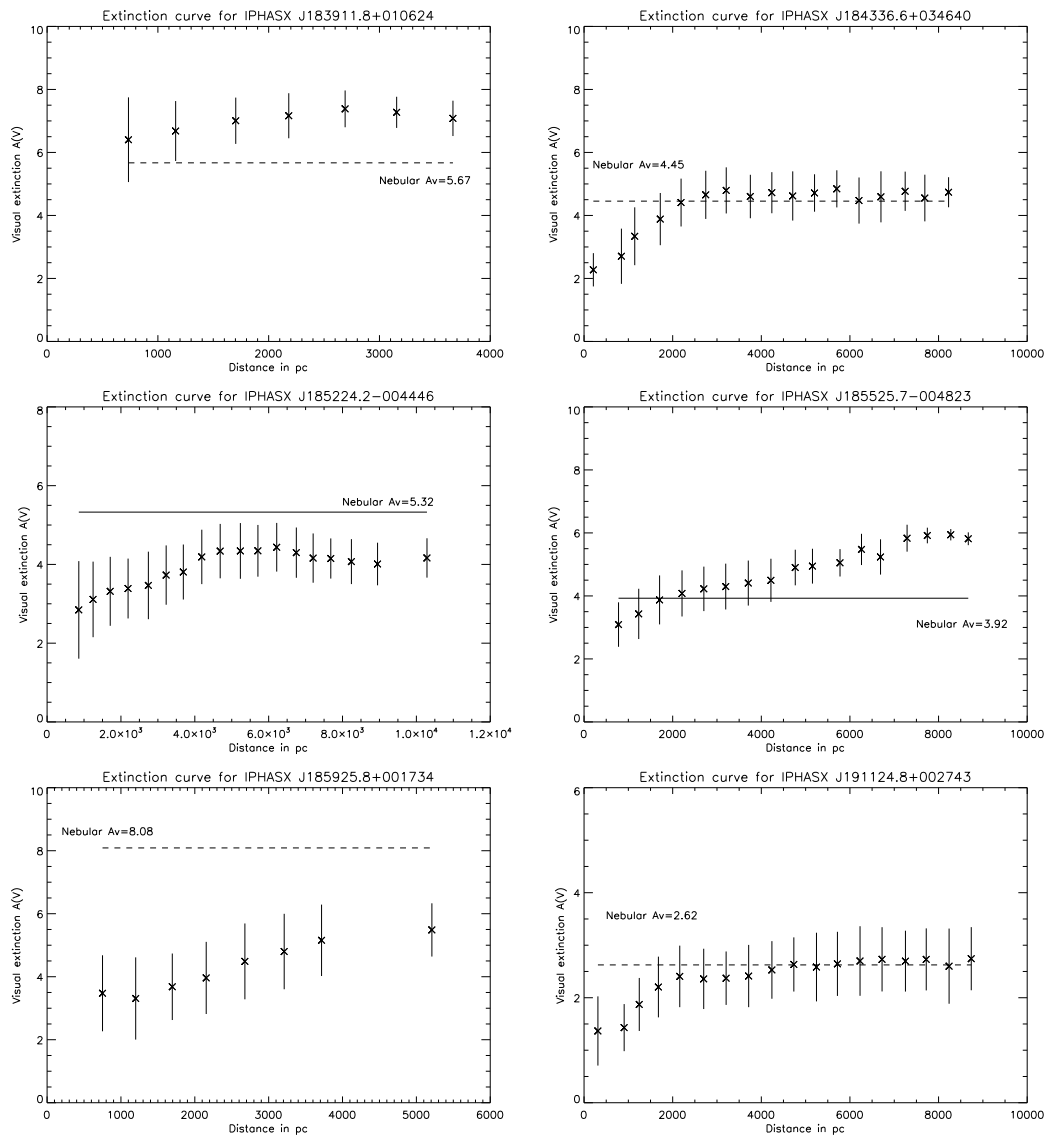
Figure 6.2: Extinction curves of the main sequence stars in the direction of each of the nebulae giving their distances.
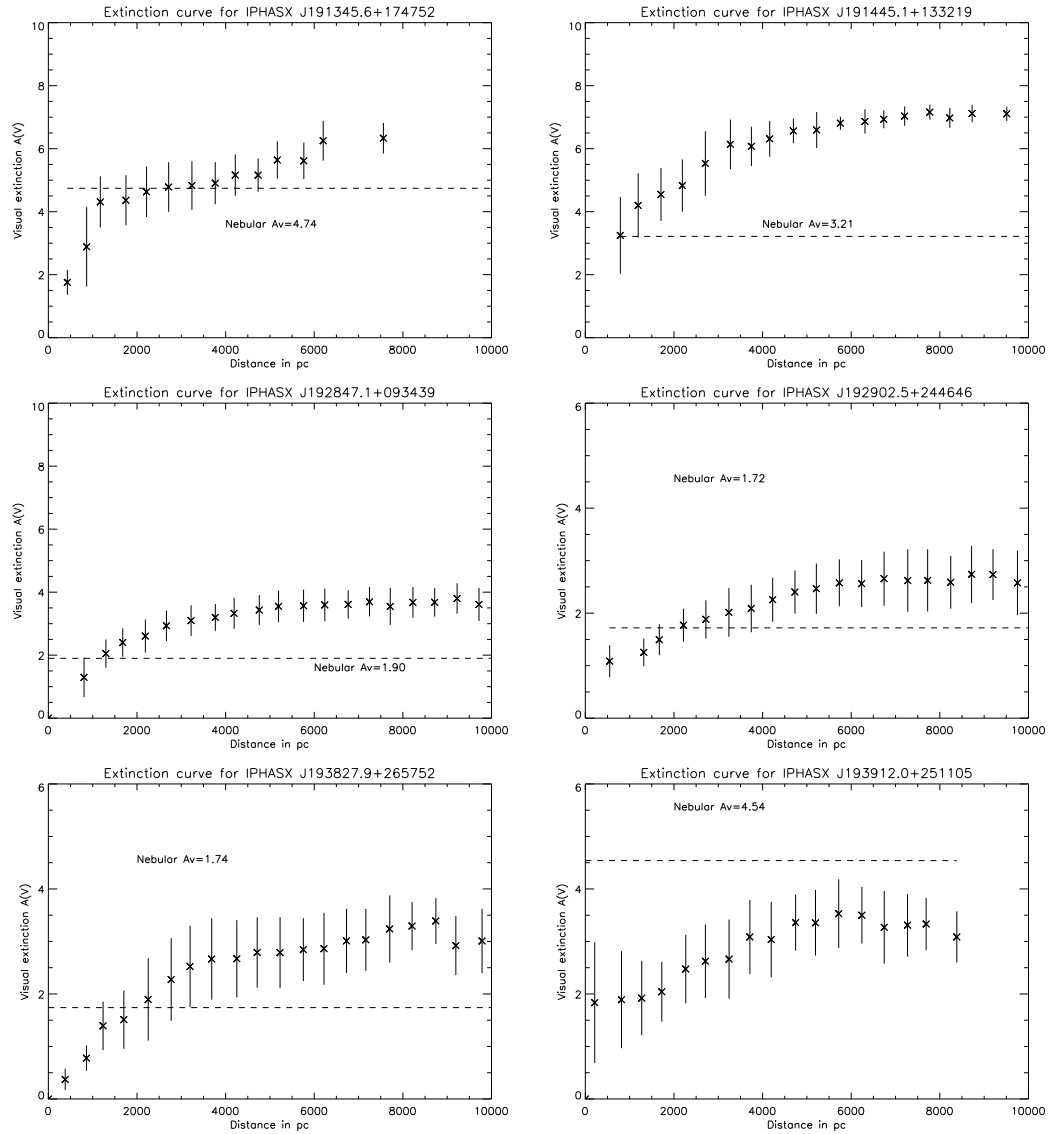
Figure 6.2 (continued)
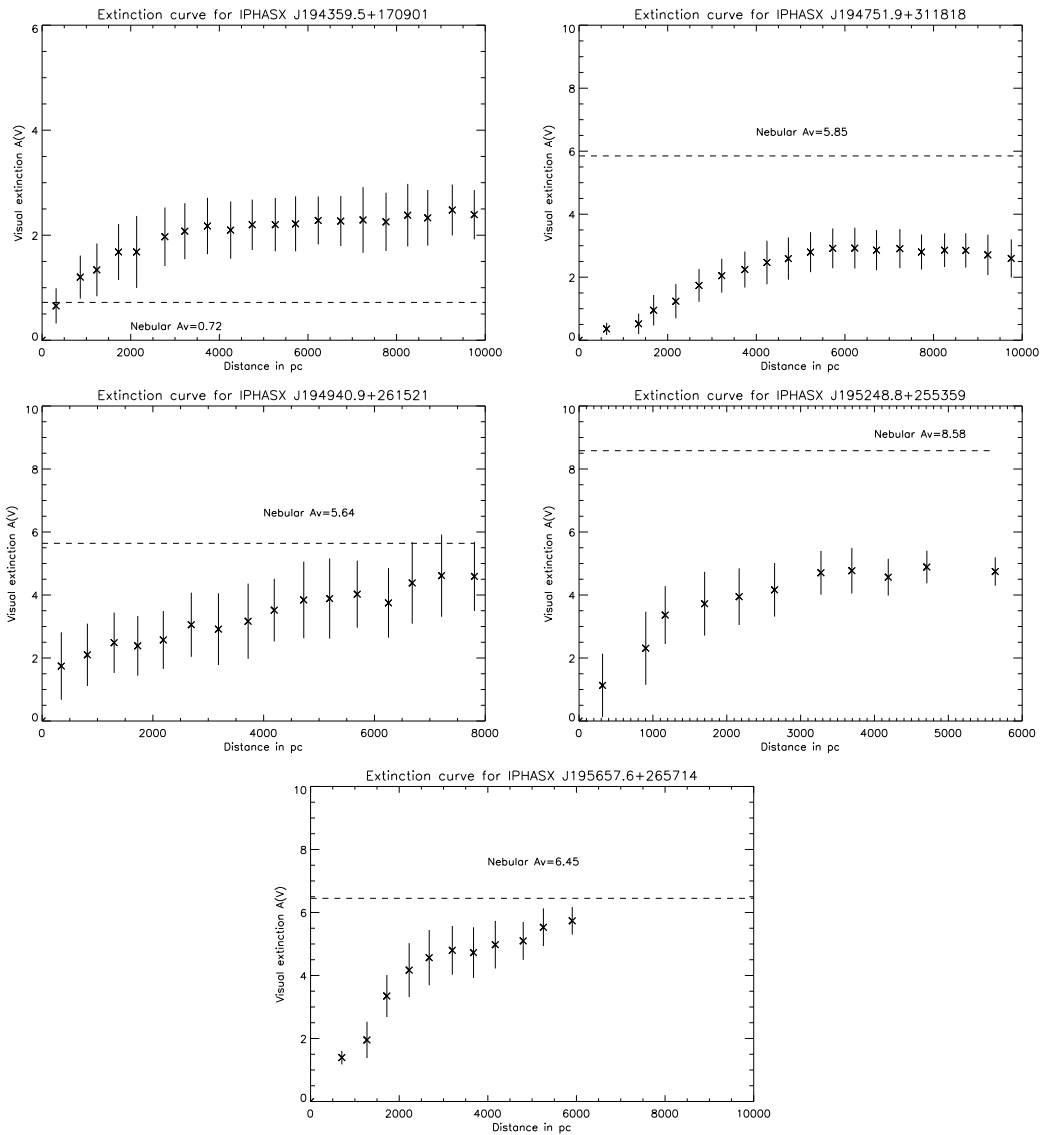
Figure 6.2 (continued)

6.4.2 Accuracy of the method

We observed that some PNe have reddening greater than their associated reddening-distance curve. This poses the problem of the accuracy of the new IPHAS method. As seen previously the extinction-distance method relies first on the photometry (for the A stars) and on the estimation of the extinction for the nebulae. We assume that the precision of the photometry is not significant as the accuracy is about 1 to 2%. A vari-

ation of extinction in the A-stars' field is possible if the surrounding field stars are in a particularly "turbulent" area i.e. with large HII regions, SNRs or clusters where the extinction is subject to (large) variations. But the error bars on the curves are not large enough to fully confirm this possibility. The errors in the distance determination might therefore come from the objects observed i.e. in our case the PNe and more precisely their internal extinction. The geometry of the PN and the way we derive the extinction play a major role in the accuracy of the distances. As said earlier, the intrinsic extinction of the PN may be a problem as it may vary inside the PN. This would therefore particularly affect large nebulae. As an example we observed the possible variation in extinction in the large bipolar IPHASX J192847.1+093439 (Fig. 6.3). The data were measured along the slit over a 2.9 arcmin length. Together with Fig. 6.4, we can see that the extinction is roughly uniform across the nebula. The two peaks in the Hα/Hβ ratio are due to the presence of bright stars on the slit. Therefore we can say that not only large variations of extinction inside a PN is not likely but also, if they appear, the presence of foreign bodies on the slit is likely. The precise determination of the nebular extinction is an important aspect for determining the accuracy of the distance.
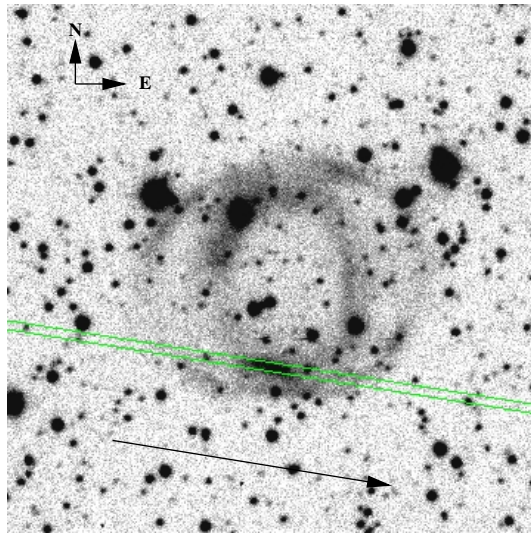
Figure 6.3: IPHASX J192847.1+093439: Position of the slit on the PN, the arrow indicates the direction for reading the data i.e. towards the East.
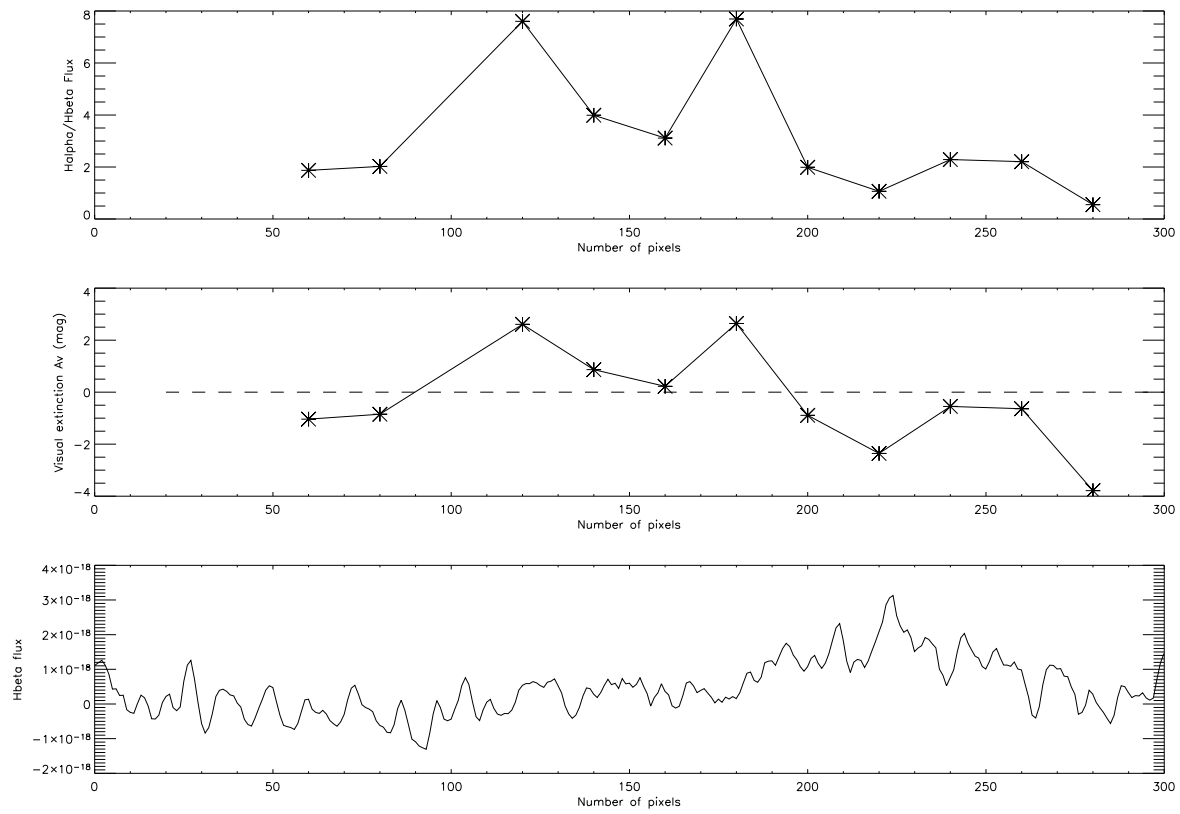
Figure 6.4: Variation of the Hα/Hβ ratio, visual extinction Av and Hβ flux (in erg/cm^2/s/Å) inside the planetary nebula IPHASX J192847.1+093439.

6.5 Discussion

6.5.1 Comparison of the methods

Now that we have retrieved the distances by three different means, we need to compare the results of the methods used. The distances are summarised in Table 6.7 and the radii in Table 6.8 (we do not include the Shklovskii results in this last table, as they would give incoherent values for the radius).

Table 6.7: Distances in kpc obtained via the four methods. "+" indicates a non convergence towards a distance.

| PN (IPHASX J)	Whole SB	Mean SB	F(Ha)Spectro	1% Contour	Extinction	Shklovskii
183911.8+010624	5.7 ± 2.3	5.2 ± 2.2	8.1 ± 3.2	5.8 ± 2.3	0.7^{-ul}_{+1}	12.0 ± 3.6
184336.6+034640	1.6 ± 0.6	1.2 ± 0.5	4.1 ± 1.6	1.6 ± 0.6	$2.2^{-0.5}_{+1}$	5.3 ± 1.6 / 5.5 ± 1.7
185224.2-004446	11.5± 4.6	7.7 ± 3.1	16.5± 6.6	9.1 ± 3.6	$5.2^{-2}_{+0.5}$ +	22.8 ± 6.8
185525.7-004823	3.4 ± 1.4	3.1 ± 1.2	9.4 ± 3.7	3.4 ± 1.4	$1.7^{-0.9}_{+2.5}$	12.8 ± 3.8 / 26.9 ± 8.0
185925.8+001734	2.6 ± 1.0	2.3 ± 0.9	6.0 ± 2.4	2.3 ± 0.9	$3.7^{-1.6}_{+ll}$ +	6.9 ± 2.1
191124.8+002743	2.2 ± 0.9	1.8 ± 0.7		1.5 ± 0.6	4.7^{-3}_{+ll}	16.9 ± 5.1 / 258.2± 77.4
191345.6+174752	7.6 ± 3.0	7.2 ± 2.9		7.5 ± 3.0	$2.7^{-1.6}_{+2.5}$	28.1 ± 8.4 / 67.8 ± 20.3
191445.1+133219	6.5 ± 2.6	6.0 ± 2.4		5.7 ± 2.3	$0.8^{-ul}_{+0.9}$	51.8 ± 15.5
192847.1+093439	1.4 ± 0.6	1.5 ± 0.6		0.9 ± 0.3	$1.3^{-1.0}_{+1.7}$	12.7 ± 3.8
192902.5+244646	7.0 ± 2.8	4.6 ± 1.8		7.0 ± 2.8	$2.2^{-0.5}_{+1.5}$	35.4 ± 10.6
193827.9+265752	9.7 ± 3.9	8.2 ± 3.3		9.6 ± 3.8	2.2^{-1}_{+2}	46.9 ± 14.1
193912.0+251105	1.6 ± 0.7	1.4 ± 0.6		1.1 ± 0.4	$5.7^{-1.5}_{+ll}$ +	10.7 ± 3.2 / 96.4 ± 28.9
194359.5+170901	1.0 ± 0.4	0.7 ± 0.3		0.6 ± 0.2	$0.3^{-ul}_{+0.6}$	8.9 ± 2.7 / 352.8 ± 105.8
194751.9+311818	3.3 ± 1.3	2.5 ± 1.0		3.2 ± 1.3	$5.7^{-2}_{+0.5}$ +	15.5 ± 4.6 / 23.6 ± 7.1
194940.9+261521	3.4 ± 1.3	2.8 ± 1.1		3.0 ± 1.2	$6.7^{-4}_{+0.5}$ +	21.8 ± 6.5 / 77.7 ± 23.3
195248.8+255359	2.0 ± 0.8	1.3 ± 0.5		1.5 ± 0.6	$3.7^{-1.3}_{+ll}$ +	11.1 ± 3.3 / 14.5 ± 4.3
195657.6+265714	2.1 ± 0.8	2.0 ± 0.8		1.7 ± 0.7	$5.9^{-0.8}_{+2.4}$ +	20.7 ± 6.2
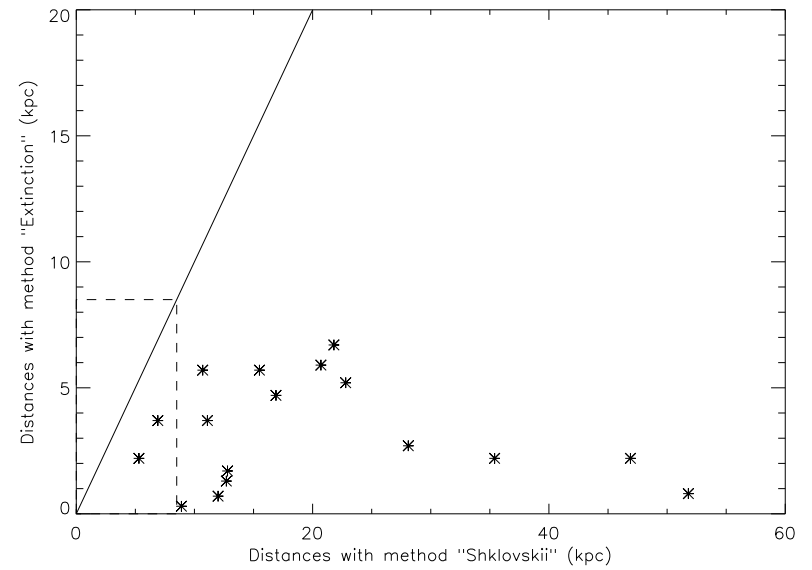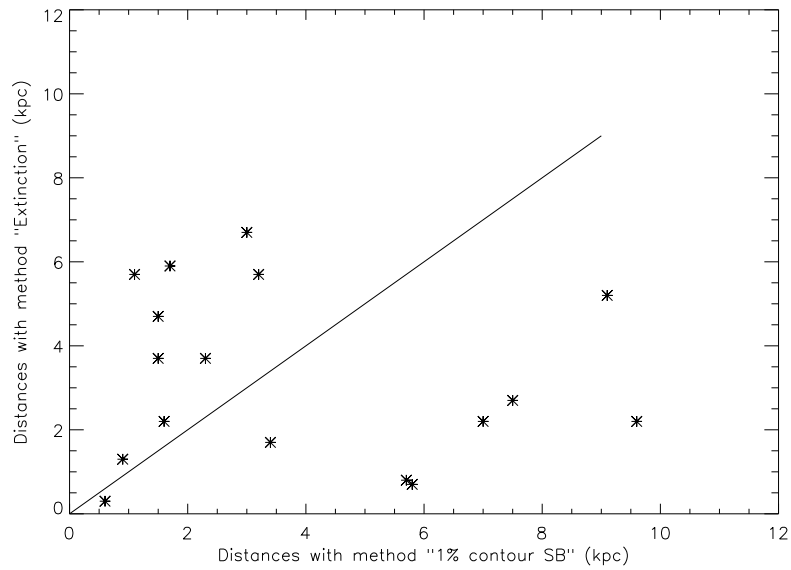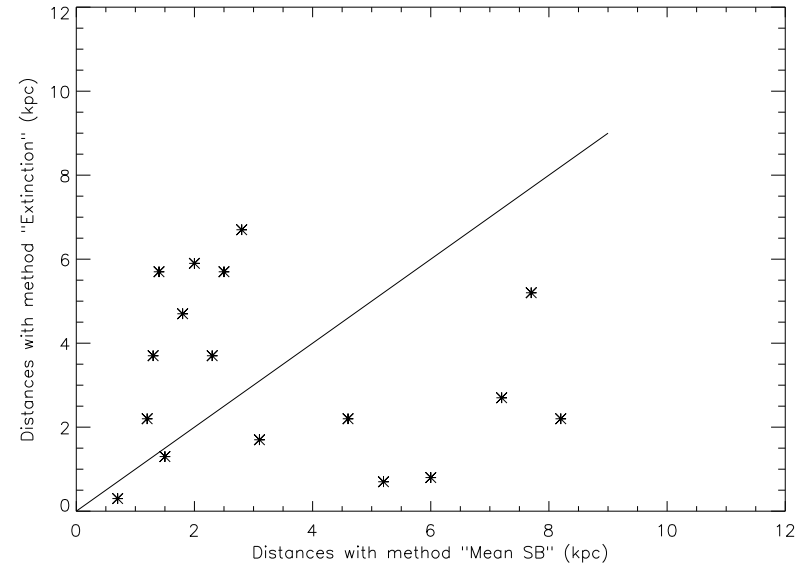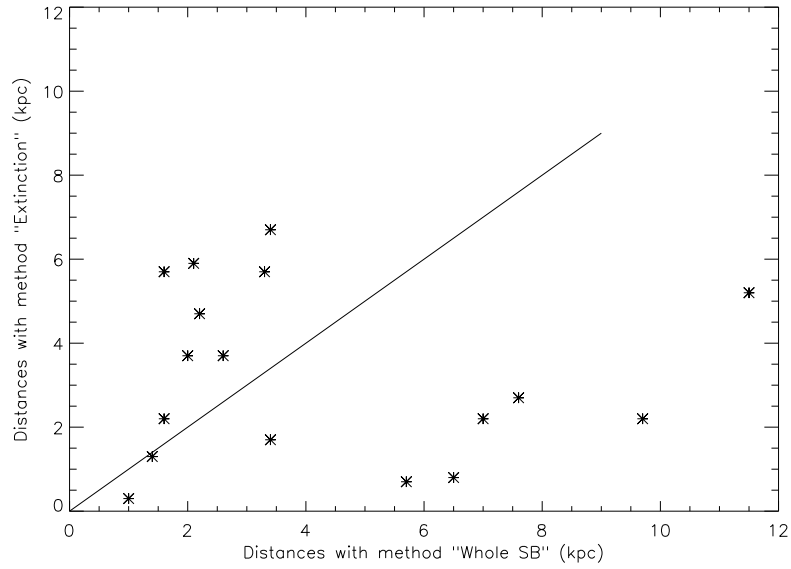
Figure 6.5: Comparison of the SB methods with the extinction method. The dash limits show 8.5 kpc.
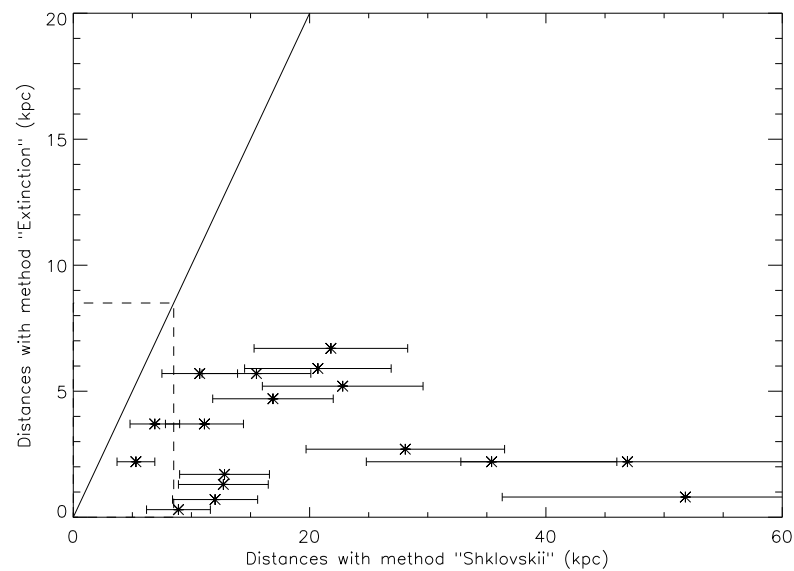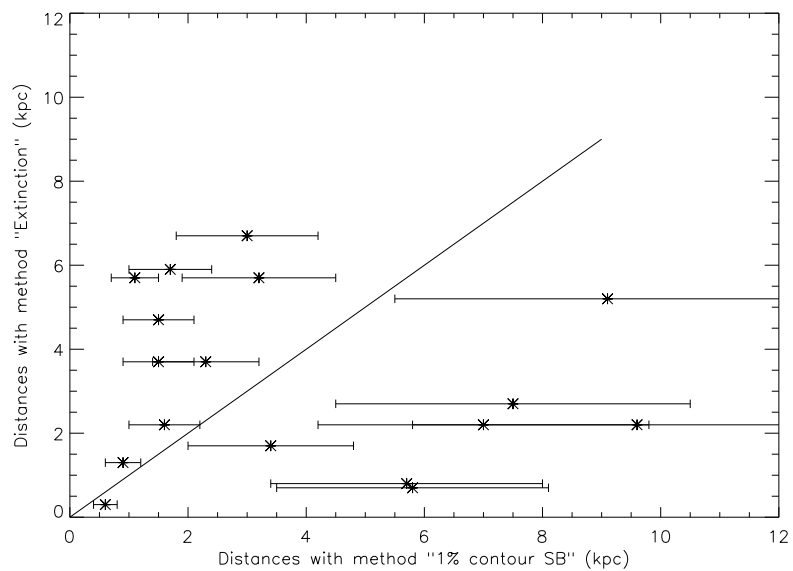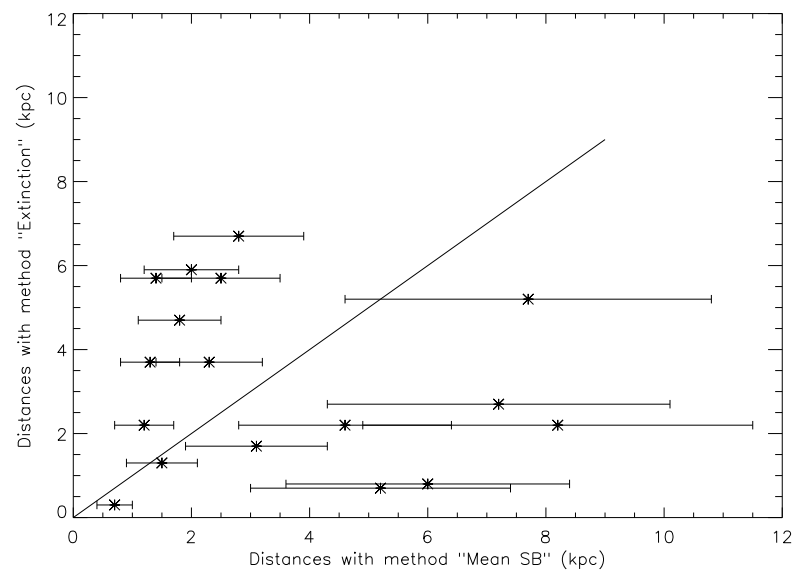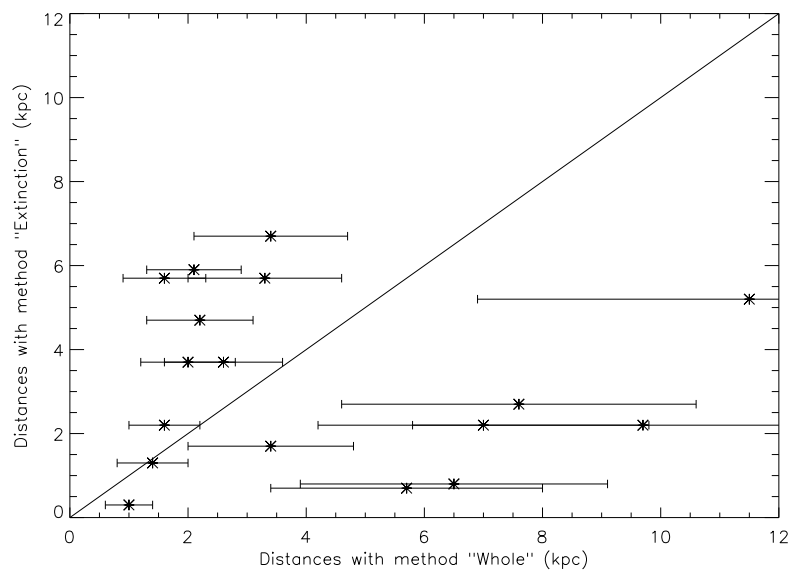
Figure 6.6: Comparison of the SB methods and their errors with the extinction method. The dash limits show 8.5 kpc.

Except for the unreliable distances given using the "Shklovskii method"(Fig.6.5 and Fig.6.6, Bottom right), we see that there is no huge variation among "whole", "mean" and "1%contour" surface brightness detection methods regarding the final distance determination. Including the spectroscopy and the extinction methods, all five techniques are generally consistent within the margins of error, otherwise few exact agreements are found using canonical values. In terms of accuracy of the processes we can classify these methods into two groups: those providing a precise area and those providing a precise flux. The visual search for the PN delimitation (whole SB) as well as the 1% contour method do not take into account the geometry of the PN. Therefore noise and additional fluxes are added (the continuum subtraction is not always perfect) and the areas corresponding to these non-useful parts are also taken into account in the calculations. The use of adaptive apertures which fit the change in geometry inside the PN (mean SB), gives a more reliable estimation of the effective areas involved in the surface brightness calculations and by extension the associated fluxes. Concerning the accuracy of the flux estimation, the use of spectroscopy appears the best way to operate. But the caveat, as said before, is the morphology of the PN. Indeed, we can only apply the fluxes derived from our long slit spectroscopy studies, to the most compact and "simply shaped" PNe. The use of integral field spectroscopy, which can give the flux at all locations in the PN, would be the best (flux and area determination). Therefore a good estimation of the surface brightness is obtained:

• With the spectroscopy: Using a Hα integrated spectrum on the whole PN which is better obtained with integral field spectroscopy.

• With the imaging: Using a narrow-band filter in Hα and the averaged surface brightness method. The ideal would be a wavelet analysis study, which would "sample" the images in different areas and levels of brightness and give a more reliable value of SB.

If we compare the mean SB method results to those obtained by the IPHAS extinction-distance method, we see that the agreement is not systematic (Fig.6.5 and Fig.6.6, Top right). Taking into account the error margins, 12 PNe show a relatively good agreement. And it is interesting to note that among these 12 PNe, four have a non-

Table 6.8: Logarithm of the radius in pc obtained via the four SB-R methods and the extinction-distance method. The general fitting law, Log SB(Hα) = -3.61 log R - 5.37, is used.

PN (IPHASX J)	Whole SB	Mean SB	F(Ha)Spectro	1% Contour	Extinction
183911.8+010624	-1.08	-1.12	-0.92	-1.07	-1.99
184336.6+034640	-1.16	-1.27	-0.74	-1.15	-1.01
185224.2-004446	-0.95	-1.12	-0.79	-1.05	-1.29
185525.7-004823	-1.00	-1.04	-0.56	-0.99	-1.30
185925.8+001734	-1.12	-1.16	-0.75	-1.16	-0.96
191124.8+002743	-0.74	-0.81		-0.89	-0.41
191345.6+174752	-0.95	-0.98		-0.96	-1.40
191445.1+133219	-0.68	-0.71		-0.74	-1.59
192847.1+093439	-0.65	-0.63		-0.86	-0.69
192902.5+244646	-0.76	-0.94		-0.76	-1.27
193827.9+265752	-0.78	-0.85		-0.78	-1.42
193912.0+251105	-0.81	-0.88		-1.00	-0.27
194359.5+170901	-0.53	-0.70		-0.74	-1.05
194751.9+311818	-1.19	-1.30		-1.20	-0.95
194940.9+261521	-1.08	-1.16		-1.13	-0.78
195248.8+255359	-1.30	-1.52		-1.44	-1.04
195657.6+265714	-0.90	-0.93		-0.99	-0.46

convergence of their extinction in the IPHAS curves, and only a lower limit is assumed for their distance. The 5 PNe with no agreement are IPHASX J183911.8+010624, IPHASX J191445.1+133219,IPHASX J193912.0+251105, IPHASX J195248.8+255359 and IPHASX J195657.6+265714. A source of error could be in the determination of the extinction in the PN.

There is no obvious common factor which could explain why some objects have a relatively consistent distance using all the techniques nor why some large discrepancies exist. The two parameters that come to mind are the size and the morphology of the PNe.

Is the (dis)agreement on the distances linked to the size of the PNe ? Nothing suggests that such a link exists. We can find small and large size PNe with relatively concordant distances among the majority of the methods (e.g. IPHASX J184336.6+034640 ($\theta=18$") and IPHASX J194359.5+170901 ($\theta=122$")), as well as small and large size PNe with discordant values (e.g.IPHASX J183911.8+010624 ($\theta=6$") and IPHASX J195657.6+265714 ($\theta=24$")). Thus size may not be an issue.

Is the (dis)agreement on the distances linked to the morphology of the PN ? If we compare the different distances and the morphologies of the PNe from which they are derived, there is no obvious link: none of the morphological types are more likely to provide a better agreement of the distances than another. But if we consider the morphology of the PNe upstream i.e.when the parameters to obtain the distances are determined (namely the surface brightness and the flux), then the shape can play a crucial role, as mentioned earlier. The detailed examination of the geometry of the PN is therefore a key point in obtaining accurate distances. This would lead to a better determination of the surface brightness and the flux as the entire PN would be taken into account.

In the case of the comparison of the SB-R method with the "spectroscopic method", the use of the single Hα flux (in the first one) may have a larger influence than previously thought. We considered the Hα+[NII] flux for all the SB-R methods based on imaging. The total flux of the PN would be enhanced due to the contribution of the nitrogen, and lead to the discrepancy concerning the distance (for the same PN surface). On the other hand, the derivation of the extinction for the PNe may also suffer some errors.

We also have to emphasise that the SB-R method relies on previously determined

distances, and we assumed that those distances are correct within an estimated error. This assumption may not be necessarily true. So, in order to check it, we derived the distances of a set of known PNe in the same sky area as our IPHAS targets. We used, the spectroscopic method based on their "pure" Hα flux given in the Acker et al. (1992) catalogue and the general SB relation. This was compared to other estimations of the distances by Cahn et al. (1992) and Zhang (1995). The results for the 78 PNe (with the necessary available data) are listed in Table 6.9. We found quite a good agreement for most of the PNe between the 3 methods i.e. optical surface brightness-radius by Frew and Parker (2006), "Shklovskii" method by Cahn et al. (1992) and using the mean of the results given by the radio SB-R and ionised mass-radius relations by Zhang (1995). Unfortunately we do not have at this stage the IPHAS extinction curves for those PNe.

Table 6.9: Comparison of the distances (kpc) of known PNe using the SB-R method (the general fitting law, Log SB(Hα) = -3.61 log R - 5.37, is used), the results from Cahn et al. (1992) and Zhang (1995)

PNG	SB-R	Cahn et al. (1992)	Zhang (1995)
032.0-03.0	8.7±3.4	9.1	12.6
032.5-03.2	14.3±5.7	-	-
032.7-02.0	3.4±1.3	3.4	5.0
032.9-02.8	11.1±4.4	5.1	8.9
033.0-05.3	1.6±0.6	2.4	3.9
033.8-02.6	3.1±1.2	2.0	2.3
034.0+02.2	6.4±2.5	5.0	5.7
035.7-05.0	7.5±3.0	-	-
035.9-01.1	7.5±0.3	0.9	1.9
038.4-03.3	18.1±7.2	-	-

Table 6.9 – continued .

PNG	SB-R	Cahn et al. (1992)	Zhang (1995)
038.7-03.3	11.1±4.4	-	-
039.5-02.7	4.4±1.7	4.7	4.5
040.4-03.1	7.8±3.1	6.2	6.8
041.2-00.6	12.0±4.8	-	-
041.8+04.4	15.8±6.3	-	-
041.8-02.9	0.8±0.3	0.6	0.9
043.0-03.0	5.6±2.2	6.6	8.4
043.1+03.8	6.2±2.4	6.5	6.5
045.4-02.7	1.4±0.5	2.1	7.9
045.7-04.5	2.0±0.8	1.7	1.8
045.9-01.9	15.5±6.2	6.1	10.2
046.3-03.1	3.3±1.3	4.6	4.3
046.4-04.1	4.6±1.8	2.9	3.2
047.1+04.1	12.2±4.9	-	-
048.0-02.3	3.3±1.3	4.6	4.0
048.1+01.1	9.7±3.8	2.8	6.4
048.5+04.2	11.4±4.5	15.1	14.9
048.7+01.9	5.2±2.0	3.3	4.3
049.4+02.4	10.2±4.0	-	8.5
050.1+03.3	0.3±0.1	0.6	1.1
051.0+02.8	5.2±2.1	-	-
051.0+03.0	4.2±1.6	3.9	6.6
051.0-04.5	5.2±2.1	-	-
051.9-03.8	5.1±2.0	4.6	4.6
052.2-04.0	5.0±2.0	4.1	8.6
052.5-02.9	5.7±2.3	4.6	4.8

Table 6.9 – continued .

PNG	SB-R	Cahn et al. (1992)	Zhang (1995)
052.9+02.7	12.7±5.0	3.9	6.9
052.9-02.7	59.8±23.9	20.4	29.3
053.8-03.0	3.5±1.4	-	-
054.4-02.5	2.5±1.0	4.2	9.8
055.1-01.8	19.5±7.8	-	-
055.2+02.8	3.6±1.4	4.6	6.6
055.3+02.7	6.6±2.6	-	-
055.5-00.5	4.5±1.8	-	-
055.6+02.1	5.7±2.2	-	-
056.0+02.0	15.7±6.3	3.9	5.7
057.9-01.5	5.2±2.0	2.8	6.3
058.9+01.3	6.9±2.7	7.0	6.8
059.0+04.6	11.6±4.6	-	-
059.0-01.7	6.0±2.4	-	-
059.4+02.3	9.4±3.7	7.1	8.2
059.9+02.0	10.9±4.3	7.6	12.2
060.5+01.8	5.3±2.1	3.9	6.0
060.5-00.3	17.5±7.0	-	-
061.3+03.6	5.6±2.2	-	-
062.4-00.2	5.3±2.1	6.9	7.4
064.9-02.1	3.9±1.5	2.8	8.2
065.9+00.5	2.3±0.9	1.3	1.4
067.9-00.2	27.6±11.0	2.4	8.4
068.3-02.7	3.3±1.3	3.3	6.0
068.6+01.1	1.9±0.7	-	-
068.7+01.9	9.6±3.8	7.9	8.2

Table 6.9 – continued .

PNG	SB-R	Cahn et al. (1992)	Zhang (1995)
068.7+03.0	6.1±2.4	6.6	7.9
068.8-00.0	5.7±2.2	3.8	4.5
069.2+02.8	6.6±2.6	-	22.4
069.2+03.8	5.9±2.3	-	-
069.4-02.6	1.4±0.5	1.6	2.3
069.6-03.9	8.6±3.4	5.6	-
071.6-02.3	3.7±1.4	1.7	4.4
072.1+00.1	5.0±2.0	4.0	4.0
073.0-02.4	6.8±2.7	-	-
074.5+02.1	5.2±2.0	2.4	3.9
075.6+04.3	7.3±2.9	-	-
076.4+01.8	12.7±5.1	-	-
077.5+03.7	6.7±2.7	-	-
077.7+03.1	15.0±6.0	-	-
078.3-02.7	4.4±1.7	-	-
078.9+00.7	15.9±6.3	-	-

We have pointed out the pros and cons in using different methods to derive the distances to PNe. A "pure" Hα flux and an accurate determination of the PN surface are needed for the SB-R method. The reason for the differences with the distances from the IPHAS extinction curves (although sometime compensated by the error margin) is not entirely clear at this stage and may come from the accuracy, or lack of it, concerning the determination of the nebular extinction.

6.5.2 IPHAS PNe in the Galactic Plane: height and galactocentric distances

We show, in Fig.6.7 (top), the distances of the confirmed IPHAS PNe listed in Table 6.6 using the IPHAS extinction curves and the ones of known planetary nebulae in the same sky area. The latter distances have mainly been obtained by Cahn et al. (1992) and Zhang (1995). We also show the expected number of nebulae in terms of distance from the Sun and it appears that the detection of PNe is quite complete (with a peak at ~4.5 kpc, the missing objects may be hidden in the interstellar medium).

Still in Fig.6.7 (bottom), the absolute height above the Galactic Plane (|z| in pc) for the IPHAS data has been plotted against the distance. First we notice that 2 objects lie at a high distance above the plane i.e.with |z| greater than 200 pc. In this group we find 1 bipolar PN (IPHASX J191124.8+002743 [349 pc] and 1 round PN (IPHASX J194751.9+311818 [296 pc]) (see also Table 6.6). The mean absolute height for these two groups gives: $< |z| >=88$ pc for the bipolar $(< |z| >=55$ pc if we removed the highest PN) and $< |z| >=129$ pc for the round PNe $(< |z| >=96$ pc if we removed the highest one). In this small sample, the separation between the bipolar and round PNe in the plane is not as significant as found by Corradi and Schwarz (1995) and Manchado et al. (2000), moreover we do find these two groups at a lower mean height than found by the previous authors (see Table 1.2).

In figure 6.8 we show the distribution of z (distance from the plane) for the bipolar and round PNe. Although the sample is very small, we attempted to fit the histograms with the exponential characteristic of the scale height:

$$n(z) = n(0)e^{\frac{-z}{<|z|>}} \tag{6.7}$$

Assuming that all the objects are taken into account, the exponential relative to the scale height fits well the distribution for both groups (with a mean height of 88 pc for the bipolar and 129 pc for the round PNe).
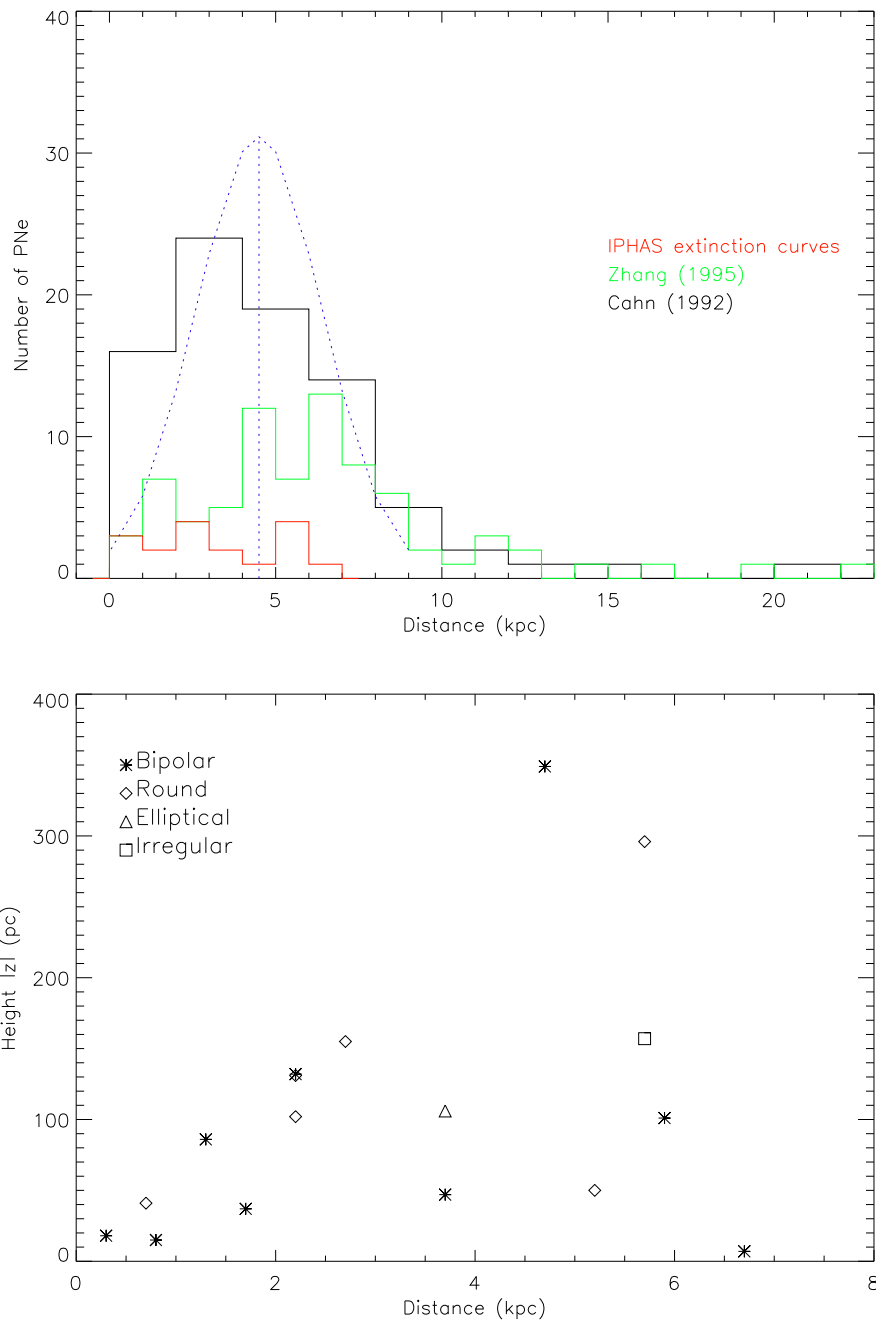
Figure 6.7: Distribution of the distances and height above the plane of the IPHAS planetary nebulae. Top: The IPHAS PNe distances (red) are compared to the distances retrieved by Cahn et al. (1992) (black) and Zhang (1995) (green). The blue dotted line shows the expected number of nebulae in term of distance from the Sun.
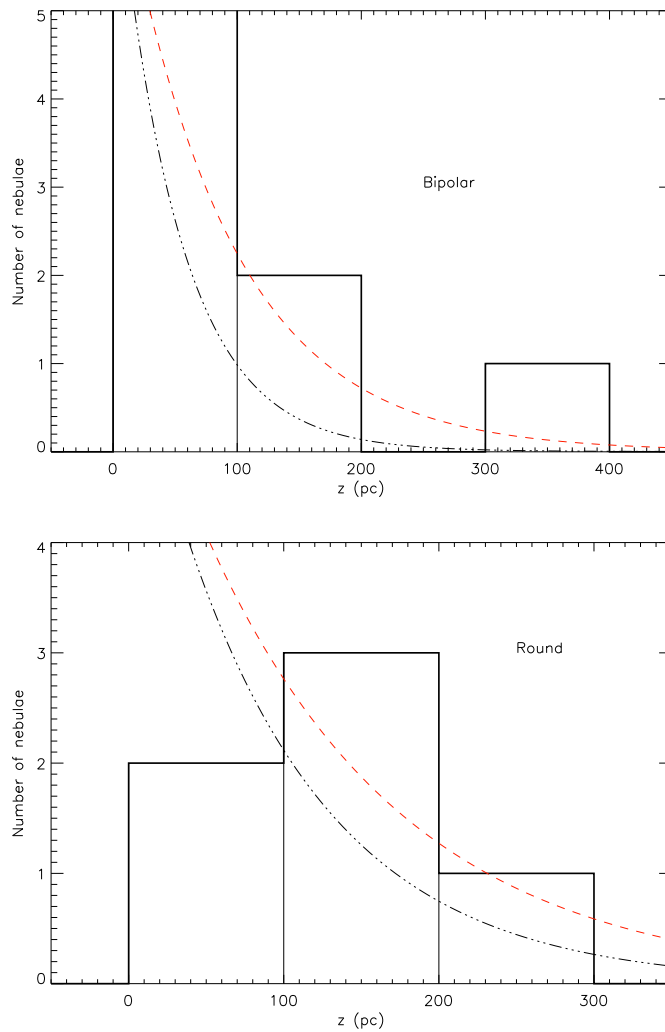
Figure 6.8: z distribution for bipolar and round PNe. The dashed lines show the fits with the scale heights as defined above. The red line indicates that all the objects have been taken into account, the black line represents all the objects but the highest z.

Once we have an estimation of the distance of the IPHAS PNe from the Sun, it is interesting to locate them using the galactic centre as origin. This would allow us to determine how far they are seen and in general how far IPHAS can detect planetary nebulae in this particular direction (29 deg $< l <$ 79 deg and b=±5 deg). Figure 6.9 shows the distribution of the IPHAS PNe according to their galactocentric distances
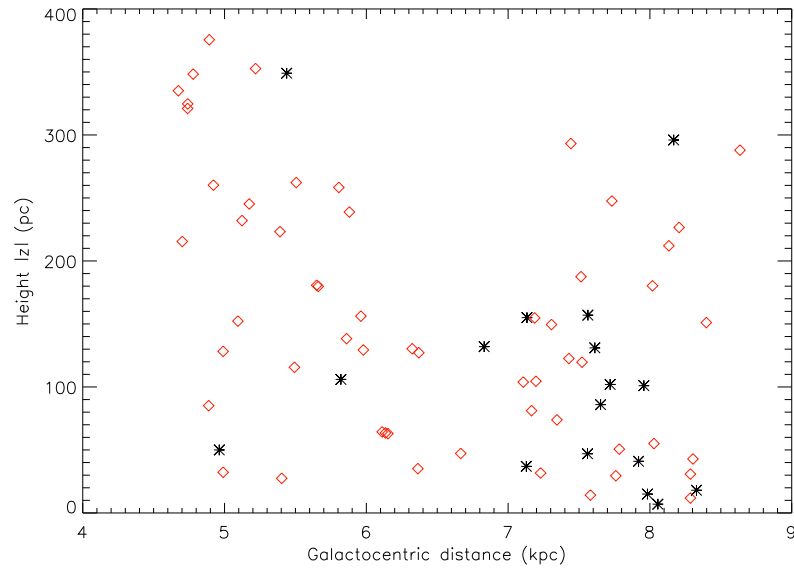
Figure 6.9: Galactic location of the IPHAS PNe (black) and a set of known PNe from Acker et al. (1992) (red).

(Table 6.10). In this context the distances from the extinction curves have been used. We also show, for comparative purposes, the galactocentric distances for PNe chosen in the Strasbourg-ESO catalogue (Acker et al. 1992). The distances of those objects have been retrieved by Cahn et al. (1992). We assume that the distance to the galactic centre is 8.5 kpc.

The sample of PNe presented here is mainly located near the Sun (between roughly 7kpc and 8.4 kpc in galactocentric distances), although we found some of them at larger distances. For the closest PNe we do not expect to see great changes in their abundance unless we consider that IPHAS discovers faint and old PNe. Concerning the PNe with the largest distances, their discovery is quite encouraging: if this trend is similar in other area of the plane and particularly in the galactic anticentre, we should be able to define the characteristics of far located nebulae, such as the existence of an abundance gradient (Mampaso et al. 2007).

Table 6.10: Galactocentric distances in kpc of the IPHAS PNe.

PN (IPHASX J)	D_{Gal}
183911.8+010624	7.9
184336.6+034640	6.8
185224.2-004446	4.9
185525.7-004823	7.1
185925.8+001734	5.8
191124.8+002743	5.4
191345.6+174752	7.1
191445.1+133219	7.9
192847.1+093439	7.6
192902.5+244646	7.6
193827.9+265752	7.7
193912.0+251105	7.5
194359.5+170901	8.3
194751.9+311818	8.1
194940.9+261521	8.0
195248.8+255359	7.5
195657.6+265714	7.9

6.6   Ionised Mass

Our knowledge of the distances is fundamental in order to derive other physical pa-
rameters like the nebular mass or ionised mass (M_i) of the nebulae. The lack of data
on the stellar temperature for the IPHAS PNe prevents any association to evolutionary
tracks that we need in order to estimate the core mass of the targets. But we can still
estimate the nebular mass or ionised mass M_i. There are two ways to characterise the
mass of a planetary nebula. First, if we assume that the ionised mass corresponds to

the total mass ejected by the PN, the PN is then considered as density bounded. M_i is therefore constant. Then, if we assume that the total mass of the nebula is much higher than the ionised mass, the PN is classified as ionisation bounded. The zone where the matter is ionised is limited to the deep area where Lyman photons are operating. In this case M_i will increase with the radius.

The mass can be obtained from the equation

$$M_i = \frac{4\pi}{3} \times n_e \times \mu_e \times m_H \times \epsilon \times R_i^3 \tag{6.8}$$

with μ_e the mean atomic weight per electron and ϵ the filling factor that we chose to be 0.6 .

Figure 6.10 shows the correlation between M_i and the radius for a sample of PNe from Zhang (1995) and the IPHAS objects (which results are listed in Table6.11). Two PNe have a (really) large mass which is unrealistic, the error probably comes from the distance determination which is a lower limit. Otherwise most of the IPHAS nebulae have their masses between 10^{-4}M$_\odot$ and 1 M$_\odot$, which is the range usually observed for PNe.
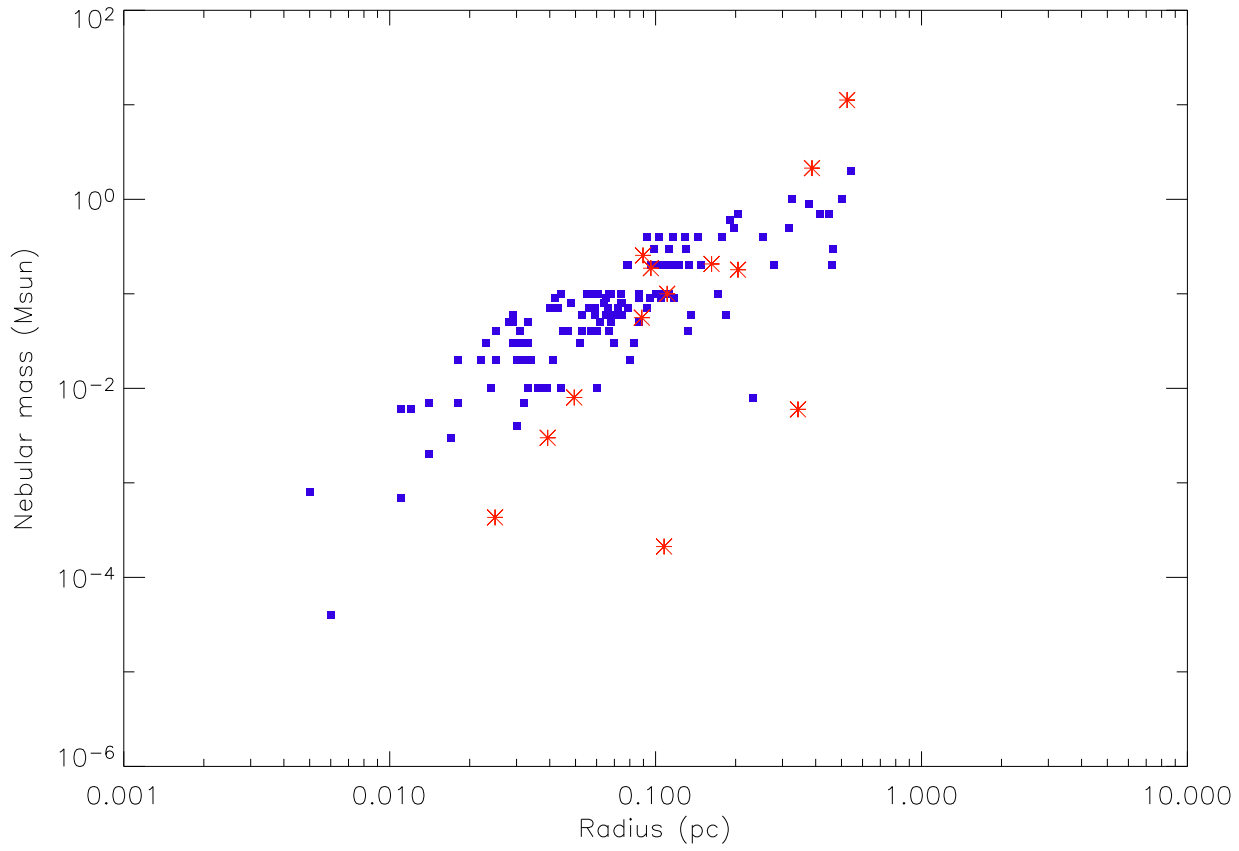
Figure 6.10: Nebular mass against radius for a set of PNe from Zhang (1995) (blue) and the IPHAS objects (red) which distances have been determined with the extinction curves.

Table 6.11: Derived ionised masses for the IPHAS targets.

Name (IPHASX J)	M_i ($M_\odot$)
184336.6+034640	0.187
185525.7-004823	0.008
185925.8+001734	2.12e-4
191124.8+002743	2.14
191345.6+174752	0.003
191445.1+133219	4.31e-4
192847.1+093439	0.18
193912.0+251105	11.23
194359.5+170901	0.056
194751.9+311818	0.100
194940.9+261521	0.207
195248.8+255359	0.255
195657.6+265714	0.006

The issue of the density/ionisation bounded nature of the IPHAS PNe will be addressed in the next chapter.

7

Recombination process and age determination

7.1 Application to the sample of IPHAS PNe

As IPHAS targets rather faint PNe, many of them are likely to be evolved and subject to recombination. The recombination process in planetary nebulae occurs when they enter the cooling track of the HR diagram, which corresponds to a rapid decrease of the UV radiation of the CS. A sign of this phenomenon may be seen through the [NII] overintensity relative to Hα, observed in some PNe (Table7.1). But the high [NII] flux can also be due to the presence of shocks.

The recombination rate is density dependent. It will be lower in a high density PN (young) compared to a low density one. The recombination time scale is then shorter for young PNe and longer for more evolved PNe. This is an important parameter as in the case of evolved and massive (M > 1 M$_\odot$) PNe (Tylenda 1983), the recombination time of the nebular gas is comparable to the nebular age. We note that in the case of the bipolar PNe, the recombination time scale is shorter than for less massive PNe (round, elliptical).

An estimation of this time scale is given by Kwok (2000). It assumes an electronic

Table 7.1: List of IPHAS PNe showing a nitrogen enhancement.

Name	[NII]6584/Hα
IPHASX J185224.2-004446	1.88
IPHASX J185525.7-004823	1.72
IPHASX J185925.8+001734	1.53
IPHASX J191124.8+002743	1.17
IPHASX J191445.1+133219	1.99
IPHASX J192847.1+093439	4.11
IPHASX J194940.9+261521	1.40
IPHASX J195248.8+255359	2.44
IPHASX J195657.6+265714	4.07

temperature of 10^4 K and an hydrogen recombination coefficient α_H of 4.18×10^{-13} cm^3 s^{-1}.

$$t_r = \frac{1}{n_e \alpha_H} \sim \frac{7.6 \times 10^4}{n_e/cm^{-3}} yr \qquad (7.1)$$

The derivation of the recombination time scale is a tool that will indicate the evolutionary age of the PNe. Using the values of the [SII]6717/6731 ratio listed in Table 3.4, the density is measured using the "Nebular" package in IRAF developed by Shaw and Dufour (1995). To be consistent, we used the same temperature that we assumed for the recombination time estimation. There is a limit to the use of the [SII] ratio as a density indicator as it is no longer sensitive for densities lower than $\sim$100 cm^{-3} because collisional excitation becomes too infrequent. In the same way there is an upper limit, $\sim$ 3$\times$10^5 cm^{-3}, when collisional de-excitation becomes important

In Table 7.2, we list the recombination time scale for our nebulae. Except for IPHASX J185925.8+001734 and IPHASX J195657.6+265714, all the PNe have a short time-scale, meaning that they are probably not recombining yet and that ionisation is still predominant. Assuming that a typical PN will enter the cooling track at

Table 7.2: Recombination time scale in a set of IPHAS planetary nebulae.

Name	n_e[SII](cm^{-3})	t_r (yr)
IPHASX J184336.6+034640	2486	30
IPHASX J185525.7-004823	1217	62
IPHASX J185925.8+001734	2 [1]	3.8×10^4
IPHASX J191124.8+002743	432	175
IPHASX J191345.6+174752	606	125
IPHASX J191445.1+133219	328	232
IPHASX J192847.1+093439	260	292
IPHASX J193912.0+251105	910	83
IPHASX J194359.5+170901	948	80
IPHASX J194751.9+311818	874	87
IPHASX J194940.9+261521	558	136
IPHASX J195248.8+255359	4160	18
IPHASX J195657.6+265714	2 [1]	3.8×10^4

[1] The [SII] line ratio is above the 1.43 sensitivity limit, for the derivation of the density. The lowest density applicable is therefore 2 cm^{-3}.

an age between ~10 000 and ~20 000 yrs, the observed IPHAS PNe could be rather young (i.e. a young central star) with values lower than 10^4 yrs. The two exceptions are more compatible with evolved PNe.

Another way to quantify the age of these IPHAS PNe consists of studying their density/size relationship and comparing this with well studied planetary nebulae. As said previously, a young PN is more likely to be smaller than an evolved PN whose envelope starts to expand in the ISM, in the same way a young PN will generally have a higher density than an old one. The determination of the size is distance dependent and the error on the radius generally results from the lack of accuracy on the distance. Figure 7.1 shows a $1/n_e^2$ distribution and 3 objects are found with a comparative dynamical age equal to or longer than 10 000 yrs (IPHASX J185925.8+001734,

IPHASX J191124.8+002743, and IPHASX J195657.6+265714): those PNe are therefore recombining. We also notice that IPHASX J192847.1+093439 and IPHASX J195657.6+265714 show the largest nitrogen overabundance with ratios (over Hα) of 4.11 and 4.07 respectively (Table 7.1).

Table 7.3 gives a summary of the nebular parameters used in Fig.7.1 and also shows in the fourth column for the IPHAS PNe, a calculation of the dynamical age (or observed age), assuming a typical expansion velocity of 25 km/s. The velocity expansion of PNe is generally considered as constant with a mean velocity of 20 km/s (24 km/s for Kaler et al. (1990), 26 km/s for Phillips (1989)). This speed slowed down when the nebulae hit the ISM i.e. in the final part of their evolution. In our case 4 PNe show an age greater than 10 000 yrs: IPHASX J191124.8+002743, IPHASX J193827.8+265752, IPHASX J193912.0+251105 and IPHASX J195657.6+265714. These results validate partially those obtained from figure 7.1. All the other PNe are still rather young. This method relies on the accuracy concerning the distance. The findings from the 3 methods (Recombination time scale, density versus size relation and R/V$_{exp}$) are listed in Table 7.4. IPHASX J195657.6+265714 (Figure 7.2) is the only PN for which all methods agree on its recombination status and therefore its description as an evolved PN. If we compare the evolutionary age of the central star based on the recombination time and the dynamical age, we can see that there is a strong discrepancy. The error could either come from the wrong determination of the measurable parameters like the distances and nebular sizes, or from the fact that the two time-scales are not comparable as their zero-point is not the same. Indeed, the evolutionary time starts when the temperature is high enough to ionise the nebula while the dynamical time starts at the first ejection of matter which creates the nebula. Moreover as the evolutionary time inversely depends on the core mass, the time-scale will decrease for a high core mass as in bipolar PNe.

The survey covers PNe with a wide range of ages. But is there a particular group which is more likely to be revealed by IPHAS?
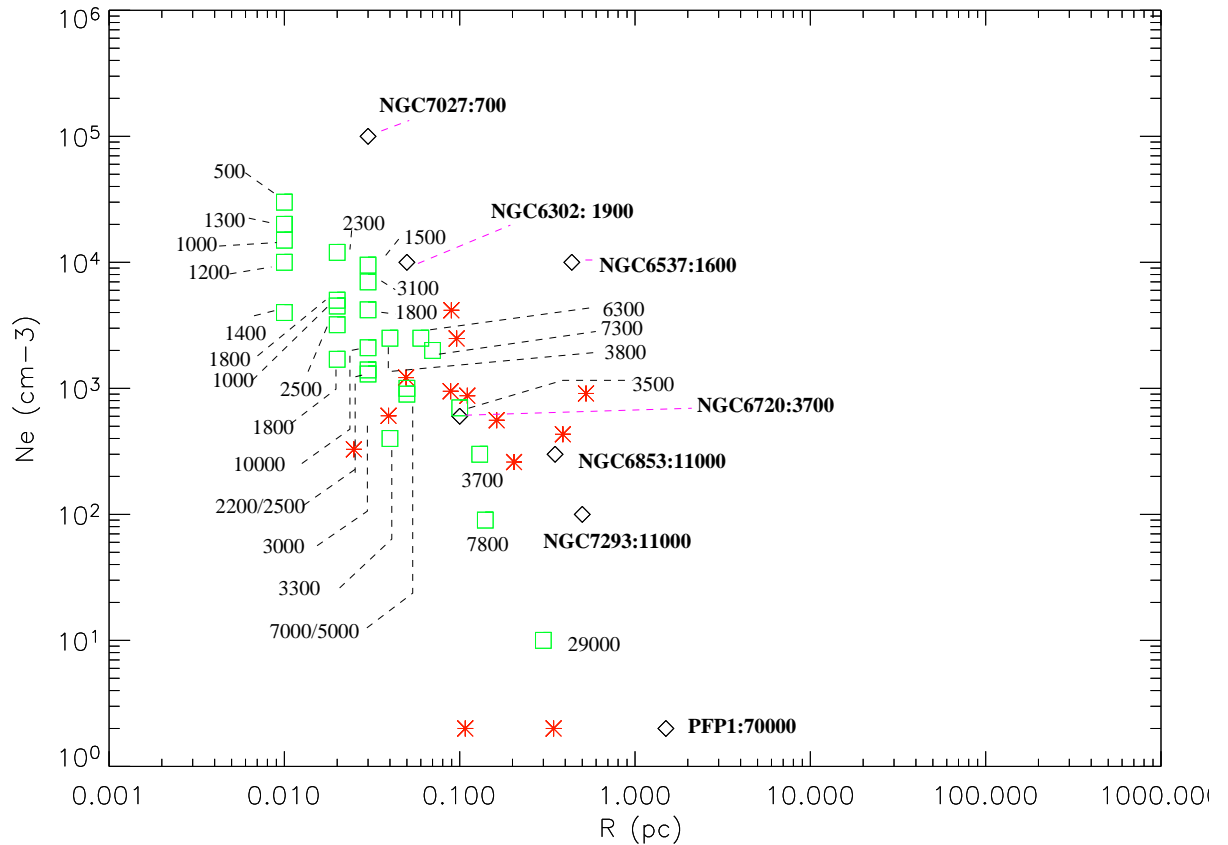
Figure 7.1: Electron Density versus radius diagram for the IPHAS PNe (Red Asterisk) compared to a set of well studied planetary nebulae (Black Diamond) chosen as milestones and several other known PNe taken from the literature (Green Square). The numbers represent the dynamical ages of the nebulae.

Figure7.3 shows that most of the PNe discovered by the survey have a radius greater than ~0.03 pc and a density lower than 10^4 cm^{-3}. This corresponds to PNe with an age (dynamical) greater than ~4000 yrs. In our small sample, all but 4 objects have an age between 4000 and 8000 yrs. We do not have any new young PNe. If we look at this distribution using this time a set of known PNe from Acker et al. (1992) in the same sky area as the IPHAS PNe, Fig.7.4, we see first that the majority of those known PN are located in the range 4000-8000 years, and so are 8 of the IPHAS PNe. Also, four
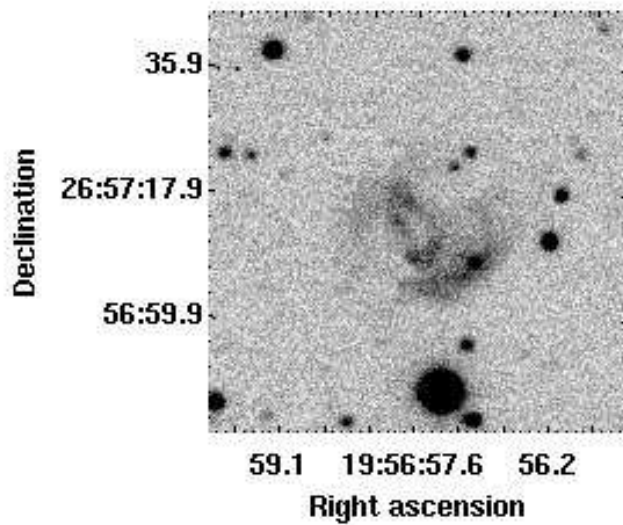
Figure 7.2: IPHASX J195657.6+265714: an evolved recombining PN.

IPHAS planetary nebulae fall in the recombination area, which is 1 more than previously selected.

Therefore we can say that with the survey we are likely to discover "middle-aged" PNe, like the typical NGC 6720. As most of the PNe already discovered in this sky area occupy the same place in the radius vs density diagram, we can conclude that (most of) the new IPHAS PNe may not have been detected before, due to the extinction and not due to their great age. Nevertheless, we do observe (very) evolved IPHAS PNe, like the typical NGC 7293; and no known PNe (in same sky area) have been identified in this part of the radius vs density diagram. For those IPHAS PNe, the reason for their previous non-detection is likely to be linked to their greater evolutionary status.

IPHAS is therefore a good tool to complete previous surveys in terms of coverage of evolutionary stages.
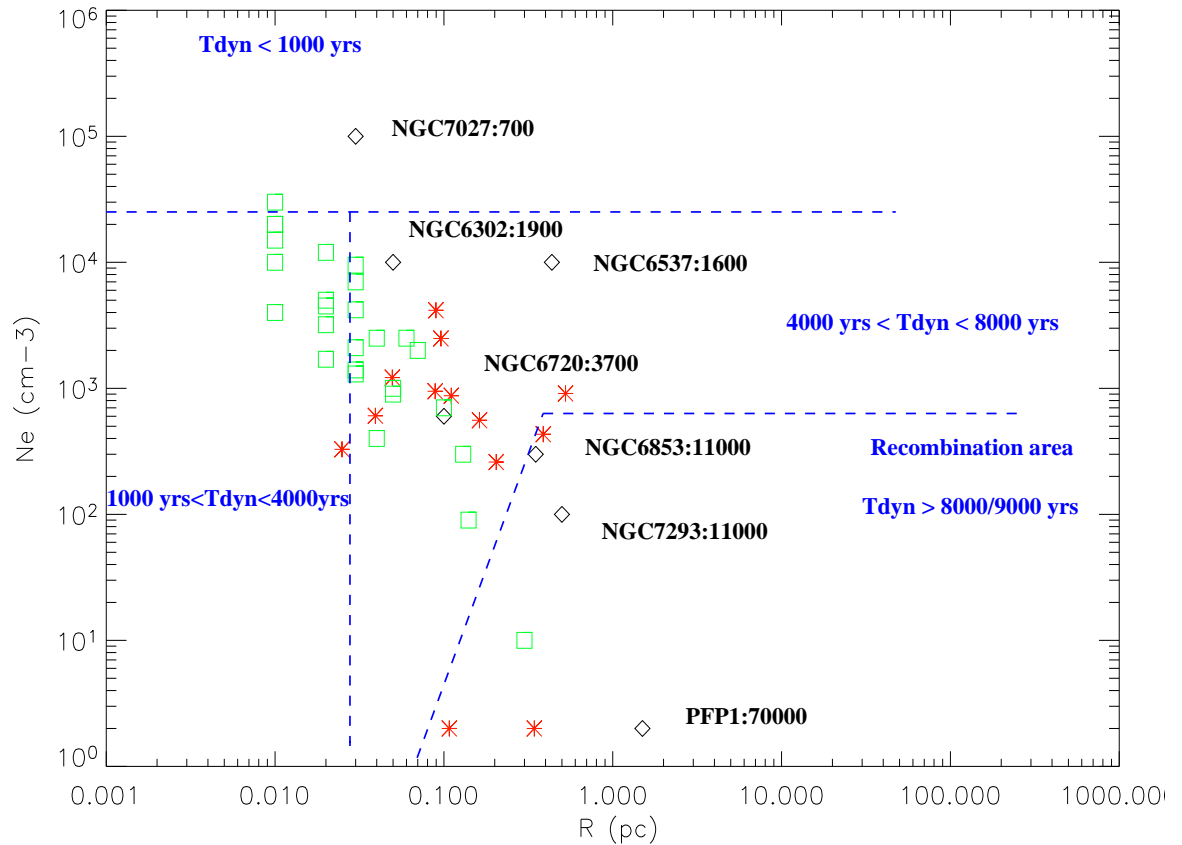
Figure 7.3: Age determination from the electronic density versus radius diagram for the IPHAS PNe. Comparison with a set a well known PNe.

7.2 Discussion

7.2.1 The age populations

Our study of the recombination process and age of the IPHAS PNe have shown the emergence of two groups :

- The "middle-aged" PNe (4000-8000 yrs), which show no sign of recombination and represent the majority of the sample. They do not seem to differ, in term of age, from the known PNe in the same sky area. They were just hidden by interstellar extinction, which explains their previous non-discovery.
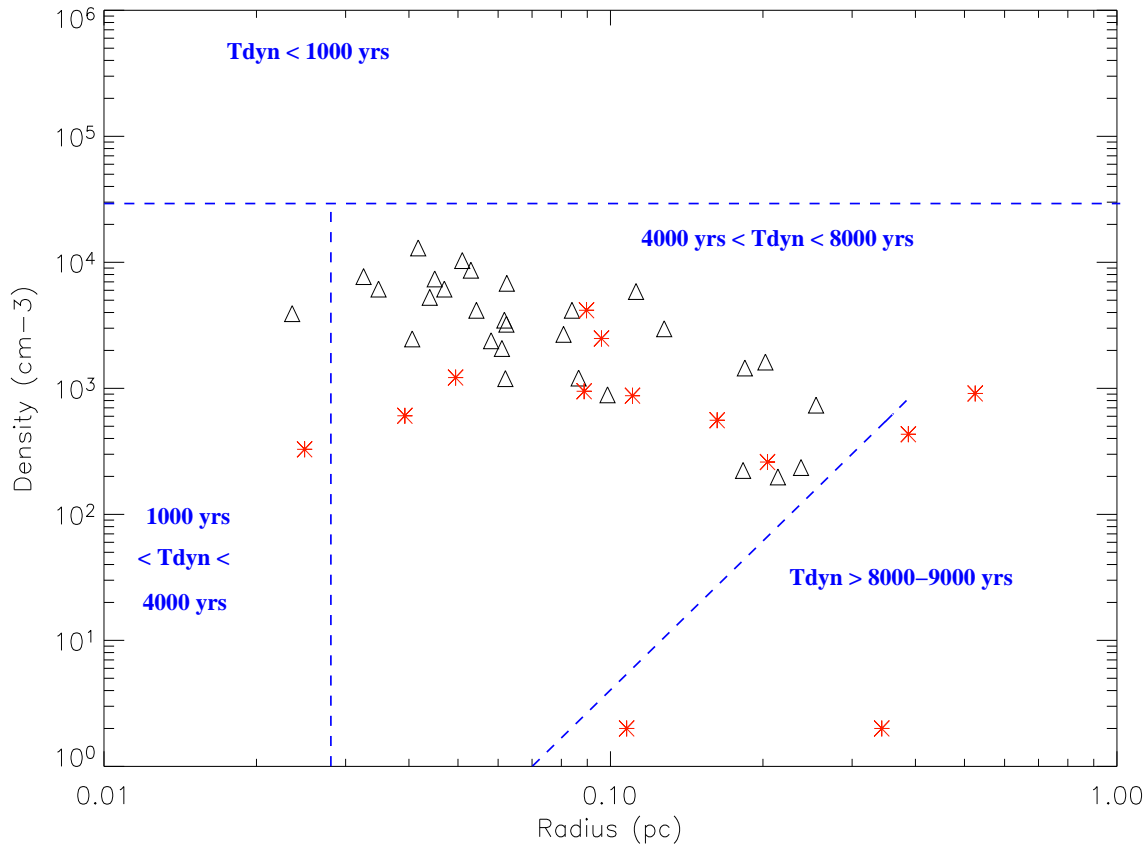
Figure 7.4: Density versus radius diagram for the IPHAS PNe and comparison with a sample of known PNe located in the same sky area. The radii have been derived from the SB-R relation used in Table 6.9 and the densities have been obtained from the [SII] lines given in the Acker et al. (1992) catalogue. Red: IPHAS PNe and Black: known PNe. We have to emphasise that the use of canonical values for the radii, using the SB-R method, may introduce errors for recombining and evolved PNe due to their complex morphology.

- The "evolved" PNe, with an age greater than ~8000 yrs. All show diverse signs of recombination, and only one PN has been fully identified as a recombining object (See Table 7.4).

One aim of the survey, which goes deeper in terms of sensitivity than previous surveys, explains why we are picking up those two types of generally faint objects. The low number of PNe observed on the cooling track is more a statistical problem than an astrophysical one. Hence, we are dealing with a small number of objects, and the figure is very likely to change once we complete the follow up spectroscopy for all the IPHAS nebulae. Nevertheless the radio study (Section 3.3) has shown that the IPHAS sources are generally evolved and extended, and in this case extinction does not play any role. We may therefore expect more IPHAS PNe on the cooling track.

Table 7.3: Nebular parameters for a set of the "milestone" PNe and dynamical age determination for the IPHAS PNe (the distances from the extinction curves are used).

Name	$n_e(cm^{-3})$	Radius (pc)	Age_{dyn} (yrs)[1]
NGC 7027	$10^{5\,a1}$	0.030^{a2}	700^{a3}
NGC 6537	$10^{4\,b1}$	0.436^{b2}	1600^{b3}
NGC 6302	$10^{4\,c1}$	0.05^{c2}	1900^{c3}
NGC 7293	100^{d1}	0.5^{d2}	11000^{d3}
NGC 6853	300^{e1}	0.35^{e2}	11000^{e3}
NGC 6720	600^{f1}	0.10^{f2}	3400^{f3}
PFP1^g	2	1.5	70000
IPHASX J183911.8+010624	-	0.01	390
IPHASX J184336.6+034640	2486	0.09	3700
IPHASX J185224.2-004446	-	0.05	1960*
IPHASX J185525.7-004823	1217	0.05	1960
IPHASX J185925.8+001734	2	0.10	4200*
IPHASX J191124.8+002743	432	0.38	14800
IPHASX J191345.6+174752	606	0.04	1500
IPHASX J191445.1+133219	328	0.02	980
IPHASX J192847.1+093439	260	0.20	7986
IPHASX J192902.5+244646	-	0.05	1960
IPHASX J193827.9+265752	-	0.52	20300
IPHASX J193912.0+251105	910	0.52	20300*
IPHASX J194359.5+170901	948	0.09	3500
IPHASX J194751.9+311818	874	0.11	4300*
IPHASX J194940.9+261521	558	0.16	6400*
IPHASX J195248.8+255359	4160	0.09	3500*
IPHASX J195657.6+265714	2	0.34	13000*

[1] For the IPHAS targets we assume an expansion velocity of 25 km/s. *: Lower limit on the distance, a1:Middlemass (1990), a2:Masson (1989) and Acker et al. (1992), a3:Latter et al. (2000), b1:Pottasch et al. (2000), b2:Matsuura et al. (2005a) and Corradi and Schwarz (1993), b3:Matsuura et al. (2005a), c1:Matsuura et al. (2005a), c2:Cahn et al. (1992) and Acker et al. (1992), c3:Meaburn et al. (2005), d1:Leene and Pottasch (1987), d2:Meaburn et al. (2008) and Acker et al. (1992),d3:Meaburn et al. (2008), e1:Barker (1984), e2:Meaburn and Lopez (1993) and Acker et al. (1992), e3:O'Dell et al. (2002), f1:Garnett and Dinerstein (2001), f2:O'Dell et al. (2002), f3:Acker et al. (1992), g: All data from Pierce et al. (2004).

Table 7.4: Cross-correlation of the results obtained about the evolutionary status of the IPHAS PNe and the occurence of recombination. The crosses indicate that recombination is taking place.

Name (IPHASX J)	Recombination time scale	Density vs. Radius	R/V$_{exp}$)
183911.8+010624	-	-	-
184336.6+034640	-	-	-
185224.2-004446	-	-	-
185525.7-004823	-	-	-
185925.8+001734	X	X	-
191124.8+002743	-	X	X
191345.6+174752	-	-	-
191445.1+133219	-	-	-
192847.1+093439	-	X	-
192902.5+244646	-	-	-
193827.9+265752	-	-	X
193912.0+251105	-	-	X[1]
194359.5+170901	-	-	-
194751.9+311818	-	-	-
194940.9+261521	-	-	-
195248.8+255359	-	-	-
195657.6+265714	X	X	X[1]

[1] The radius has been computed using a lower limit on the distance.

7.2.2   Ionization or density bounded ?

As mentioned earlier in section 6.6, an important parameter is whether a PN is optically thick to ionising radiation (ionisation bounded) or not (density bounded). The radius vs density diagram will help to define the boundary between both behaviours as we can provide the location of the Strömgren sphere (Strömgren 1939). Primarily designed for HII regions, this sphere is an ideal model of a perfectly spherical and fully ionised region entirely made of hydrogen. The radius of this sphere (also called Strömgren radius) corresponds to the limit where the recombination rate and ionisation rate are equal. This equilibrium is translated into the equation:

$$\frac{4\pi}{3} \times n^2 \times \beta \times R^3 = Q_* \qquad (7.2)$$

with "n" the hydrogen density, "β" the total recombination rate which is a function of the electron temperature, "R" the radius of the sphere and "Q_*" the rate of ionising photon emission. The n^2 dependence is due to the fact that recombination is a two-body process, hence depends on one n for the proton density and another n for the electron density.

Therefore the Strömgren radius is given by:

$$R = \left(\frac{3}{4\pi} \times \frac{Q_*}{n^2 \beta} \right)^{1/3} \qquad (7.3)$$

We will adopt typical values for planetary nebulae, thus β at $T_e=10^4$ K is equal to 2×10^{-13} cm^3 s^{-1} and $Q_*=10^{47}$ s^{-1}.

Figure 7.5 shows the Strömgren sphere on the radius vs density diagrams of Fig.7.3. We can see that the majority of the PNe (located in a wide sky area) fell under the line delimiting the equilibrium between recombination and ionisation. Those PNe are fully ionised and then density bounded. If we restrict the known PNe to those located in the same sky area as the IPHAS PNe (Fig7.6), the pattern remains the same although we found more PNe being ionisation bounded than previously observed. Concerning the IPHAS PNe, 4 are ionisation bounded and 9 are density bounded. We therefore

observed a systematically higher number of fully ionised nebula. The 4 ionisation bounded IPHAS PNe (Fig.7.7) will have their ionised masses increased with the radius, while the 9 density bounded (Fig.7.8) will have a constant ionised mass. The latter will also become much fainter as they expand.
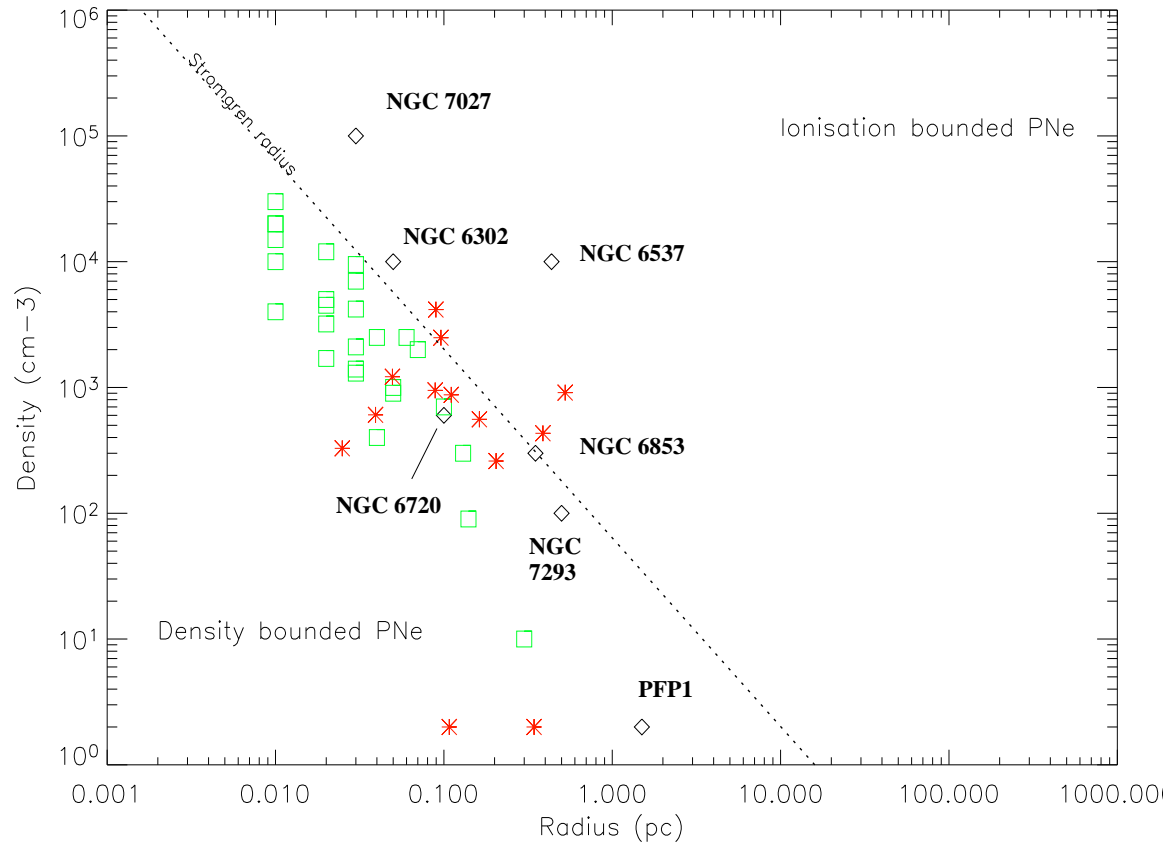
Figure 7.5: Determination of the ionisation and density bounded IPHAS PNe using the Strömgren radius from Fig.7.3.

Figure 7.6: Determination of the ionisation and density bounded IPHAS PNe using the Strömgren radius from Fig.7.4.
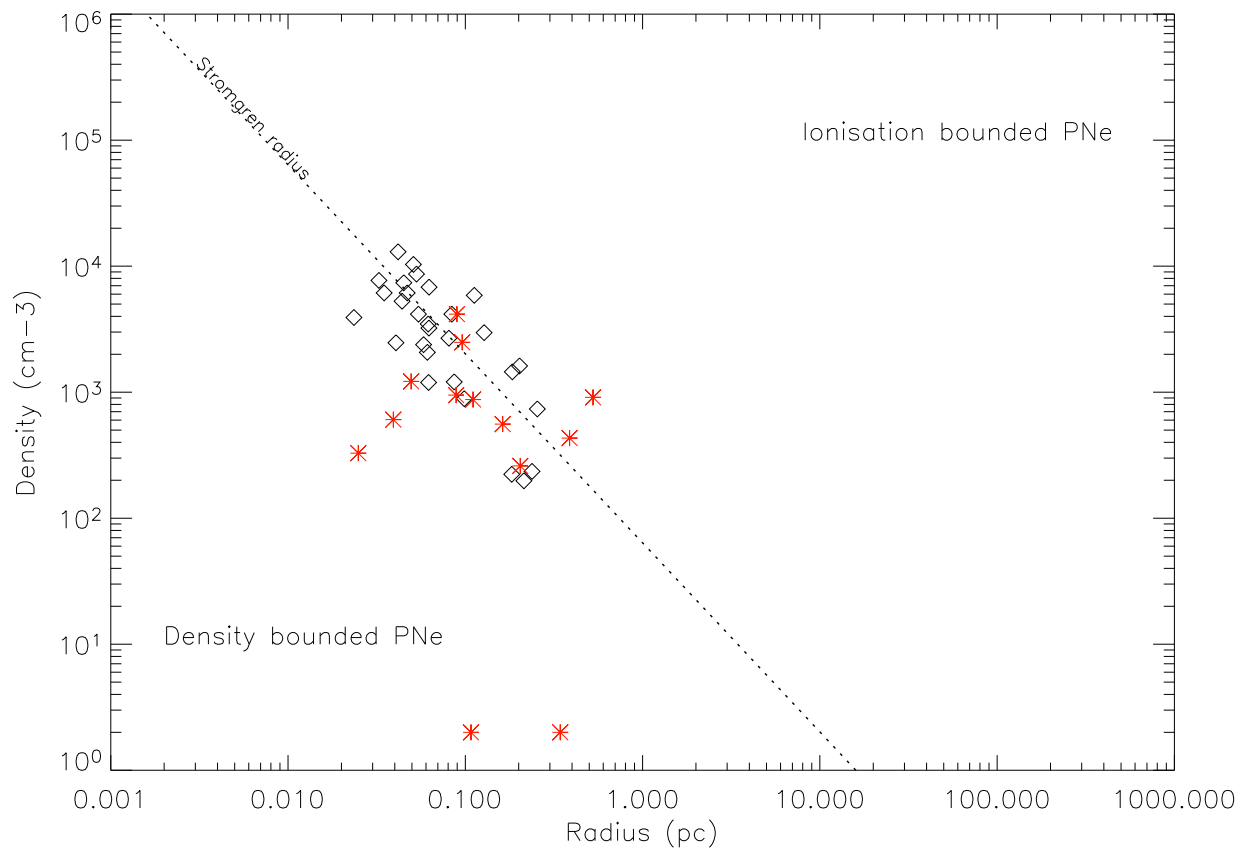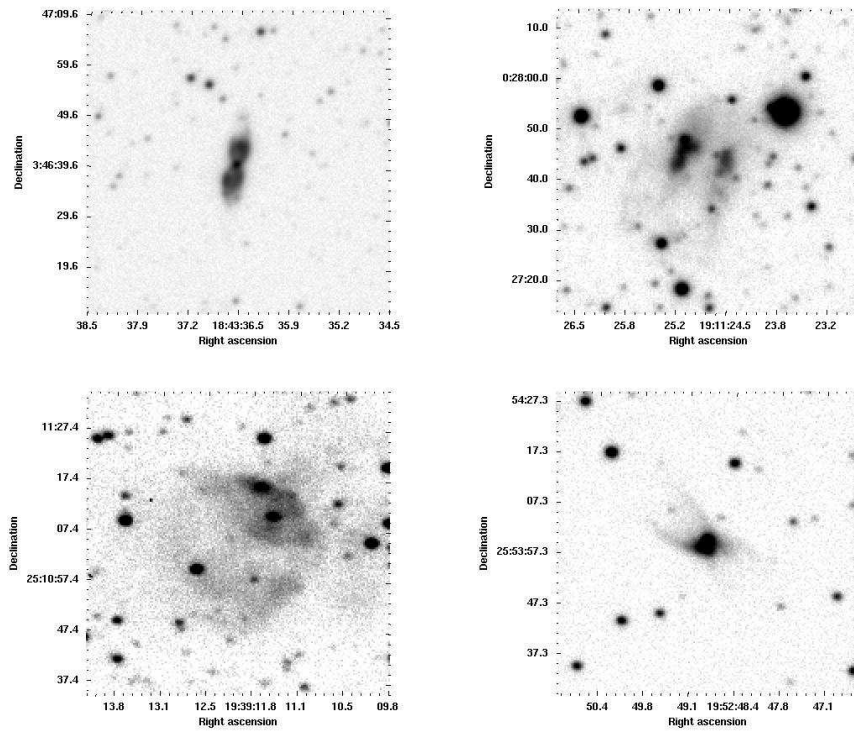
Figure 7.7: Ionisation bounded IPHAS PNe. From left to right and Top to Bottom: IPHASX J184336.6+034640, IPHASX J191124.8+002743 (sign of recombination), IPHASX J193912.0+251105(sign of recombination) and IPHASX J195248.8+255359.
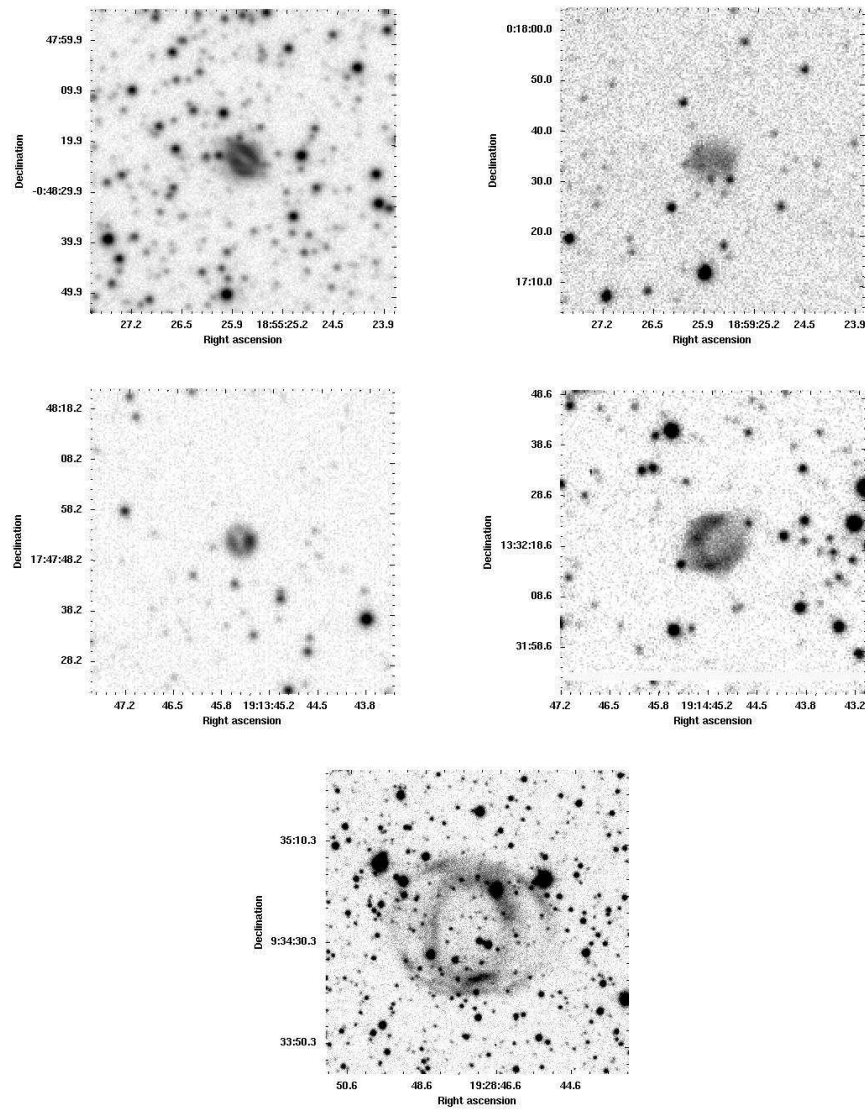
Figure 7.8: Density bounded IPHAS PNe. From left to right and Top to Bottom: IPHASX J185525.7-004823, IPHASX J185925.8+001734, IPHASX J191345.6+174752, IPHASX J191445.1+133219, IPHASX J192847.1+093439.
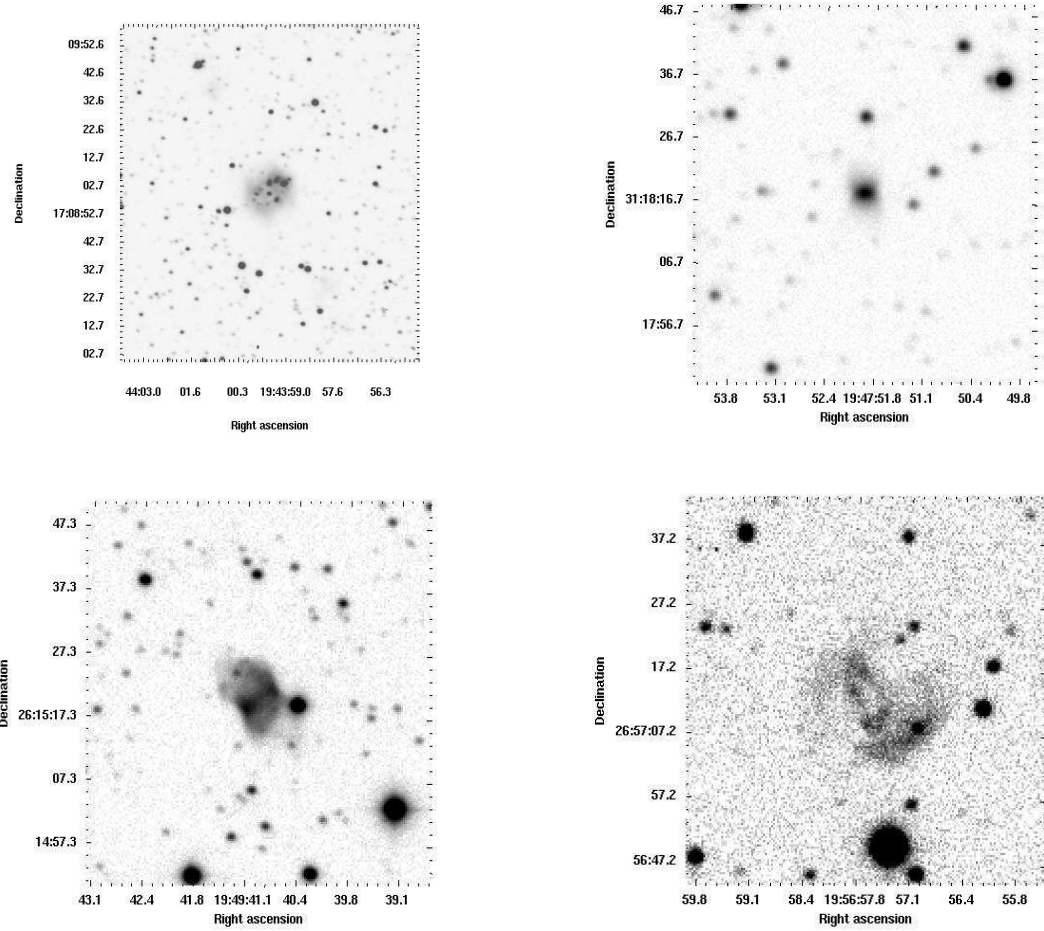
Figure 7.8 (Continued). From left to right and Top to Bottom: IPHASX J194359.5+170901, IPHASX J194751.9+311818, IPHASX J194940.9+261521 and IPHASX J195657.6+265714.

8

Interaction with the interstellar medium

8.1 Classification of the IPHAS nebulae

The PN-ISM interaction is a fundamental process in the development of PNe and has been studied by Borkowski et al. (1990), Soker et al. (1991), Tweedy and Kwitter (1996) and Villaver et al. (2000) among others, from a theoretical and observational point of view. The interaction process does not only refer to large and old nebulae, i.e. it does not "start" at the end of the PN phase. Rauch et al. (2000) and Wareing et al. (2007) showed that different stages of interaction are exhibited during the PNe life (see Fig. 8.1). Rauch et al. (2000) defined 3 epochs: first when the PN is **young** and expanding into the ISM with its density higher than the ISM density. The latter has not much "power" over the PN. Then, during its **mid-age**, the PN density starts to decline but there is still an equilibrium between both entities (relative to their densities). A compression of the external shell of the PN increases its surface brightness. Rauch et al. (2000) also discuss the increase of the recombination rate in the PN. Finally, the expansion and density of the **old** PN decline sufficiently enough that the PN density can be overcome by the ISM density. The PN undergoes all kinds of deformations

(Rayleigh-Taylor instabilities for example, movement of the central star (CS) out of its boundaries...etc). RT instabilities are perturbations occurring at the interface of two layers of different densities, in our case the PN and the ISM. The material of lower density is accelerated into the one of higher density, and hydrodynamic instabilities grow at the interface causing vortices. As the perturbation evolves downward-moving irregularities appear and are generally called "Rayleigh-Taylor fingers". In this context Kelvin-Helmholtz instability can occur,in the form of waves, if the velocity difference across the interface is large enough.

The velocity (between PN and ISM), the density (PN and ISM) and the morphology (PN) are therefore the parameters that will define the stage of ISM interaction and by extension the evolutionary state of the planetary nebula.

So far the PN-ISM interaction has mainly been detected in a rather small number of nebulae, which are generally bright objects ("young" and "mid-age" PNe). The low surface brightness, generally associated with nebulae mixing with the ISM and "old" PNe, has for a long time prevented any deeper observation and good statistical study of these interactions. The new generation of Hα surveys have surmounted this problem. Pierce et al. (2004), in the framework of the AAO/UKST Survey, discovered PFP 1, a large (radius = 1.5 $\pm$0.6 pc), faint (logarithm of the Hα surface brightness equal to -6.05 erg.cm^{-2}.s^{-1}.sr^{-1}, new PN, starting to interact with the ISM. This discovery has been followed by several others which are still candidates.

The depth reached by the IPHAS survey combined with the binning detection method allowed us to detect several interacting PNe candidates. We will adopt the definition of Wareing et al. (2007) to categorise our PNe. This recent investigation relies on three-dimensional hydrodynamic simulations at different ISM velocities and densities, and for different AGB mass loss rates. They listed four stages of interaction respectively named WZO1, WZO2, WZO3 and WZO4. The WZO1 stage corresponds to the "young" epoch defined by Rauch et al. (2000), the WZO2 stage corresponds to the " mid-age" epoch and the two last stages WZO3 and WZO4 can be correlated to the "old" epoch. The shapes observed and the corresponding definition of each stage are
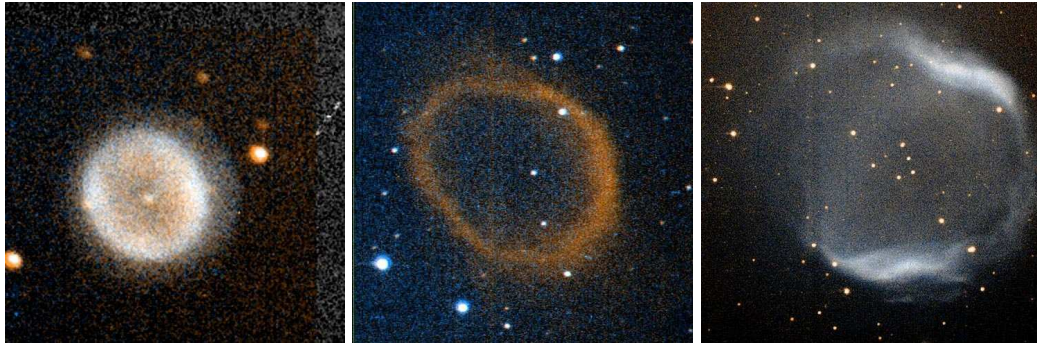
Figure 8.1: Example of planetary nebulae at different successive stages of ISM interaction. From left to right: Ba1, A 13 and Jn1. The images are taken from the "The Image Catalogue of Planetary Nebulae" of Bruce Balick (http://www.astro.washington.edu/balick/PNIC/) and are originally from the "IAC Morphological Catalog of Northern Galactic Planetary Nebulae" (Manchado et al. 1996)

given in Fig. 8.2 and Table 8.1. There is not much difference between the two groups concerning the global evolution of PNe with ISM interaction. The divergence arises when boundaries have to be set to determine the beginning and the end of a stage or epoch. The advantage of using the work of Wareing et al. (2007) is the possibility of a direct comparison between the observations and the predictions (models).
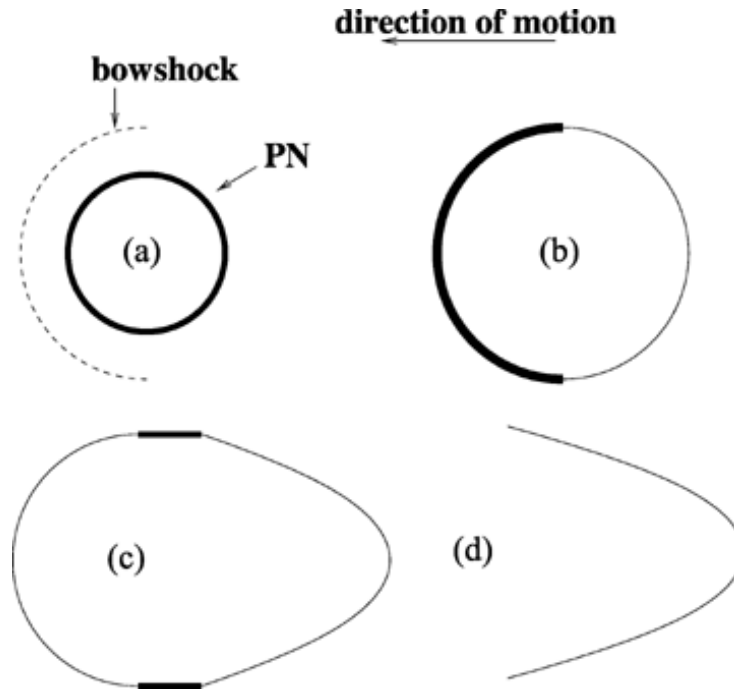
Figure 8.2: Nebular shapes for the four stages of interaction defined by Wareing et al. (2007). The letters a,b,c and d indicating the central star position.

Table 8.1: Definition of the four ISM interaction stages by Wareing et al. (2007).

Stage	Observable effects
WZO1	PN as yet unaffected; faint bow shock may be observable.
WZO2	Brightening of PN shell in direction of motion.
WZO3	Geometric center shifts away from central star.
WZO4	PN completely disrupted, central star is outside of the PN.

We found in our sample of 233 nebulae, 21 candidates which showed a morphology that can be linked to one of the stages described above, other than WZO1. A summary of these objects is shown in Table 8.2. In the following we will show all the PN candidates according their classification, and sketches describing the interaction process. The images are in Hα+[NII] if no other information is given.

- **WZO1**

We did not find any object showing a distant bow shock. In agreement with the definition of stage 1 of interaction, all but the WZO2, WZO3 and WZO4 classified candidate PNe, can be included in the WZO1 group.

- **WZO2**

IPHASX J185322.1+083018: There is no evidence of a full closed nebula and the only remaining structure is the well defined semi-circular bow shock (Fig. 8.3). We found 3 possible CS candidates based on the USNO[1] catalogues. Only the two brighter ones have an available B mag: 17.1 and 17.4 from the centre to the rim. This object, whose size assumes an original circular shape of about 1.8 arcmin in diameter, has its 2 bluer CS candidates moved away from the geometric centre towards the bright rim at +28 and +47 arcsec respectively. No other relevant data have been found regarding these candidates.

IPHASX J190338.5+104227: This large nebula (8.5 arcmin in diameter), shows a bright rim and also some nebular material inside what could have been a formerly round PN. The Hα-r image in Fig. 8.4 reveals a circular outflow ahead of the nebula which may or may not be related to the nebula. The bright central star candidate at 19:03:33.707 +10:44:01.33, (USNO B mag= 12) is located at +106 arcsec from the geometric centre in the rim direction. This CS candidate is linked to the ROSAT X-ray source RXS J190333.1+104355 ($10.8\pm1.7.10^{-2}$s^{-1} count rate) (Voges et al. 1999) and the NVSS/VLA radio source J190333+104409 (4.7±0.6 mJy). The CS is linked to a microquasar according to Paredes et al. (2002). A surrounding circular "outflow/jet" is observed in the bow shock direction but it was revealed by recent observation not to

---

[1]U.S. Naval Observatory: http://www.nofs.navy.mil/data/fchpix/
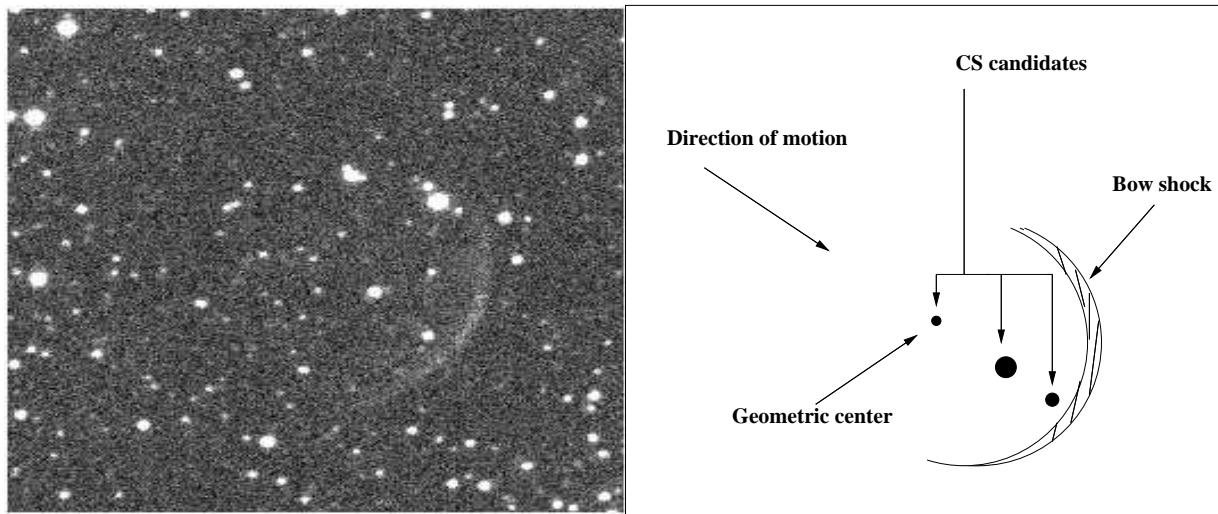
Figure 8.3: IPHASX J185322.1+083018. North on the Top and East.

be real.
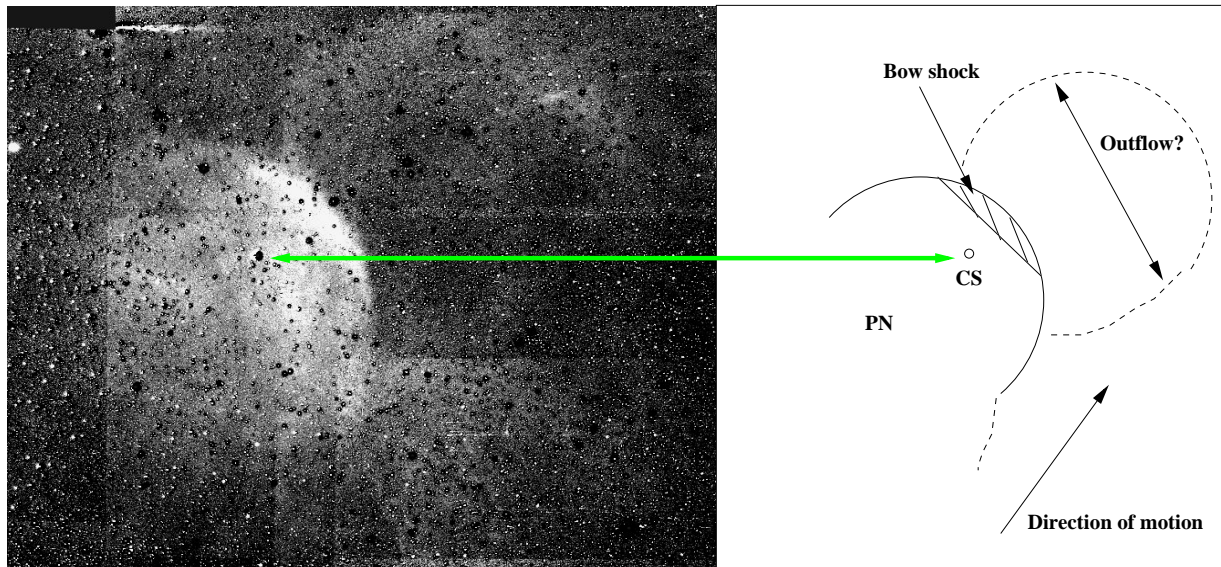
Figure 8.4: IPHASX J190338.5+104227. North on the Top and East on the left. The
Hα-r image has been scaled (adjusting the brightness levels) for display purposes.

IPHASX J190419.4+152126: This faint semi-circular ring, remnant of a large cir-
cular nebula (~8 arcmin), shows a linear enhancement of the brightness at the tip of

the bow shock (Fig. 8.5). The CS candidate has a USNO blue magnitude of 12.8 mag and is located at +1 arcmin from the geometric centre towards the bright rim. No other relevant data have been found on this star.
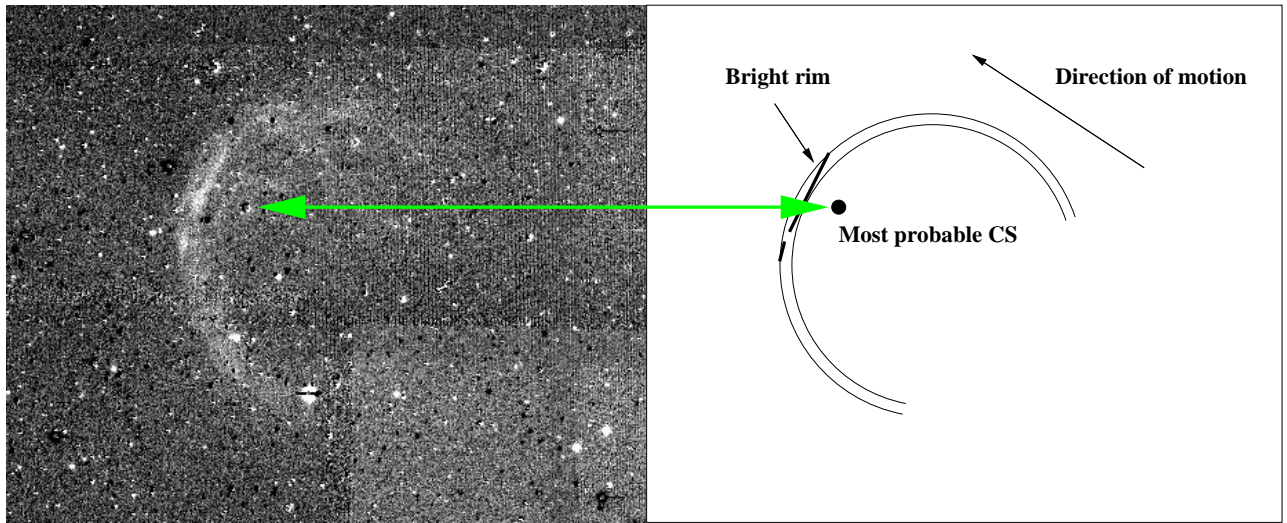
Figure 8.5: IPHASX J190419.4+152126. North on the Top and East on the left. The Hα-r image has been scaled for display purposes.

IPHASX J190454.0+101801: This small nebula (18 arcsec in diameter) shows a bright rim in the southern direction which may indicate the direction of motion (Fig. 8.6). The presence of stars on the nebula prevents us from seeing any opposite rim, which would indicate that we are dealing with a bipolar nebula. Assuming that the nebula shows an interaction with the ISM, we noticed on both eastern and western sides perturbations that may be linked to vortexes. These turbulent motions were well seen and described by Wareing et al. (2007) in their case b hydrodynamical simulations (their figure 3), but no tail is visible in our image. The central star candidate is quite faint and no data of interest have been found on it.

IPHASX J190512.4+161347: Contrary to first impressions, the direction of motion in this 1 arcmin diameter circular nebula, appears to be directed to the North-East (Fig.8.7). The bright straight rim in the western side is therefore a high density structure. Due to the geometry of the nebula, we expected to locate the CS near the geomet-
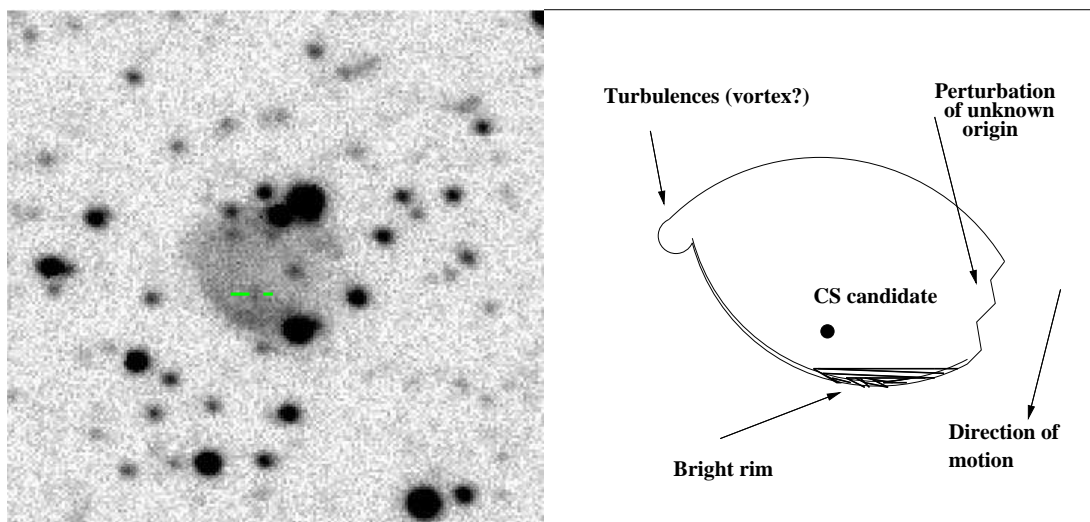
Figure 8.6: IPHASX J190454.0+101801. North on the Top and East on the left. The CS candidate is indicated by the two green dashes.

ric centre, and 3 faint stars can be classified as candidates. But none of them showed any relevant data. The whole configuration suggests that the nebula is in between stages 2 and 3 of interaction and is evolving relatively slowly (slow wind interaction). The nebula can be defined as ancient.
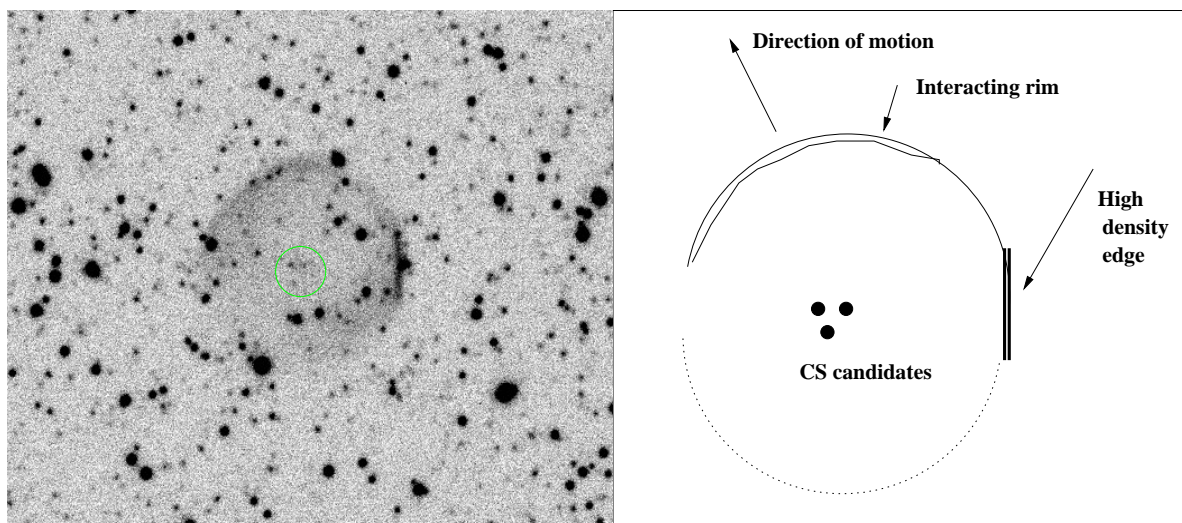

Figure 8.7: IPHASX J190512.4+161347. North on the Top and East on the left.

IPHASX J190654.9+052216: This nebula presents an eastern interacting thick rim (45 arcsec wide) (Fig.8.8). The CS candidate located at 19:06:57.357 +05:22:22.24, has a USNO B magnitude of 16.4 mag and is at +1.5 arcmin from the geometric centre in the rim direction.
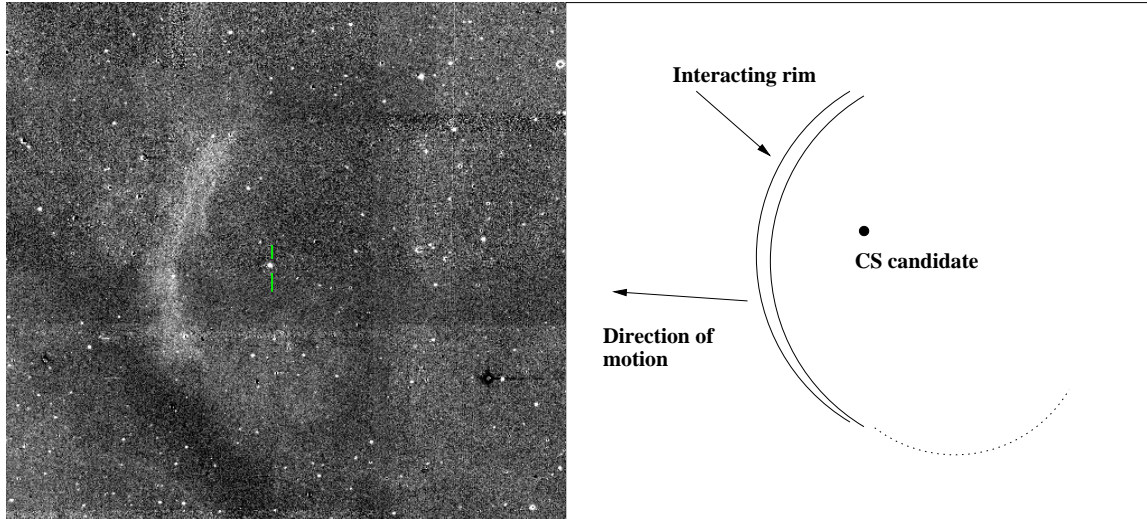

Figure 8.8: IPHASX J190654.9+052216. North on the Top and East on the left. The CS candidate is indicated by the two green dashes.

IPHASX J191421.1+140936: This small nebula (size of about 47 arcsec) reveals signs of ISM interaction in the North-West direction with a probable high density wall on the northern part (Fig. 8.9). The object would therefore be in the transition phase between stages 2 and 3. The best CS candidate (19:14:21.072 +14:09:41.88) has a blue magnitude of 18.2 mag and is located at +11 arcsec from the geometric centre in the direction of the rim. Unfortunately, no relevant data are known about this star.

IPHASX J192436.3+154402: This 20 arcsec size nebula possesses an interacting edge with the ISM on its South-East side and can be classified as WZO2 (Fig. 8.10). We do not have much data on the 2 candidates CS which have a blue magnitude of 19.4 and 19.7 mag.

IPHASX J192543.2+143546: This large nebula, also classified as a candidate SNR, interacts with the interstellar medium in the North-East direction and is still perfectly
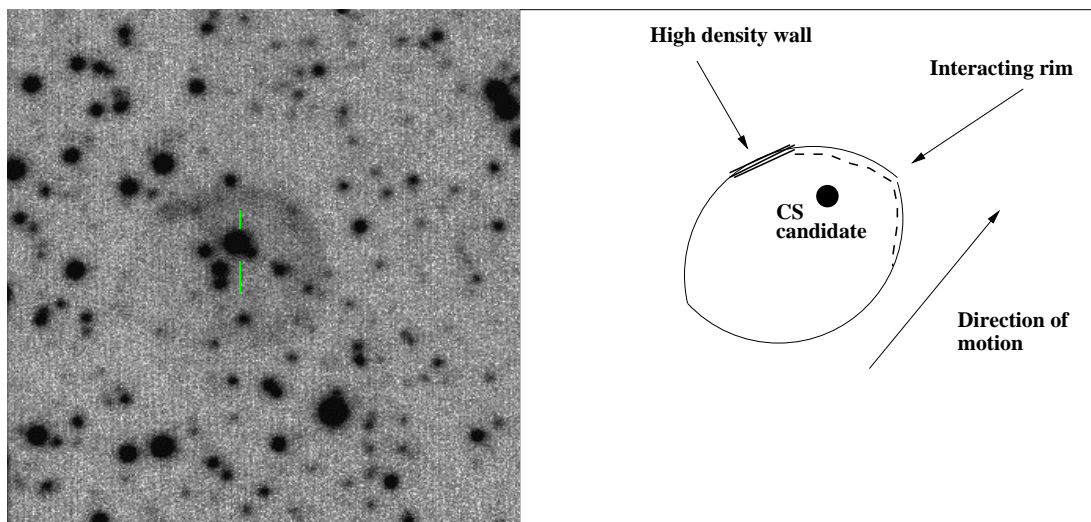
Figure 8.9: IPHASX J191421.1+140936. North on the Top and East on the left. The CS candidate is indicated by the two green dashes.
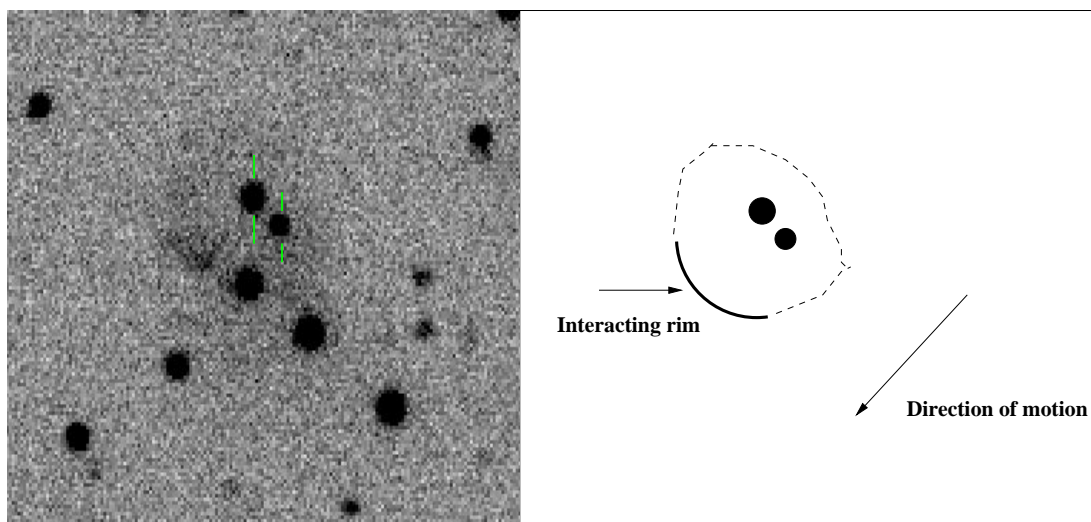

Figure 8.10: IPHASX J192436.3+154402. North on the Top and East on the left. The CS candidates are indicated by the two green dashes.

circular but any possible CS candidates remain unclear (Fig. 8.11).

IPHASX J193630.3+312810: This large semi-circular nebula (~ 7 arcmin) reveals a southern bow shock coincident with an interaction with the ISM (Fig. 8.12). The
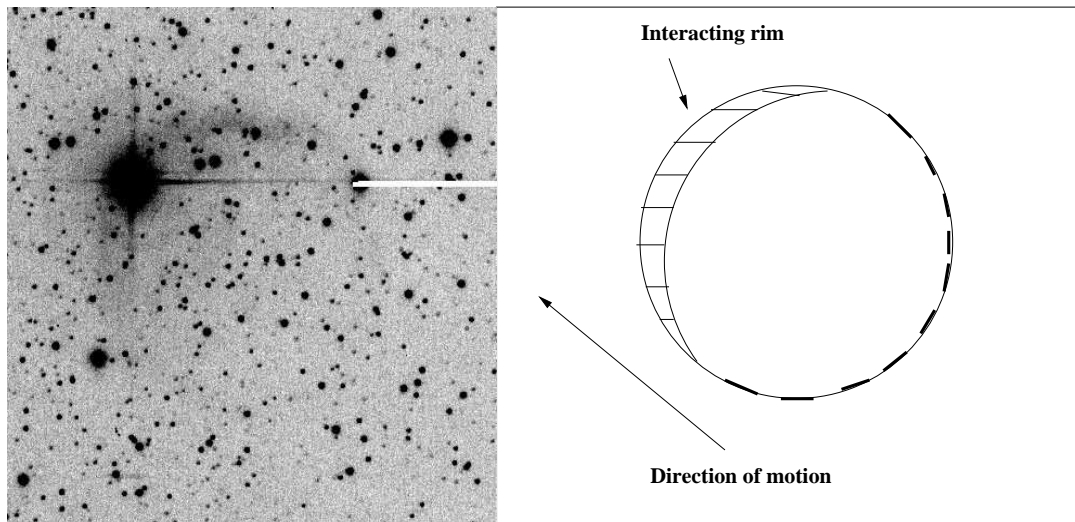
Figure 8.11: IPHASX J192543.2+143546. North on the Top and East on the left.

rim appears to be quite thin (width less than 10") and nearly filamentary. The best CS candidate (19:36:30.987 +31:26:01.77) has a blue magnitude of 14.2 mag and is at about +5.5 arcmin from the geometric centre in the rim direction. No relevant data are known about this star.
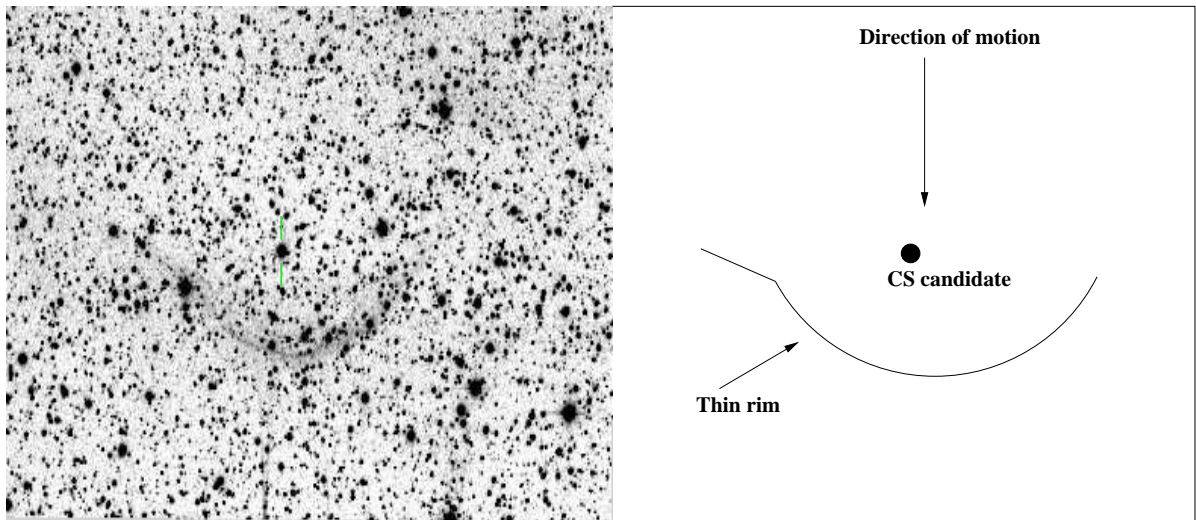
Figure 8.12: IPHASX J193630.3+312810. North on the Top and East on the left. The CS candidates is indicated by the two green dashes.

IPHASX J193637.3+123808: This round nebula is a perfect example of stage 2 of interaction as it shows shell completion and a bright edge in the direction of motion (North-East)(Fig. 8.13). The bluest star and CS candidate, at +80" from the geometric centre in the rim direction, has a magnitude of 14.2 (19:36:39.488 +12:38:38.05) but no other information is available.
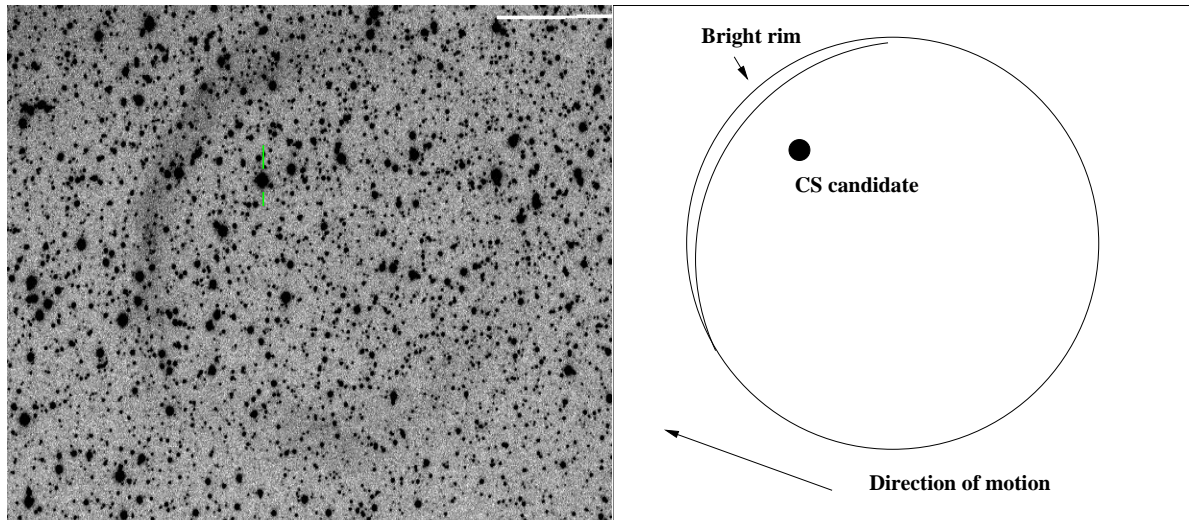

Figure 8.13: IPHASX J193637.3+123808. North on the Top and East on the left. The CS candidates is indicated by the two green dashes.

IPHASX J194204.9+231932: This small nebula (size 15") shows a well defined bright front in the South-East direction and is nearly a closed structure (Fig. 8.14). The geometry of the source does not allow us to identify a CS candidate, the latter seeming not to be visible (maybe hidden by the internal extinction) .

IPHASX J194240.6+275109: This object is a circular nebula with a semi-circular rim enhancement towards the South (Fig. 8.15). The material at the rear of the bright edge is quite faint but still contributes to a closed nebula. The best CS candidate (for geometric and magnitude concerns) is the star with the coordinates 19:42:41.262 +27:50:45.86, located at +26 arcsec from the geometric centre in the edge direction. Its blue magnitude is 15.7. There is no other useful information available about it.

IPHASX J194645.3+262211: This large semi-circular nebula shows a bright rim
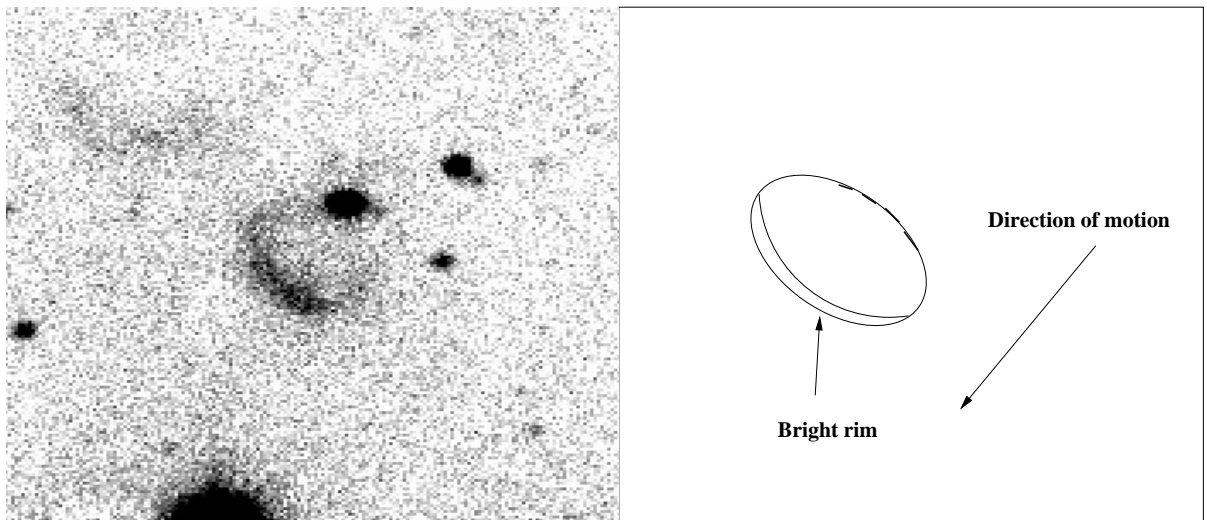
Figure 8.14: IPHASX J194204.9+231932. North on the Top and East on the left.
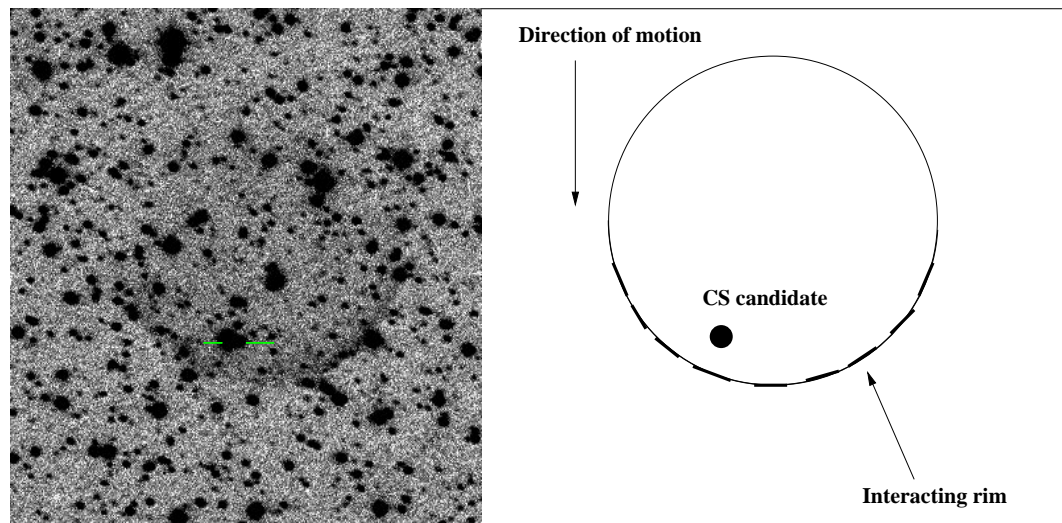
Figure 8.15: IPHASX J194240.6+275109. North on the Top and East on the left. The CS candidate is indicated by the two green dashes.

in the South-East direction and there seems to be fainter surrounding material in the whole southern part which may belong to the nebula (Fig. 8.16). The field is quite crowded and there is no obvious CS candidate. We can only state that due to the geometry of the nebula, the CS will have a B mag fainter than 16. If we consider that

only the bright rim is part of the PN candidate, the best CS candidate (coordinates: 19:46:51.770 +26:21:26.24) has a USNO B mag of 16.1 and is located at +118 arcsec from the geometric centre in the direction of the edge.
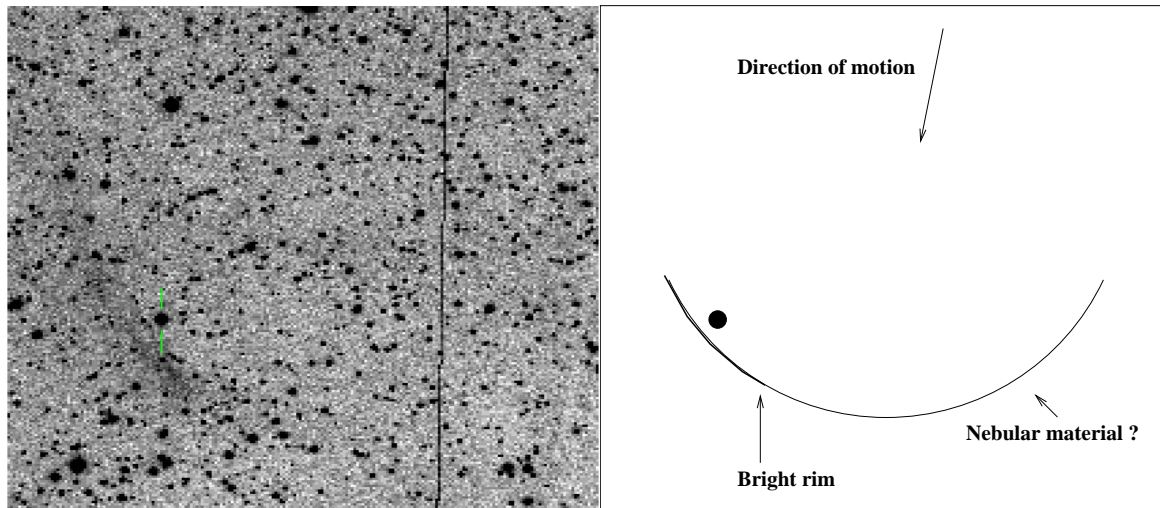

Figure 8.16: IPHASX J194645.3+262211. North on the Top and East on the left. The CS candidates is indicated by the two green dashes.

IPHASX J194727.6+230816: The ISM interaction in this "small" (37 arcsec in diameter) round nebula occurs in the South-West side where we can see a density enhancement (Fig. 8.17) and flattening of the candidate PN. The rest of the nebula is perfectly defined. For the first time the CS seems to be well identified, coinciding with the geometric centre at coordinates 19:47:27.554 +23:08:16.31. The USNO B1.0 catalogue gives a very faint B2 magnitude of 20.40. A compact second shell (about 5 arcsec in diameter) seems also be present in the central part of the nebula. Deeper imaging is needed to confirm this presence.

IPHASX J194852.7+222516: This small nebula (21 arcsec in diameter) is composed of roughly 2 shells/rings (Fig. 8.18). The outer shell has a round morphology while the inner shell tends to show a bipolar shape. The Southern part of the object is density enhanced which would indicate an interaction with the ISM in that direction. Considering that the original shape of the nebula was not round but bipolar, we can
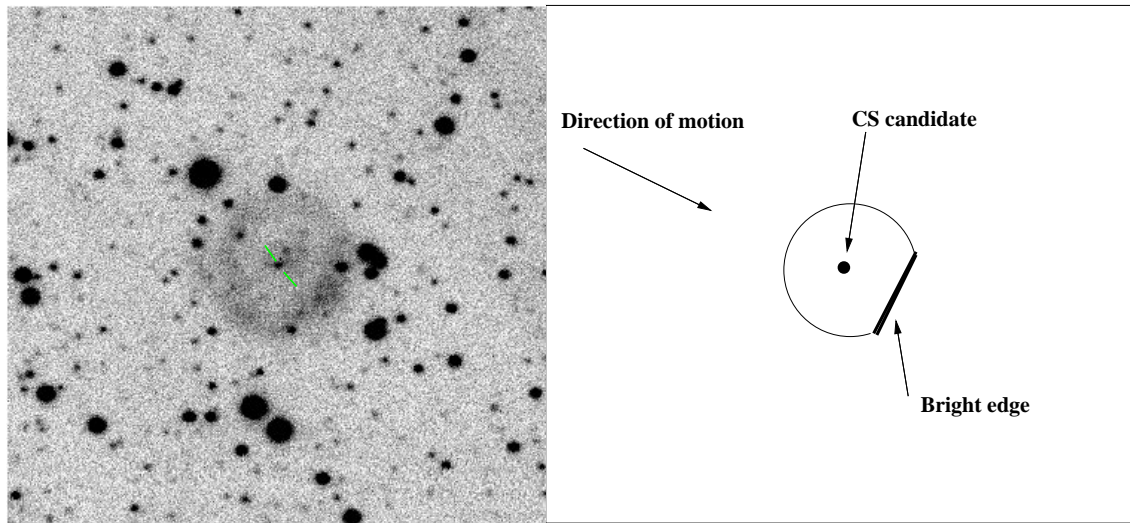
Figure 8.17: IPHASX J194727.6+230816. North on the Top and East on the left. The CS candidate is indicated by the two green dashes.

assume, that while moving into the ISM, the bow shock was deformed and the nebular material pushed backward and accumulated in the waist, enhancing the size of the nebula in this region. There is no obvious information on the best CS, but according to the blue magnitude of the stars in the area, we can assume that our CS will be fainter than B=20 mag.

IPHASX J195357.9+312130: The disrupted geometry of this large nebula indicates that it could be highly evolved (Fig.8.19). The long bow shock front, in the North-East direction, is thick ($\sim$ 25 arcsec wide) and diffuse. The crowded field made it difficult to identify the CS but we can give an upper B mag limit of 16 mag, assuming that the CS has not left the nebula.

- **WZO3**

IPHASX J185744.5+105053: The irregular distribution of the nebular material complicates the classification of this nebula in a stage of interaction (Fig. 8.20). Two scenarios are possible. First, the nebula displays a motion in the North-West direction,
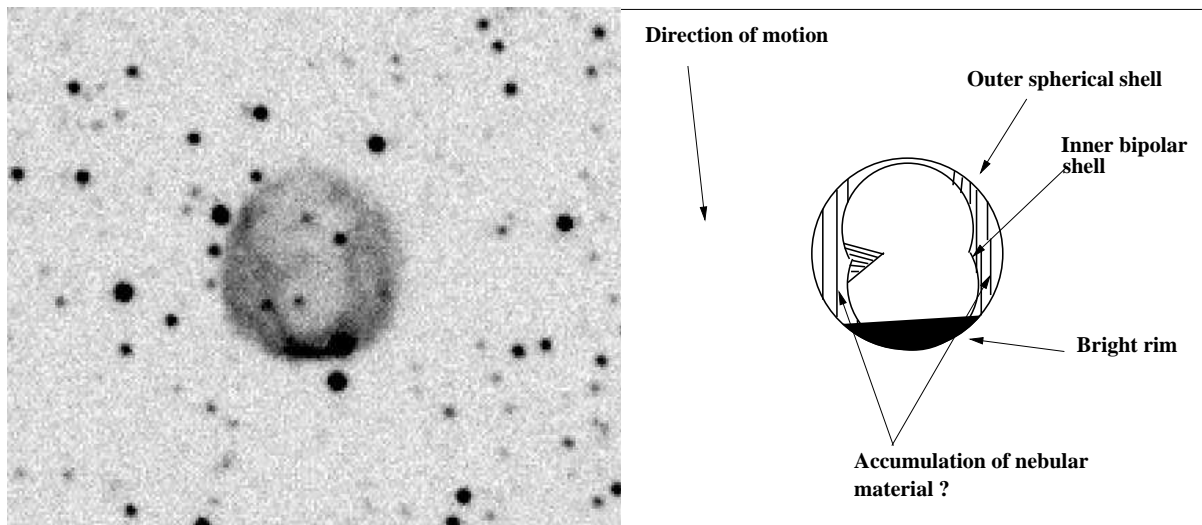
Figure 8.18: IPHASX J194852.7+222516. North on the Top and East on the left.
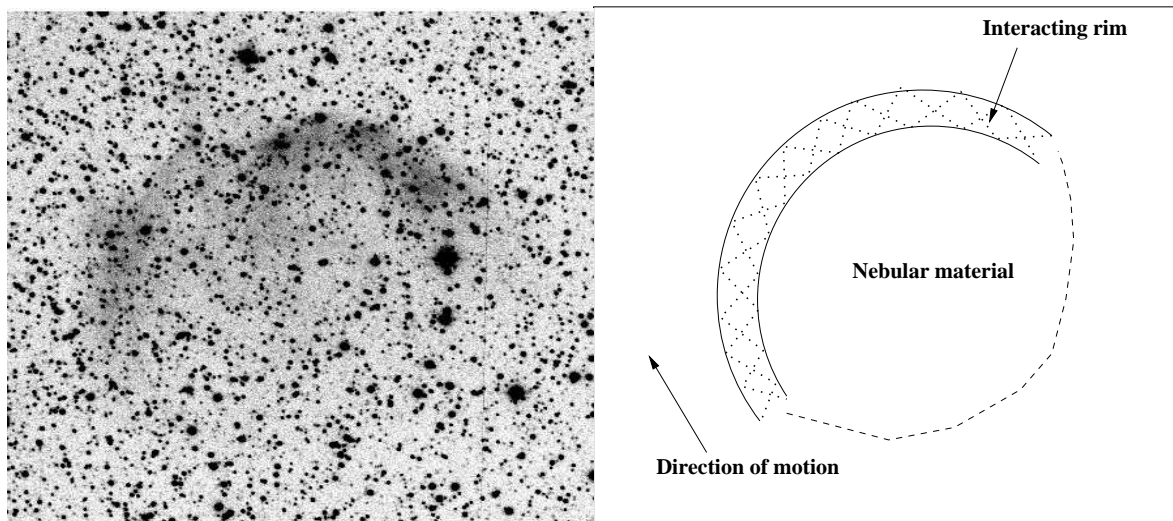
Figure 8.19: IPHASX J195357.9+312130. North on the Top and East on the left.

and the bright western edge and its opposite side are the result of the beginning of a sweeping process of the nebular material localised on the front side (with an asymmetry in the distribution). This material is flowing towards the back of the nebula. In the second hypothesis, th direction of motion is in the opposite South-East direction. In this case the bright edge is the final result of the move backwards of the nebular matter

leaving the front part of the nebula totally empty. In both cases we are in between stages 3 and 4 of interaction, the second scenario being closer to the WZO4 scheme. The best CS candidate has a blue magnitude of 15.9 and its location (18:57:44.804 +10:50:53.55) coincides with both hypotheses.
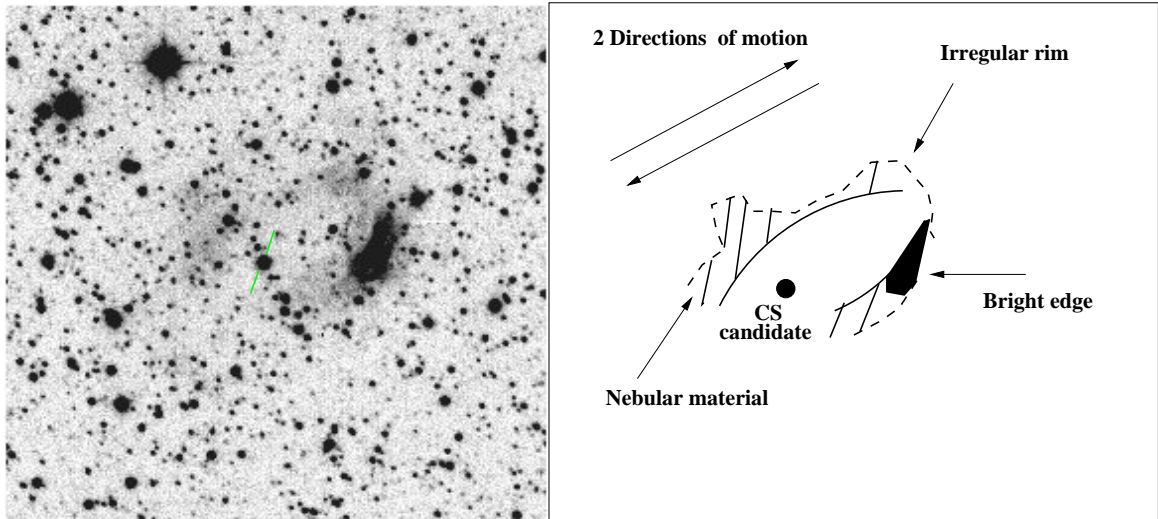

Figure 8.20: IPHASX J185744.5+105053. North on the Top and East on the left. The CS candidate is indicated by the two green dashes.

IPHASX J190700.7+043041: This 18 arcmin wide semi-circular nebula is the largest of our sample (Fig. 8.21). It shows two opposite thick bright rims on the North and the South, with the southern one revealing a greater density enhancement and a filamentary general structure. It is unclear how to classify this object as it is surrounded by SNRs and we see the presence of filaments in the South and North-West part of the nebula. Moreover a pulsar, PSR J1906+0414, is located at 16 arcmin from the geometric centre. Combined with the presence of the X-ray source 1RXS J190709.4+043100 at 131 arcsec from the centre of the nebula, this object has therefore also been classified as a candidate SNR. Assuming that IPHASX J190700.7+043041 is a genuine PN candidate, it would be defined as an ancient remnant of a PN mainly moving into the ISM in the eastern direction. The nebular material has shifted on the sides and progressively left the front part depleted, explaining the two opposite bright rims and the

fainter foreground. The filaments seen near the high density southern part would be associated with turbulences/vortexes, as also predicted by the hydrodynamical models. The large scale field did not allow us to define a good CS candidate but we can state that its upper B magnitude will be around 12.6.
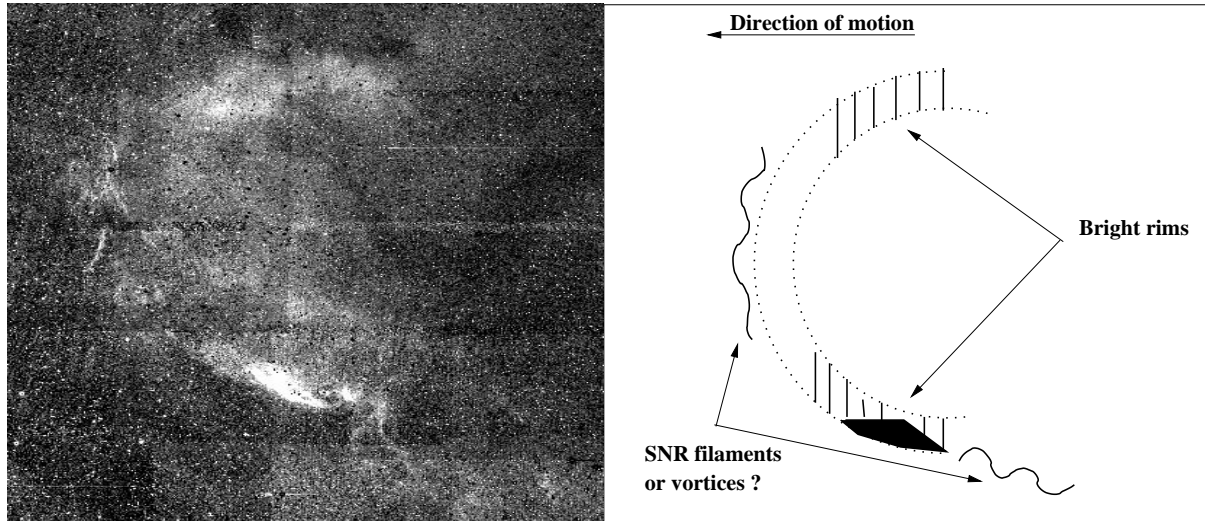

Figure 8.21: IPHASX J190700.7+043041. North on the Top and East on the left. The Hα-r image.

IPHASX J192221.5+151550: The geometry of this nebula reveals a narrow bow shock (~90 deg aperture) indicating a high speed object colliding with the ISM in a North-South direction (Fig. 8.22). The central star, located at 19:22:21.406 +15:15:45.92, is very faint and situated very close to the bow shock's tip (at 10 arcsec from it).

- **WZO4**

IPHASX J190227.3+020815: This nebula is typical of stage 4 of ISM interaction as defined by Wareing et al. (2007) (see their figure 5.d) (Fig. 8.23). The interacting part is not the brighter side of the nebula in the South-East but the opposite thin and faint arc in the North-West. The object reaches a stage where all its matter has been moved from the front to the rear leaving only a remnant "wall" of matter. The most probable CS (19:02:27.032 +02:08:18.12) has a B magnitude of 16 and is located at
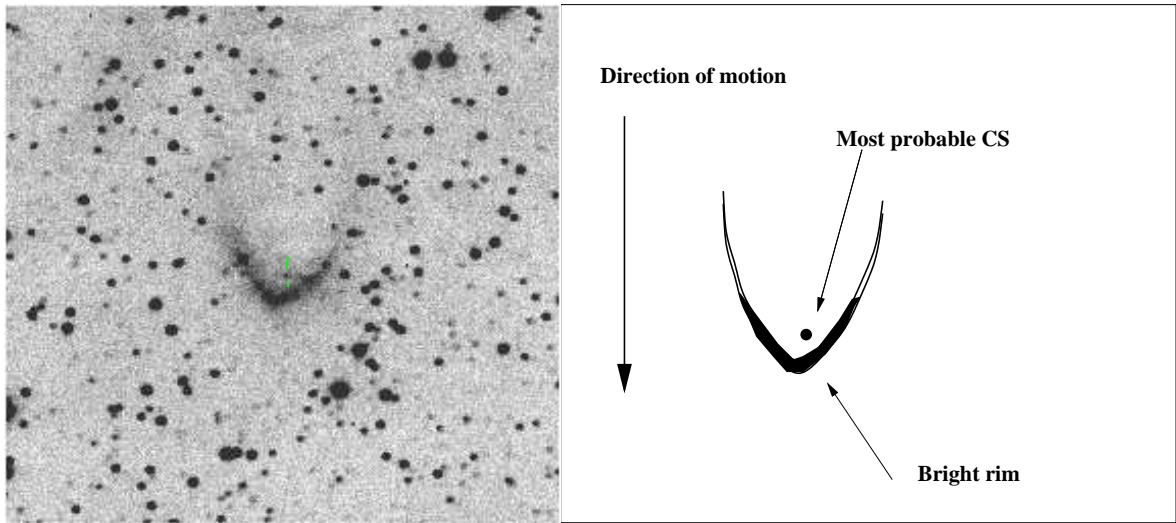
Figure 8.22: IPHASX J192221.5+151550. North on the Top and East on the left. The CS candidate is indicated by the two green dashes .

~30 arcsec from the interacting rim in the North-South direction.
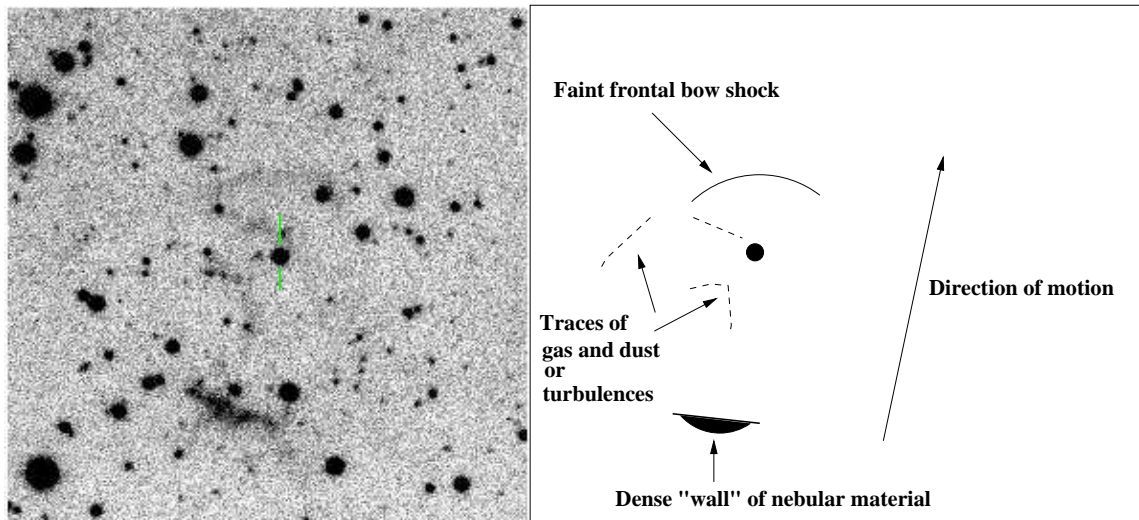

Figure 8.23: IPHASX J190227.3+020815. North on the Top and East on the left. The CS candidate is indicated by the two green dashes .

The systematic visual identification of candidate planetary nebulae with ISM inter-

action has been delayed by the difficulty in detecting them. We show in Table 8.2, the surface brightness (SB) of the 21 candidate PNe. This type of measurement for these particular objects has its limits in the sense that it relies on the selected surface of the PNe. Indeed, there is no written rule on what should be considered as the surface of a partially seen PN/ISM (from the WZO1 to WZO4 type, this difficulty increases): do we only take into account the "visible" part of the nebula or should we assume, when possible, that the remnant rim was part of the original geometric structure (e.g. for a semi-circular rim)? Ideally, a multi-wavelength coverage would give us the total extent of the nebula, but as we only have the Hα+[NII] images we will assume that the surface is bounded by the observed emission and no assumptions regarding the geometric surface will be used.

The method used to derive the SB is the same as mentioned earlier for the distance determination. But we must underline that there is no correction for reddening. So the surface brightnesses derived are the observed surface brightnesses. The lack of spectra prevent any de-reddening, and the use of Schlegel et al. (1998) maps is not recommended as we are looking in a really dusty area, and they derived the extinction in lines of sight. The correct visual extinction may be considerably under or overestimated.

The results obtained show that although the SB is morphology dependent, there is no relation with the different interaction stages. Hence the brightest and faintest objects both belong to the WZO2 stage. This underlines the fact that, first, PNe do not necessarily go through all the stages of interaction before fading into the ISM, probably due to a slow evolution. And secondly, the IPHAS sensitivity allowed us to detect those very evolved PNe with very low surface brightness.

8.2 Comparison with hydrodynamical models

A deeper investigation into the link between the morphologies of the candidate PNe and the different hydrodynamical models (divided in 5 cases) from Wareing et al.

Table 8.2: Summary of the IPHAS nebulae with signs of ISM interaction.

IPHASX J	Morphology	Size[1]	Stage	SB undereddened [2]	SB Area[3]
185322.1+083018	R	110	WZO2	1.075e-16	1008
185744.5+105053	E	110	WZO3/WZO4	4.978e-16	11090
190227.3+020815	I	106	WZO4	2.038e-16	1259
190338.5+104227	R	512	WZO2	1.738e-16	73971
190419.4+152126	R	470	WZO2	1.981e-16	6205
190454.0+101801	R	18	WZO2	2.506e-15	241
190512.4+161347	R	66	WZO2/WZO3	1.178e-15	2856
190654.9+052216	R	464	WZO2	9.483e-18	33333
190700.7+043041	R	1090	WZO3	7.787e-16	12220
191421.1+140936	R	47	WZO2/WZO3	6.800e-16	1111
192221.5+151550	I	44	WZO3	1.107e-15	1074
192436.3+154402	E	20	WZO2	3.821e-16	387
192543.2+143546	R	176	WZO2	3.172e-16	10391
193630.3+312810	R	404	WZO2	1.115e-17	6797
193637.3+123808	R:r	262	WZO2	2.676e-16	21613
194204.9+231932	E:r	15	WZO2	3.892e-15	207
194240.6+275109	R	74	WZO2	3.387e-17	2822
194645.3+262211	R	290	WZO2	3.508e-17	4950
194727.6+230816	R	37	WZO2	1.164e-15	1042
194852.7+222516	R	21	WZO2	4.454e-15	413
195357.9+312130	R	212	WZO2	3.795e-16	25682

[1] in arcsec, [2] in erg cm^{-2} s^{-1} arcsec^{-2}, [3] in arcsec^2

(2007) will help to reveal more information. We concentrated on the cases starting from their case B, which shows the evolution of the nebula in the post-AGB phase.

The comparisons should give us data on the structures present but not detected (due to the wavelength used for example) and data on the velocity of the nebulae relatively to the ISM (this will be an estimation as the distance is required in order to define a *bona fide* velocity).

• The majority of the WZO2 candidate PNe only show a semi-circular bow shock and, no tail or external distant halo are seen nor any perturbation in or near the front shock. The observations can be associated with the Case B simulation b of Wareing et al. (2007). Fig 8.24 shows the typical ISM interaction of IPHASX J185322.1+083018 as an example and the corresponding hydrodynamical model. The physical parameters linked to this model are a velocity in the ISM of 50 km s^{-1} and an evolution of 10 000 years in the PAGB phase. One WZO2 object, IPHASX J190454.0+101801, shows
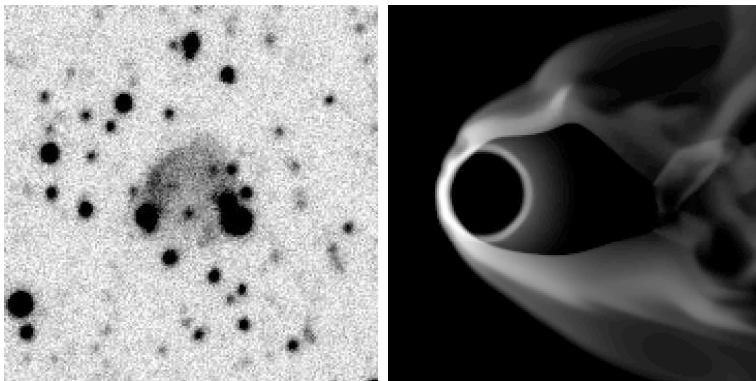

Figure 8.24: Comparison observation/model for the general WZO2 interaction process.IPHASX J190454.0+101801 has been rotated 90 deg clockwise to match the model.

possible perturbations at the edges of the bow shock and can be linked to an advanced step: Case B simulation c. In Fig 8.25, the evolutionary stage is 20 000 years.

IPHASX J190512.4+161347 and IPHASX J191421.1+140936 have been classified as transition objects from WZO2 to WZO3 (Fig. 8.26). The accumulation of nebular material at the rear of the front shock can also be represented by the case (B,b)
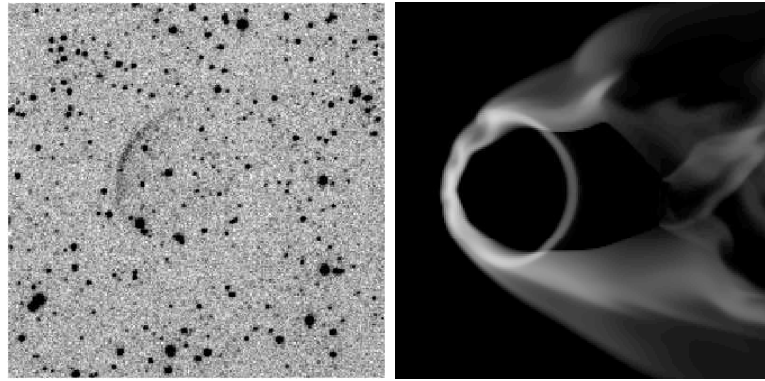
Figure 8.25: Comparison observation/model for IPHASX J190454.0+101801. The IPHAS image has been rotated to match the model.

or (B,c) models although no vortexes are seen. Finally, the PN bipolar interaction with the ISM observed in IPHASX J194852.7+222516 has not been treated by Wareing et al. (2007).

• The candidate PNe belonging to the WZO3 and WZO4 stages of interaction show the most irregular features which place them either in the group of the very evolved PNe or the one with an higher velocity in the ISM.
IPHASX J190700.7+043041 (Fig. 8.27) shows a depleted front and structures and an accumulation of the nebular material on the side. Assuming that the structures described as filaments (and which is one factor which could classify the object as a potential SNR) are in fact perturbations or vortexes due to RT instabilities, the best correlation made is with the model case (B,d) where the velocity is still at 50 km s^{-1} but the evolutionary phase is 30 000 years in the PAGB. The same classification is made for IPHASX J185744.5+105053 (Fig. 8.27), although its general morphology is more complex.

The singular shape of IPHASX J192221.5+151550 (Fig. 8.28), with a narrow opening angle, suggests a higher velocity than the one dealt with before. Thus, the model that fits this behaviour is Case D,a. The velocity of the CS relative to the ISM is
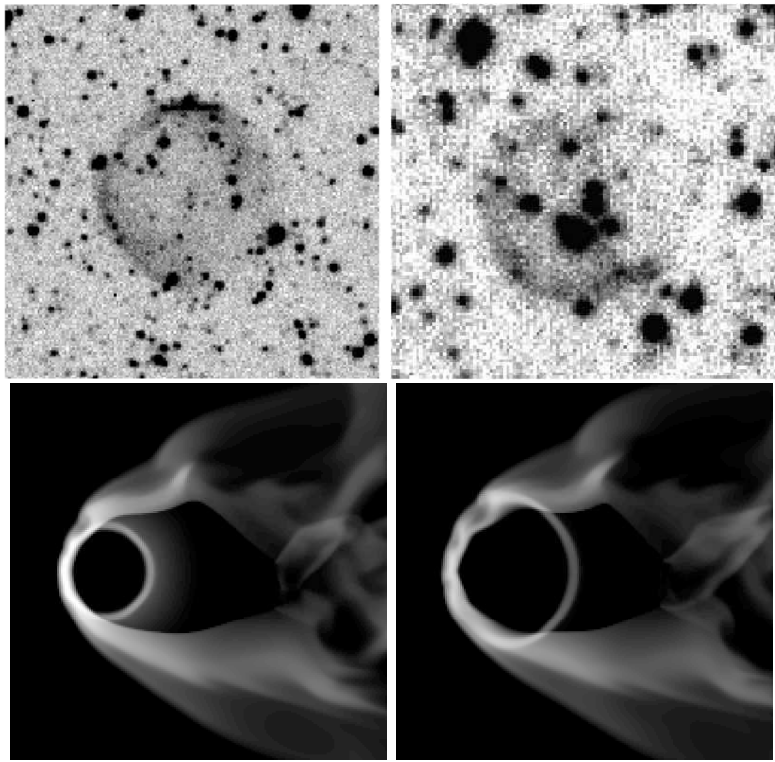
Figure 8.26: Comparison observation/model for IPHASX J190512.4+161347 (rotated 90 deg anti-clockwise) and IPHASX J191421.1+140936 (rotated 180 deg anti-clockwise).
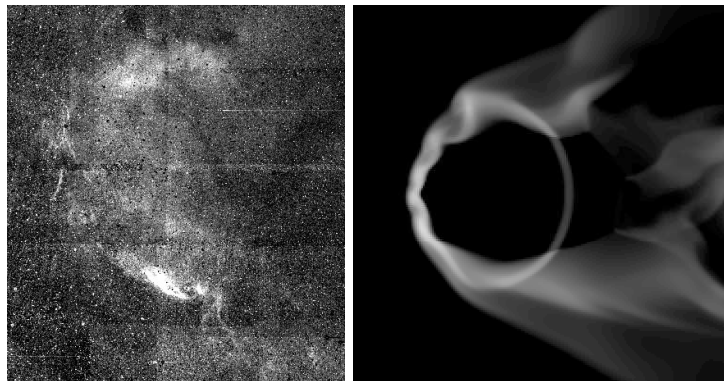

Figure 8.27: Comparison observation/model for the WZO3 IPHASX J190700.7+043041 and IPHASX J185744.5+10505.

100 km s^{-1} and the simulation shows the phase at the end of the AGB. The candidate PN is therefore much younger than all the ones cited before, but the speed of the CS has strongly affected the shape of the nebula.
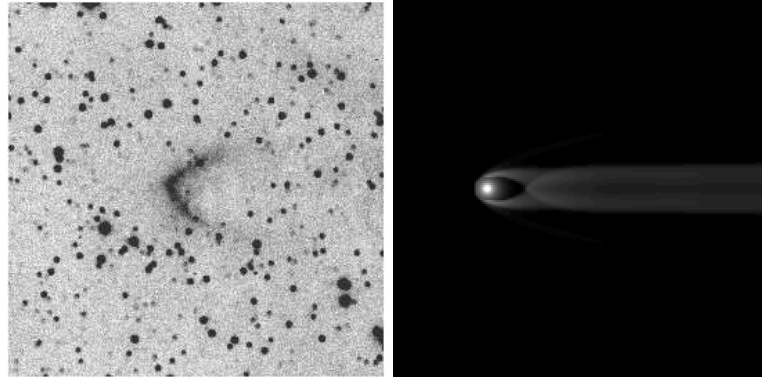

Figure 8.28: Comparison observation/model for the WZO3 IPHASX J192221.5+151550. The IPHAS image of the nebula has been rotated to match the model.

Finally the WZO4 candidate PN, IPHASX J190227.3+020815 is probably one of the best described by the models. The dense "wall" of nebular material located behind the semi-circular bow shock as well as its curvature are well seen in the model D simulation d. Moreover the presence of features which could be linked to turbulence are observed in the nebula. This corresponds to a velocity in the ISM of 100 km s^{-1} and an evolution of 10 000 years in the PAGB phase. But the bow shock is not large enough to make any extrapolation on the exact type of corresponding simulation (b,c or d), so simulation b will represent the lower limit on the physical parameters of our nebula. The CS of IPHASX J190227.3+020815 would therefore evolve at a lower limit of 100 km s^{-1} in the ISM and would be at 1000 years in the PAGB phase (the simulation "c" is at 2000 years in the PAGB phase).
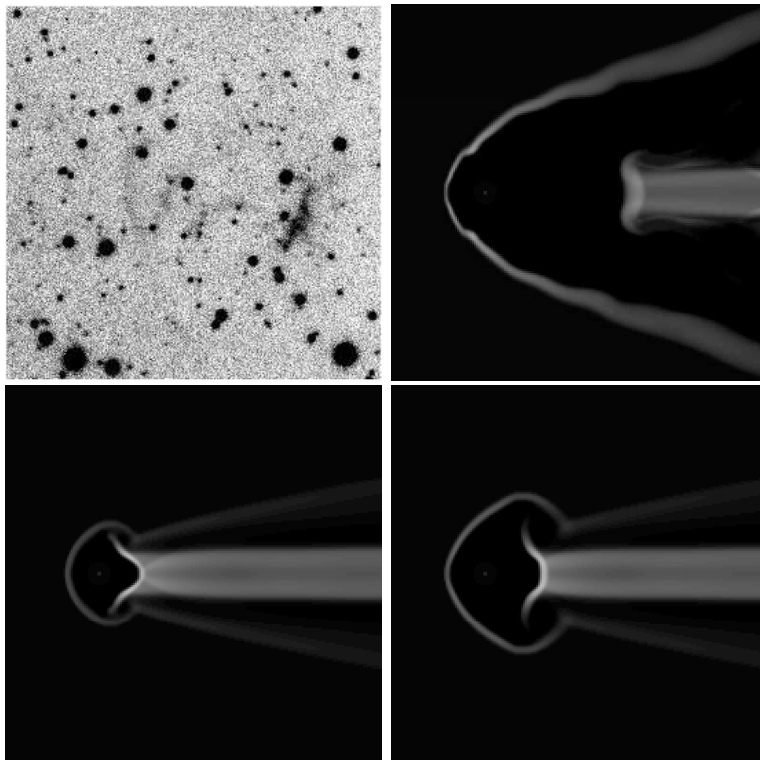
Figure 8.29: Comparison observation/model for the WZO4 IPHASX J190227.3+020815. From Case D:d (top right), CaseD:b (bottom left), Case D:c (bottom right). The IPHAS image of the nebula has been rotated 90 deg anti-clockwise to match the models.

8.3 Identification of the CS Candidates: Direction and Proper motions

The measurement of the proper motion (PM) and direction of motion of the candidate central stars will allow us to clarify the relationship between the stars and the nebula surrounding them. The method simply consists in comparing both directions of motion (bow shock and CS), which should be the same. Cudworth (1974) and Kerber et al. (2008) also measured the PM of some planetary nebulae including PNe with ISM inter-action. This type of search is not extensive for PNe/ISM due to the relative difficulty of observing the CS which can be too faint or not visible at all. Our investigation is based

on the positional accuracy in the IPHAS catalog (rms ≤ 100 mas: Gonzalez-Solares et al. (2007)) linked with previous (astrometric) observations from the USNO-B catalog (Monet et al. 2003) and the 2MASS point source catalog (Cutri et al. 2003). The results are listed in Table 8.3. Among the 21 targets, we were able to retrieve data for 13 of them.

- Three candidate PNe have their candidate CS evolving in the same direction as their bow shock: IPHASX J185322.1+083018, IPHASX J190338.5+104227 and IPHASX J190419.4+152126 (the two first having the largest proper motion of the sample, 37±5 and 56±9 mas yr^{-1} respectively).

- Three candidate CS moves towards their probable related bow shock but with an angle greater than expected, which leads to an orientation towards the edges of the rim. As there is no evidence for an enhancement of the rim in those directions, the relation between the CS and the nebulae remains unclear. IPHASX J190654.9+052216, IPHASX J191421.1+140936 and IPHASX J194240.6+275109 are involved.

- The candidate CS of IPHASX J185744.5+105053 shows a perpendicular direction of motion relatively to the 2 possible directions identified. The movement does not discard the star as the genuine CS and may reflect the true direction of motion of the nebula.

- The remaining stars either have their motions which do not fit with the motions of the nebulae or can be considered as nearly static (like IPHASX J194645.3+262211, IPHASX J 193637.3+123808 and IPHASX J193630.3+312810).

Deeper spectroscopic analyses are needed to identify the true CS. The total velocity of the CS can be separated into two components, the radial and transverse velocity. The transverse velocity v$_t$ is a function of the proper motion and distance of the CS and can

be derived as followed:

$$v_t = \frac{PM \times d}{206265} \tag{8.1}$$

with PM in arcsecond yr^{-1} and 206265 is used to obtained radian yr^{-1}. If the distance is set in term of parallax, the equation becomes:

$$d = \frac{206265 \times 1AU}{p} \tag{8.2}$$

and

$$v_t = \frac{PM \times 4.74}{p} \tag{8.3}$$

with p the parallax in arcsecond.

We therefore attempted to calculate the transverse velocity for our 3 best candidate CS. Unfortunately no data on the parallax has been found for any of them in the catalogues used. (Regarding the velocity dispersion of the PNe in our latitude range, Schneider et al. (1983) and Pottasch (1984) define a radial velocity range between ~25 and ~60 km/s (up to ~100 km/s for some objects))

Table 8.3: Proper motions of the candidates CS and direction of motion. The total proper motions are corrected from galactic rotation and solar motion.

IPHAS Name	CS	PM Ra (mas yr^{-1})	PM Dec (mas yr^{-1})	Total PM (mas yr^{-1})	PA (deg)
185322.1+083018	CS1:Geometric center	-29 ± 7	-24 ± 4	32 ± 6	226
	CS2:Middle	-3 ± 3	-8 ± 2	2 ± 2	218
	CS3:Near rim	-10 ± 3	-3 ± 3	8 ± 3	225
All CS evolve towards the bow shock. Best candidate: CS1.					
185744.5+105053	CS1	-2 ± 3	-16 ± 2	10 ± 3	193
CS moves in North-East/South-West direction, perpendicularly to any direction of motion.					
190227.3+020815	CS1	0 ± 1	-5 ± 1	2 ± 1	166
CS moves in direction exactly opposite to bow shock, towards bright structure					
190338.5+104227	CS1	-24 ± 10	51 ± 7	60 ± 9	327
CS moves in direction of bow shock.					
190419.4+152126	CS1	3 ± 7	4 ± 3	11 ± 7	31
CS moves in direction of bright bow shock.					
190454.0+101801	CS1	-	-	-	-

Table 8.3 – continued .

IPHAS Name	CS	PM Ra (mas yr^{-1})	PM Dec (mas yr^{-1})	Total PM (mas yr^{-1})	PA (deg)
190512.4+161347	CS1	-	-	-	-
190654.9+052216	CS1	-2 ± 2	-7 ± 1	2 ± 2	198
Direction of motion: upper end of the bow shock					
190700.7+043041	CS1	-	-	-	-
191421.1+140936	CS1	-4 ± 4	19 ± 4	24 ± 4	344
Direction of motion: upper part of the bow shock					
192221.5+151550	CS1	-	-	-	-
192436.3+154402	CS1:Upper star	-14 ± 16	-12 ± 14	13 ± 13	230
Direction of motion: parallel to bright rim towards North-East					
	CS2:Lower star	-26 ± 6	-27 ± 5	32 ± 6	223
Direction of motion: parallel to bright rim towards South-West					
192543.2+143546	CS1	-	-	-	-
193630.3+312810	CS1	-14 ± 7	3 ± 5	14 ± 5	284
Direction of motion: West, nearly parallel to rim.					
193637.3+123808	CS1	-4 ± 2	0 ± 3	6 ± 3	291

Table 8.3 – continued .

IPHAS Name	CS	PM Ra (mas yr^{-1})	PM Dec (mas yr^{-1})	Total PM (mas yr^{-1})	PA (deg)
Direction of motion: North-West, nearly parallel to rim.					
194204.9+231932	CS1	-	-	-	-
194240.6+275109	CS1	9 ± 10	-30 ± 3	28 ± 6	166
Direction of motion: South-East, towards eastern part of rim					
194645.3+262211	CS1	-6 ± 3	1 ± 2	7 ± 2	287
Direction of motion: Towards the interior of the nebula					
194727.6+230816	CS1	-11 ± 6	5 ± 6	13 ± 6	297
CS moves nearly parallel to the rim , in North-West direction					
194852.7+222516	CS1	-	-	-	-
195357.9+312130	CS1	-	-	-	-

8.4 Discussion

The ISM is more dense in the Galactic Plane than in the zone towards the anti-centre or the zone above a height of 100 pc (from observation of neutral hydrogen gas, Dickey and Lockman (1990)). We therefore expected a greater influence of the interaction process in this area.

It appears that the majority of the IPHAS nebulae which show an interaction with the ISM correspond to stage 2 of interaction (17 objects of the sample) and show a rather circular morphology. According to Wareing et al. (2007), this is a relatively short period in the interaction process ($\sim$1000 yrs). This conclusion is the same for the known PNe listed by Borkowski et al. (1990) and the ones in the "IAC Morphological Catalog of Northern Galactic Planetary Nebulae" (Manchado et al. 1996). We notice that only 3 nebulae display a stage 3 interaction and one a stage 4 and these are classified as irregular nebulae. Phase transitions are also observed. The fact that a stage 4 is detected in IPHAS is quite important as first we would expect more cases in other regions of the Galactic Plane and because we are now able to study PNe at the very end of their life in terms of geometry, abundances...etc.

While most of the detected candidate PNe are large, i.e with a size greater than 100 arcsec, or of medium size i.e. between 20 and 100 arcsec, small nebulae also show signs of interaction. This confirms that the ISM interaction process does not a priori only imply "old" nebulae. Figure 8.30 shows that the large objects are spread all over the latitude range but mainly reside at higher latitudes than smaller nebulae (which coincides with our general knowledge about the location of PNe) but the interesting point is the fact that we also detect large objects in zones of high extinction. Thus, 5 candidates with a size larger than 100 arcsec are located in an area with E(B-V) up to $\sim$13 mag (i.e. a latitude range between -2 deg and 1 deg). Those objects, IPHASX J190227.3+020815 (2'), IPHASX J190654.9+052216 (8'), IPHASX J190700.7+043041(18'), IPHASX J192543.2+143546 (3') and IPHASX J194645.3+262211 (5'), have low observed surface brightnesses between 10^{-16} and 10^{-18} erg cm^{-2} s^{-1} arcsec^{-2} (see Table 8.2), which

would explain why they had not been detected before. Smaller nebulae (with a size lower than 60 arcsec) are also detected in the same area. If we compare the size of the candidate PNe and their stage (Figure 8.30 bottom), we can see that the later stages (from WZO3 to WZO4) can be mainly linked to some of the largest objects. Those are therefore more affected by the ISM. But this only concerns 3 large PNe/ISM out of 12, two of them also being located at low latitude: IPHASX J190227.3+020815(WZO4) and IPHASX J190700.7+043041 (WZO3).

In two hours in RA, we detected, thanks to the IPHAS's sensitivity, 21 candidate PNe that can be associated with PNe/ISM interaction. A source of error in the identification of these objects lies in the confusion which can be made with other type of nebulae (e.g SNR) which can also be affected by the ISM (Fig. 8.32) and by the geometry of the candidate PNe which does not allow us to identify an interaction process (Fig. 8.33). Also, the angle from which the interaction is seen will affect our interpretation of the whole interaction process: the comparison with hydrodynamical simulations and proper motion measurements may be biased. We may not see it if the PN moves in the line-of-sight.

Large PNe seem to survive at relatively low latitudes but there they will undergo strong alteration by the ISM and will display more advanced stages of interaction. Those disruptions tend to affect them more than smaller size nebulae in the same latitude range. But in the area of maximum extinction (E(B-V) up to ~13 mag), i.e. where the contribution of the interstellar medium is higher (b=±0.5 deg and 30 deg <l < 50 deg), there is a total lack of PNe/ISM. It could be a detection problem , or more likely, if there were PNe/ISM at this location, they have been totally destroyed by the effect of the ISM. In the longitudinal plane, the more advanced stages are mainly located near the zone of higher ISM density (35 deg <l < 52 deg) while the more recent stages (WZO2) are located far from this region, where the ISM density is lower. The Warm Neutral Medium (WNM) (derived from HI 21 cm emission) and the Warm Ionised Medium (WIM) (derived from Hα emission) have densities between n_0=0.2 and n_0=0.5 cm^{-3} (Ferrière 2001). Wareing et al. (2007) used a density of n_0=2 cm^{-3} as a typical value

in the plane. Borkowski et al. (1990) state that the first distortions in the nebulae occur when $n_{PN} \sim 10n_0$. We cannot define a clear boundary for the lowest ISM density required to suppress any sign of interaction, but we can assume that it will be around 100 cm^{-3} which is the lowest density for the molecular clouds and the star forming regions which populate the part of the sky we are investigating. A deeper analysis of the candidate PNe will help to constrain the ISM density but we can still make two remarks: first, a PN is more likely to be found in the warm ISM than in the denser cold ISM and secondly, a PN located at a high Galactic latitude is more likely to be exposed to the hot Galactic halo. Both phenomena may affect the PN particularly for the development of RT instabilities requiring an ISM hotter than the nebula. The other effects are not fully known.

The turbulences, vortexes and filaments observed are not necessarily due to the action of interstellar magnetic fields; and most of the hydrodynamical models are "magnetic-free" (Villaver et al. (2003), Wareing et al. (2007)). But Dgani and Soker (1998) and more recently Ransom et al. (2008) showed that interstellar magnetic fields would reinforce Rayleigh-Taylor instabilities and therefore the fragmentation in the PNe, generating the shapes observed during the ISM-interaction. In addition, Ferrière (2001) state that the ISM magnetic field would increase with an increase of the interstellar density from a few μG to a tens of μG. The action of magnetic fields is discussed in Part III.

Although we did not find any typical WZO1 candidate PNe (i.e. showing a distant bow shock) in our area of study, a good example can be found in a new large PN (6 arcmin long) discovered within the survey in the 20h region. The "Ear nebula" or IPHASX J205013.7+465518, has been spectroscopically classified as a PN and is composed of two shells (Fig. 8.31). The outer shell is thick and shows signs of motion in the North-West direction (indicative of an interaction with the ISM). Some sharp structures are also seen in the same direction. The inner shell is a filamentary bipolar structure heading in the same direction as the outer shell. We believe that the
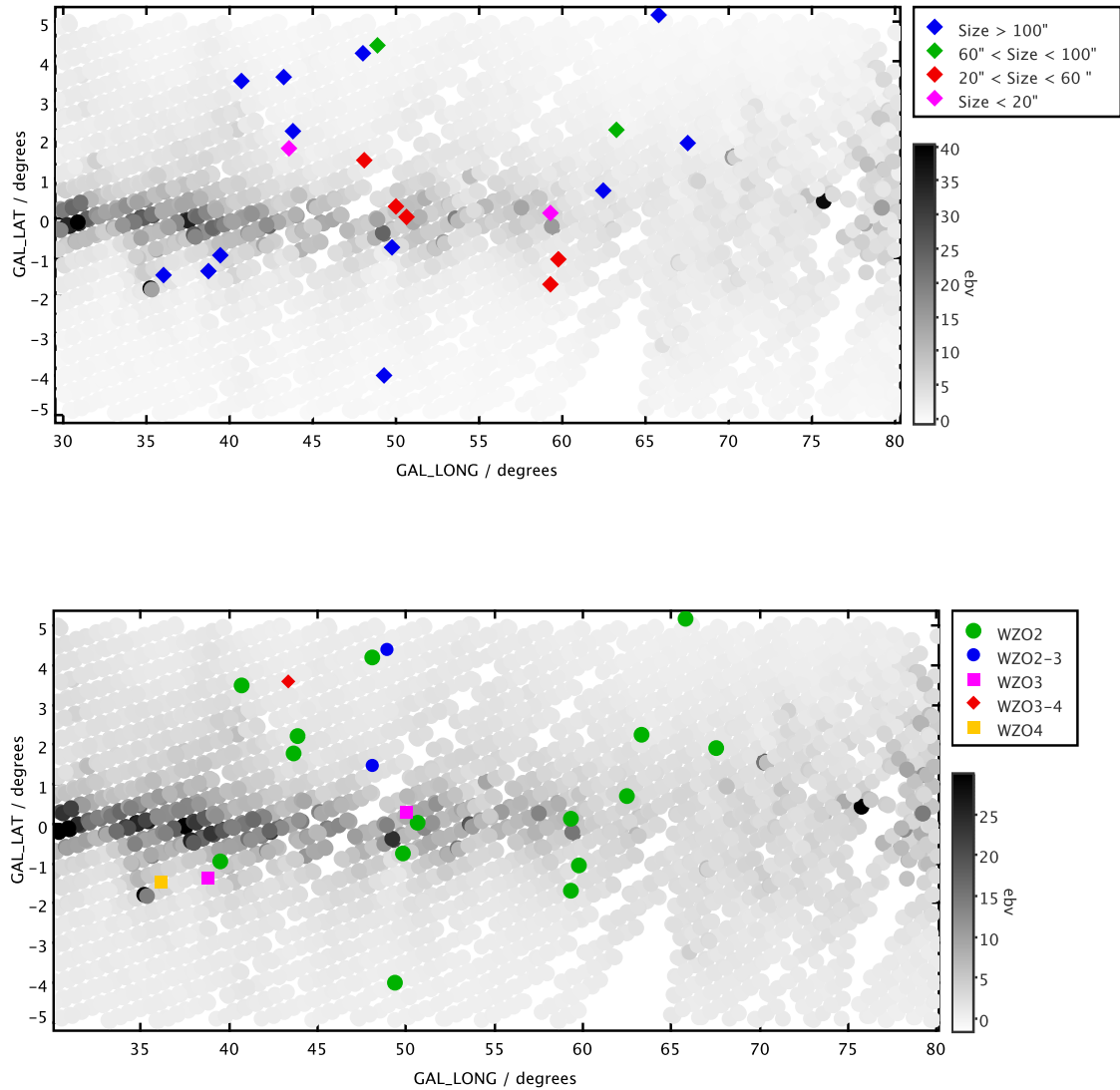
Figure 8.30: Distribution of the candidate PNe/ISM in the plane according their size and stage of interaction.

planetary nebula is only the interior part while the exterior structure is the remainder of the AGB shell. This is similar to stage 1 of interstellar interaction, but at first the inner structure is bipolar and not spherical, then the sharp structures on the sides and at the rear show the depletion of nebular material from the front interacting rim which

is more compatible to a stage 2 transition to stage 3.
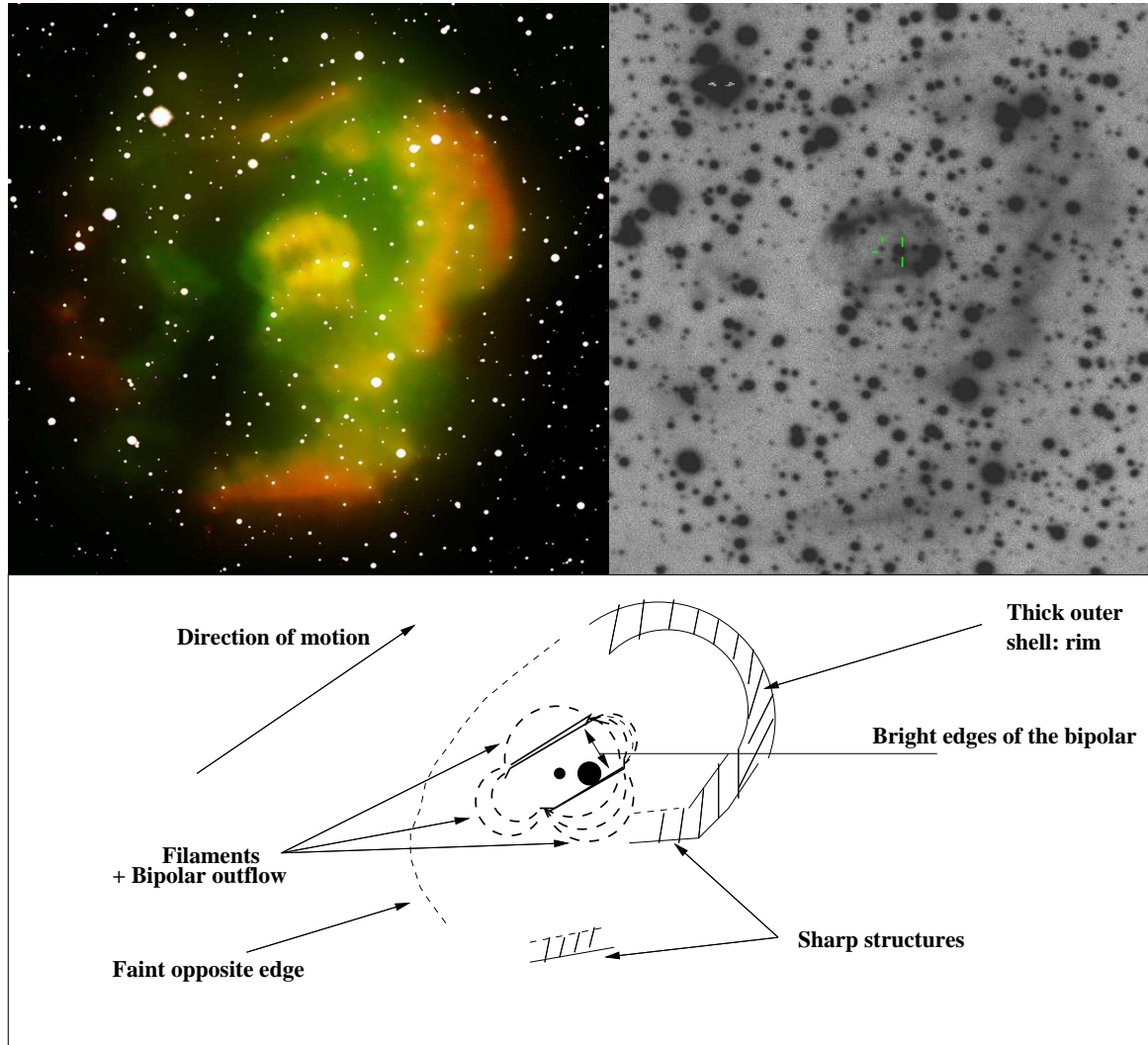
Figure 8.31: IPHASX J205013.7+465518. North on the Top and East on the left. The CS candidates are indicated by the two green dashes. On the colour image (issued from the INT/WFC), the green corresponds to the [OIII] emission and the red to the Hα+[NII] emission.
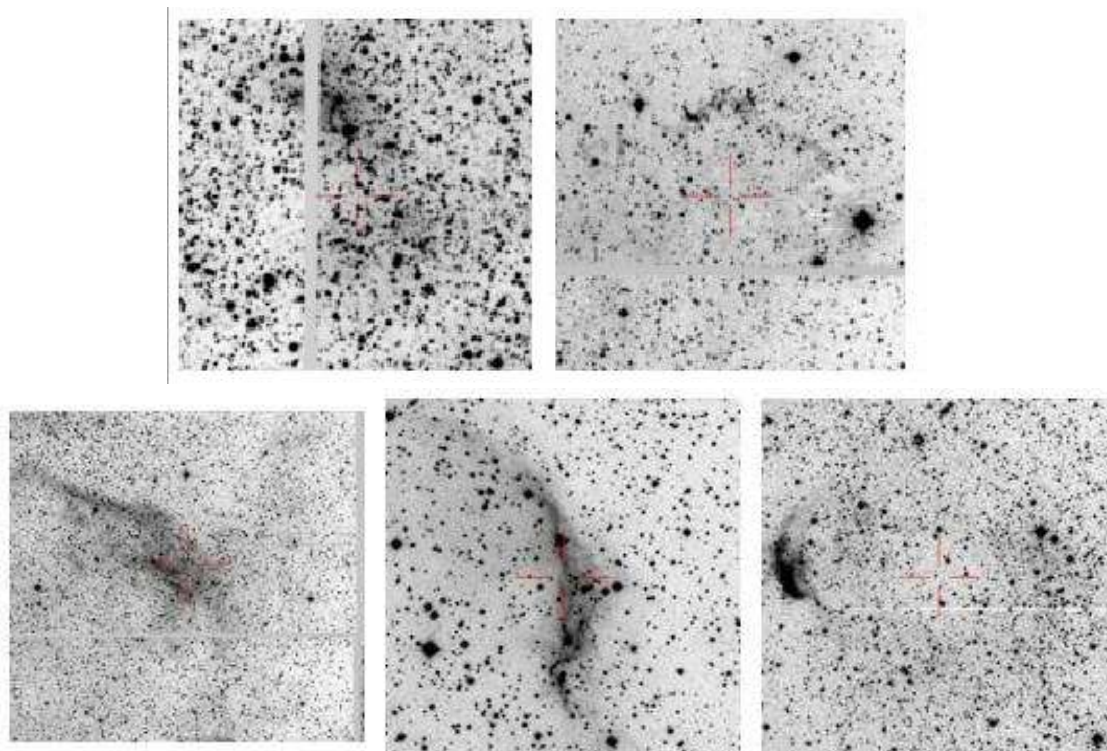
Figure 8.32: Supernovae or large PN with ISM interaction (mostly stage 2)? From the Top to Bottom, from Left to Right: IPHASX J184253.2-022642, IPHASX J185223.1+005322, IPHASX J192410.6+133443, IPHASX J195015.9+272859, IPHASX J195919.6+283827.
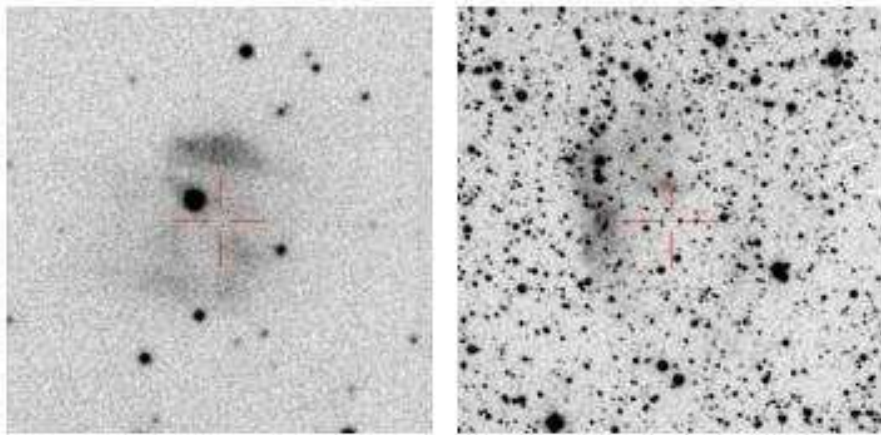
Figure 8.33: From Left to Right: IPHASX J190346.8+050935: Bipolar PN viewed face-on or stage 4 of ISM interaction in the North-South direction?, IPHASX J190614.9-013318: Bipolar with bright waist or stage 2 of interaction, direction East ?